放射対流平衡下における湿潤対流の自己集合化に関する数値的研究

柳瀬 友朗
京都大学大学院理学研究科 / 理化学研究所計算科学研究センター

- 気象衛星からみた熱帯の雲

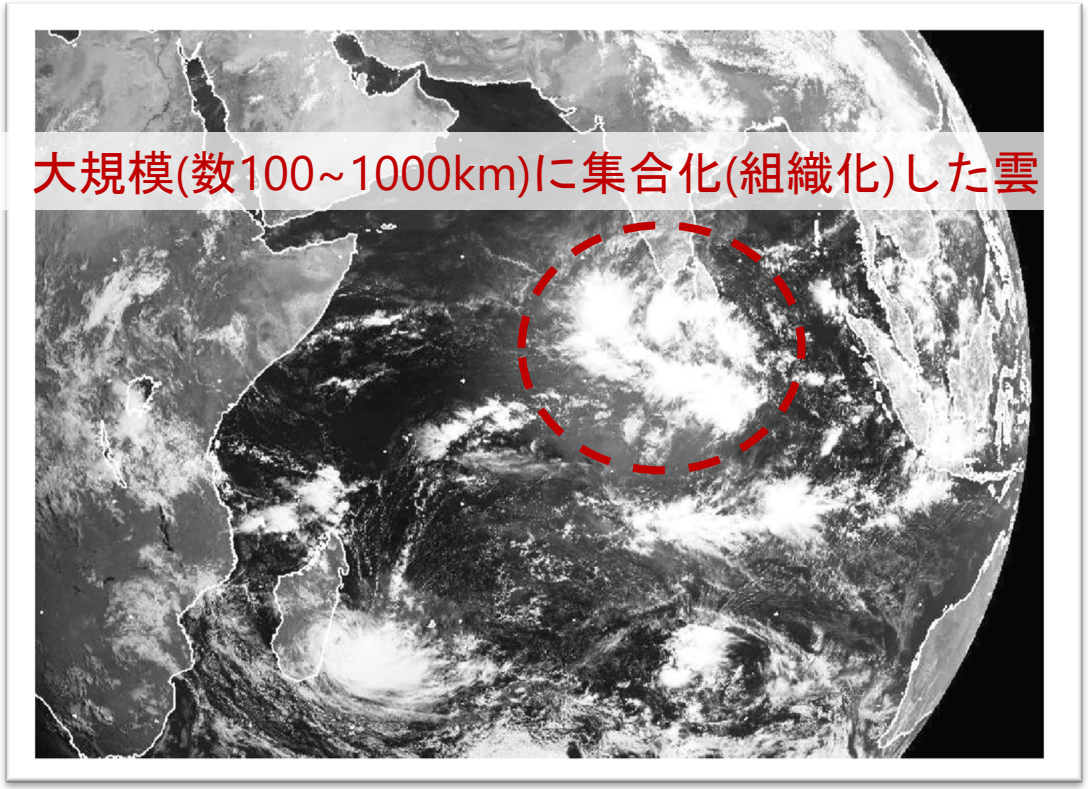

Holloway et al. (2017, *Surv Geophys*) Fig.1に加筆

- "水平一様な境界条件"の理想化大気数値実験における雲

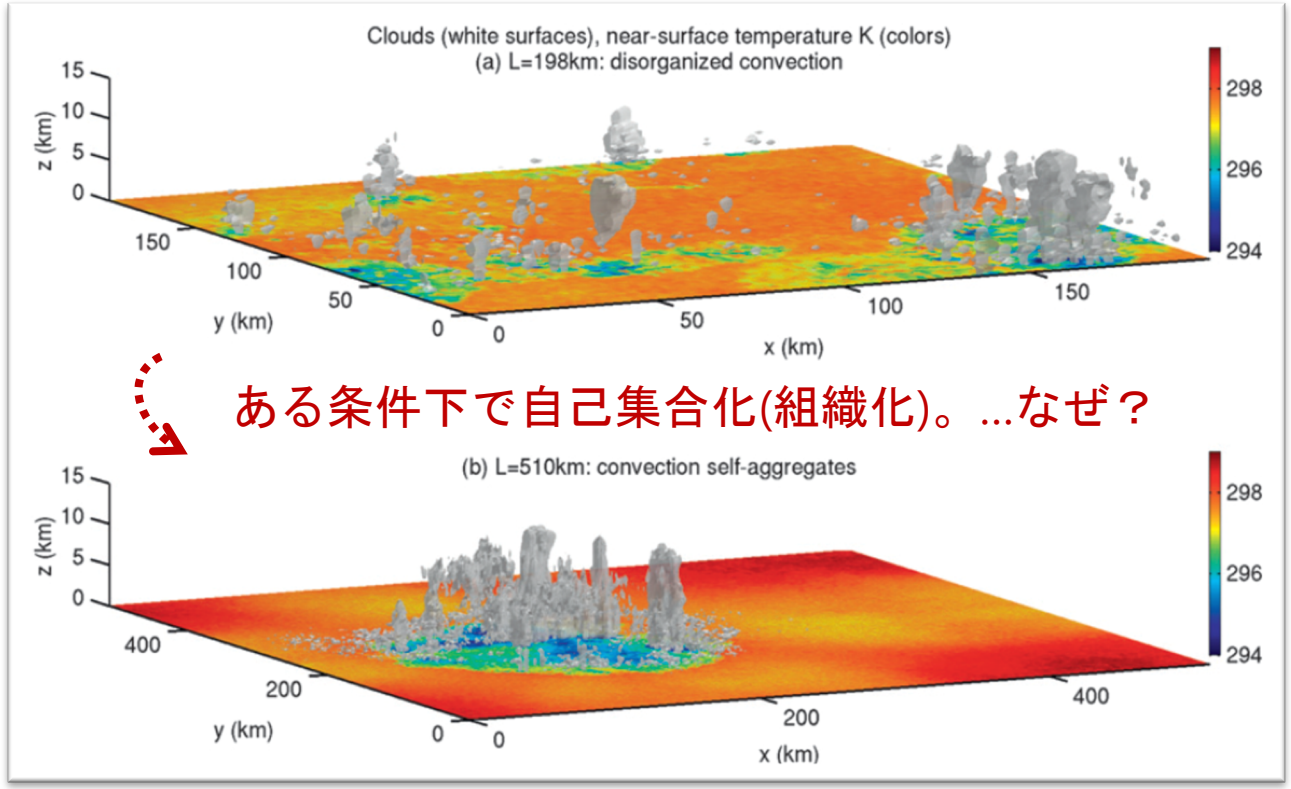

Muller and Held (2012, *J. Atmos. Sci.*) Fig.1に加筆

自己紹介

Time

[2019/04 – present]

所属：京都大学 大学院理学研究科 地球惑星科学専攻 地球物理学分野 博士後期課程 (D3)
/ 理化学研究所 計算科学研究センター 複合系気候科学研究チーム (大学院生リサーチ・アソシエイト)

博論：放射対流平衡下における湿潤対流の自己集合化に関する数値的研究

指導：竹見哲也 教授 / 富田浩文 チームリーダー

[2017/04 – 2019/03]

所属：京都大学 大学院理学研究科 地球惑星科学専攻 地球物理学分野 修士課程

修論：高解像度放射対流平衡実験における積雲アンサンブルの統計的性質

指導：竹見哲也 准教授 (当時)

[2013/04 – 2017/03]

所属：京都大学 総合人間学部

卒論：地表付近の大気乱流における浮力効果の考察 ~熱対流乱流の室内実験研究~

指導：酒井敏 教授

[1994/10]

出身：つくば

目次

① **Yanase, T.**, Nishizawa, S., Miura, H., Takemi, T., & Tomita, H. (2020).
New critical length for the onset of self-aggregation of moist convection. *Geophys. Res. Lett*. **[published; 主に3章の内容]**

② **Yanase, T.**, Nishizawa, S., Miura, H., Takemi, T., & Tomita, H. (2021).
Low-level circulation and its coupling with free-tropospheric variability as a mechanism of spontaneous aggregation of moist convection. *J. Atmos. Sci.* **[under review; 主に4章の内容]**

目次

① **Yanase, T.**, Nishizawa, S., Miura, H., Takemi, T., & Tomita, H. (2020).
New critical length for the onset of self-aggregation of moist convection. *Geophys. Res. Lett.* **[published; 主に3章の内容]**

② **Yanase, T.**, Nishizawa, S., Miura, H., Takemi, T., & Tomita, H. (2021).
Low-level circulation and its coupling with free-tropospheric variability as a mechanism of spontaneous aggregation of moist convection. *J. Atmos. Sci.* **[under review; 主に4章の内容]**

序論：雲と気候

- 気候システムにおける雲の重要性
  - 光学特性を通した放射収支への作用
  - 降水過程を通した水収支への作用
  - 潜熱解放を通した大気循環への作用
- 気候モデルにおける雲表現の不確実性
  - 気候感度に関わる雲フィードバックのモデル間不一致
  - 雲の組織化に伴うフィードバックの欠如・理解不足

Mauritsen and Stevens (2015, *Nat. Geosci.*)

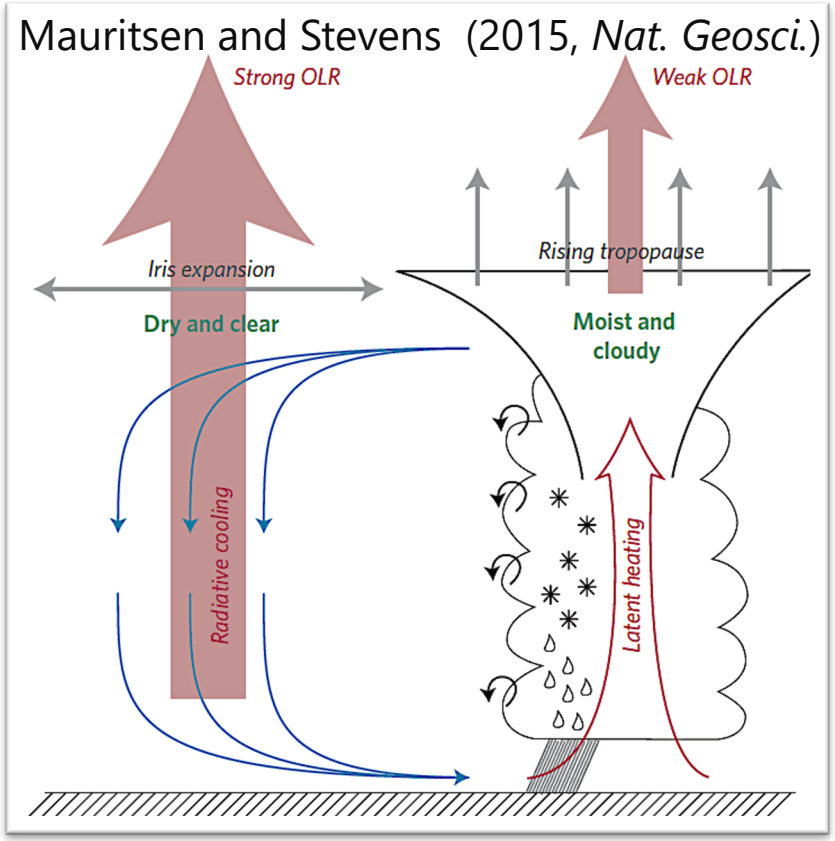

Bony et al. (2015, *Nat. Geosci.*)

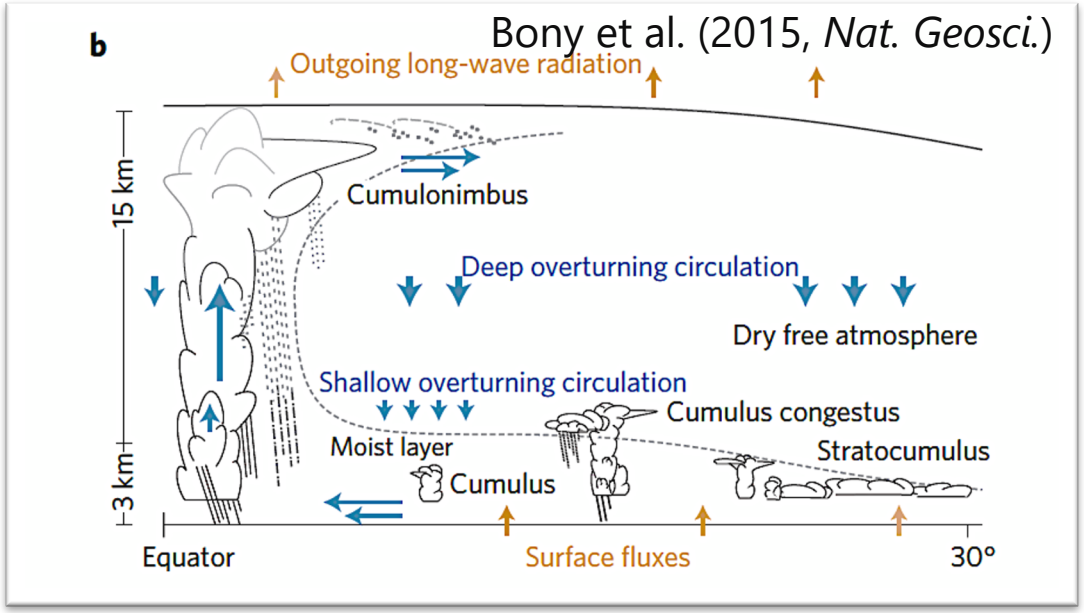

Stevens and Bony (2013, *Science*)

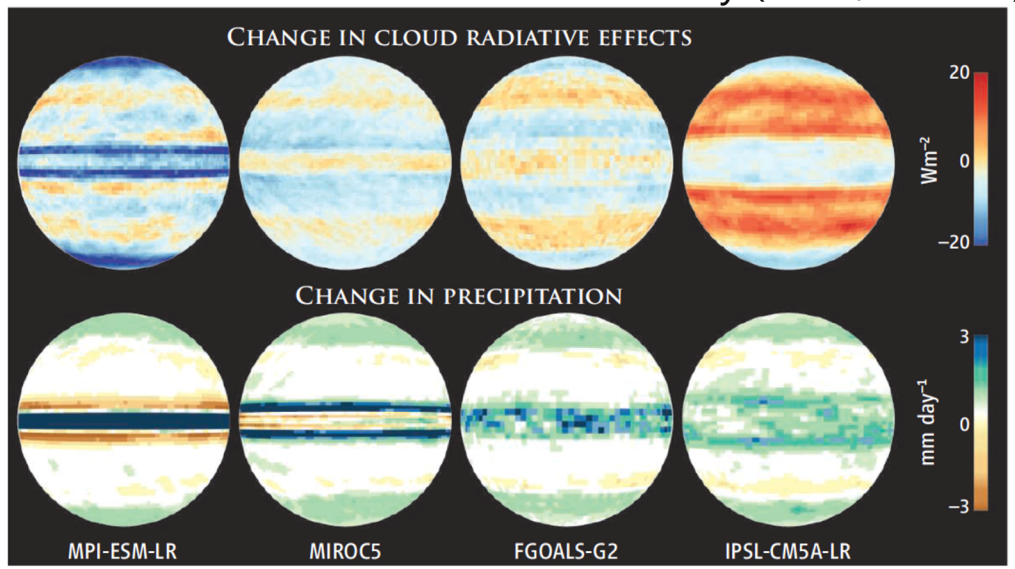

序論：対流の組織化と放射対流平衡

■ 対流の自己集合化 (Convective Self-Aggregation, CSA; e.g., Wing et al. 2017; Muller et al. 2022)
- 水平一様な境界条件の放射対流平衡(RCE)実験で発現する自発的な組織化過程

Muller and Held (2012, MH12)

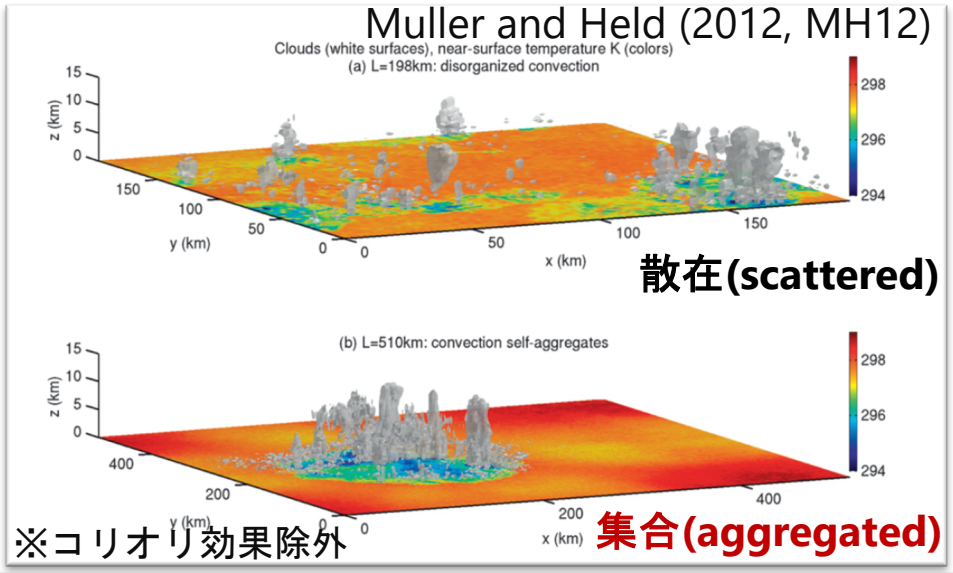

□特徴
- 湿潤-雲域と乾燥-晴域に分離
- (領域平均的な)上層雲減・湿度減・外向長波放射(OLR)増

□現実大気との関係
- 熱帯の組織化した雲擾乱の理想化形態
  - ➢ f面RCE ⇒ 熱帯低気圧的構造発現
  - ➢ β面(or球面)RCE ⇒ 熱帯季節内振動的構造発現
- 湿度・OLRと集合化度合の関係の類似性
  - ➢ 温暖化時の上層雲フィードバックへの寄与?
  - ※ 最新気候感度評価(Sherwood et al. 2020)で言及

□未解明なこと
- どのように温暖化応答し気候に作用?
- 海面温度の時間発展を許容するとどうなる?
- どのような条件で発生?
- どのようなメカニズムで発生?

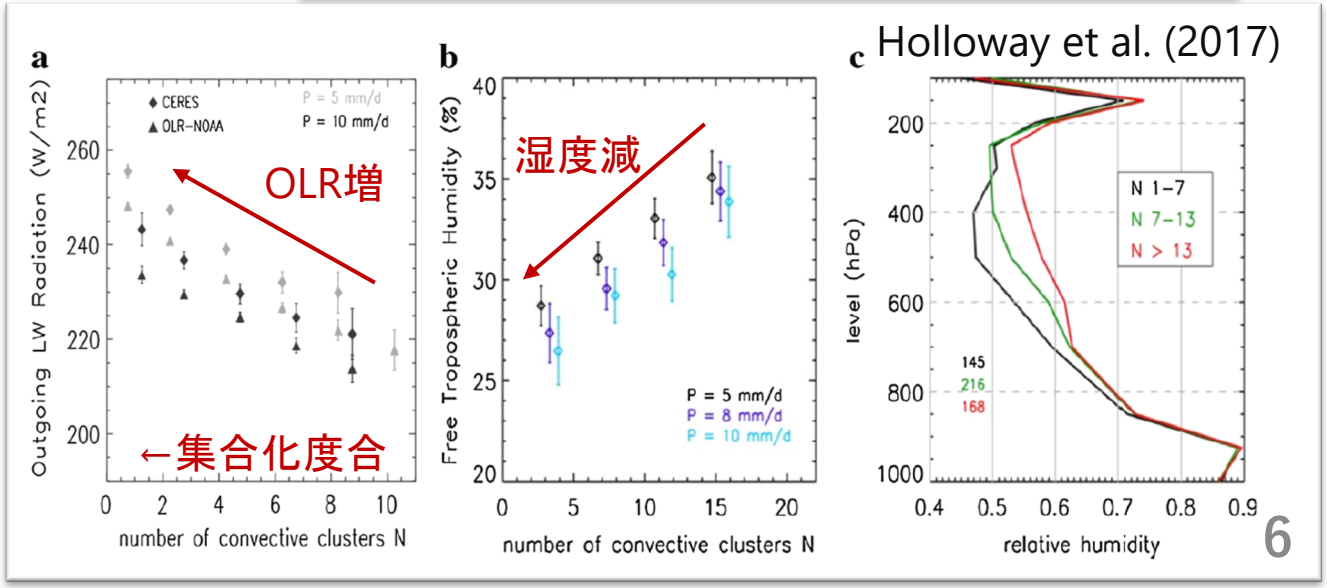

序論：研究目的

■ 現状の理解と課題

□CSA発生条件

- 領域RCE実験に用いる 水平領域幅 **L**・水平格子幅 **H** に対する依存性
  - ➢ 広領域　でのみ発生 (L ≧ 200–300 km)
  - ➢ 低解像度でのみ発生 (H ≧ 2000 m)

□CSA発生メカニズム

- 水蒸気の水平不均一性を増幅・抑制する要因
  - ➢ 対流圏全層にわたる放射冷却
  - ➢ 境界層内の循環や冷気プール

■ **本研究の問い**

□高解像度(H < 2000 m)でも領域幅十分大きければ, CSA発生?
(if yes,)

- 臨界長さ(領域幅)はどのくらいの大きさ?
- なぜCSA発生は領域幅に依存?
- なぜ格子幅2000 mで臨界長さが大きく変化?

} 第3章

- どのようなメカニズムで散在から集合に遷移?
- 境界層過程と自由対流圏過程の関係は?

} 第4章

レジーム境界が
どこに存在するかは未知

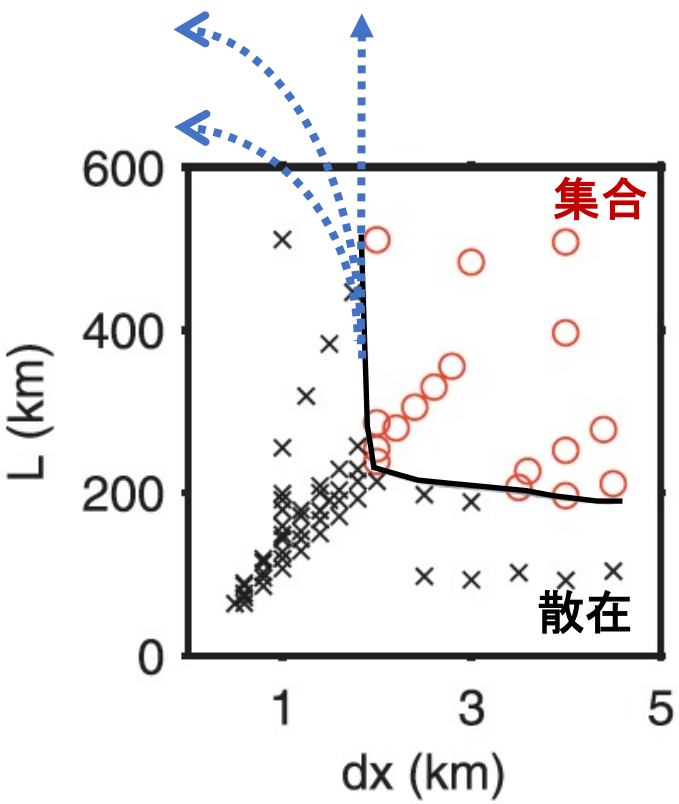

RCEレジーム図 (MH12)
縦軸: 水平領域幅
横軸: 水平格子幅

目次

① **Yanase, T.**, Nishizawa, S., Miura, H., Takemi, T., & Tomita, H. (2020).
New critical length for the onset of self-aggregation of moist convection. *Geophys. Res. Lett.* **[published; 主に3章の内容]**

② **Yanase, T.**, Nishizawa, S., Miura, H., Takemi, T., & Tomita, H. (2021).
Low-level circulation and its coupling with free-tropospheric variability as a mechanism of spontaneous aggregation of moist convection. *J. Atmos. Sci.* **[under review; 主に4章の内容]**

数値モデル及び実験設定

■ SCALE-RM version 5.3.3 (Nishizawa et al. 2015; Sato et al. 2015) ※LESとして発展. 大規模計算に強み.
3次元完全圧縮非静力学方程式系 領域大気モデル (コリオリ力は除く.)

□ 共通設定 (基本的にMH12とTompkins & Craig 1998を模擬)

- 物理過程
  - ➢ 雲物: 6クラス・1モーメントバルク型 (Tomita 2008)
  - ➢ 乱流: Smagorinsky-Lilly型 (Brown et al. 1994; Scotti et al. 1993)
  - ➢ 地表: 普遍関数を用いたバルク型 (Beljaars & Holtslag 1991; Wilson 2001). 海面温度300 K 固定.
  - ➢ 放射: 2流近似・広帯域型 (Sekiguchi & Nakajima 2008). 大気上端下向短波固定.
- 領域設定
  - ➢ 水平: 正方形型. 二重周期境界.
  - ➢ 鉛直: 上端高度24 km, 上部6 kmにスポンジ層, 下層ほど密に64層.
- 初期化手続
  - ➢ GCSS tropical squall line case (Redelsperger et al. 2000) の熱力学プロファイルから, H2000L96で100日積分.

□ 制御パラメータ
- 水平格子幅 **H**: 4000–500 m
- 水平領域幅 **L**: 96–960 km

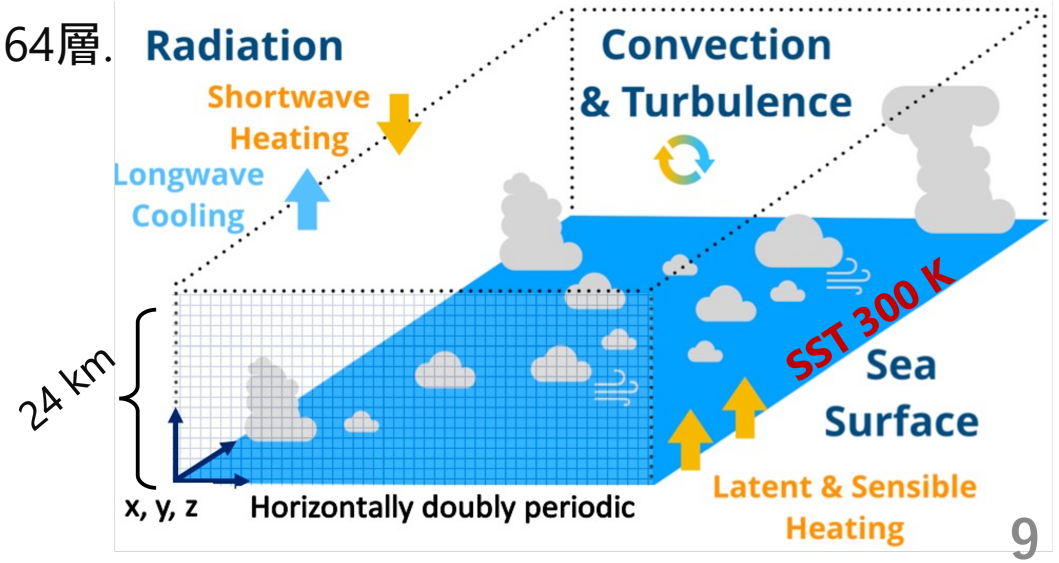

目次

① **Yanase, T.**, Nishizawa, S., Miura, H., Takemi, T., & Tomita, H. (2020).
New critical length for the onset of self-aggregation of moist convection. *Geophys. Res. Lett.* **[published; 主に3章の内容]**

② **Yanase, T.**, Nishizawa, S., Miura, H., Takemi, T., & Tomita, H. (2021).
Low-level circulation and its coupling with free-tropospheric variability as a mechanism of spontaneous aggregation of moist convection. *J. Atmos. Sci.* **[under review; 主に4章の内容]**

CSA発生条件：高解像度・広領域実験でのCSA

■ 水平領域幅Lが異なる2つの実験における雲(アニメーション).

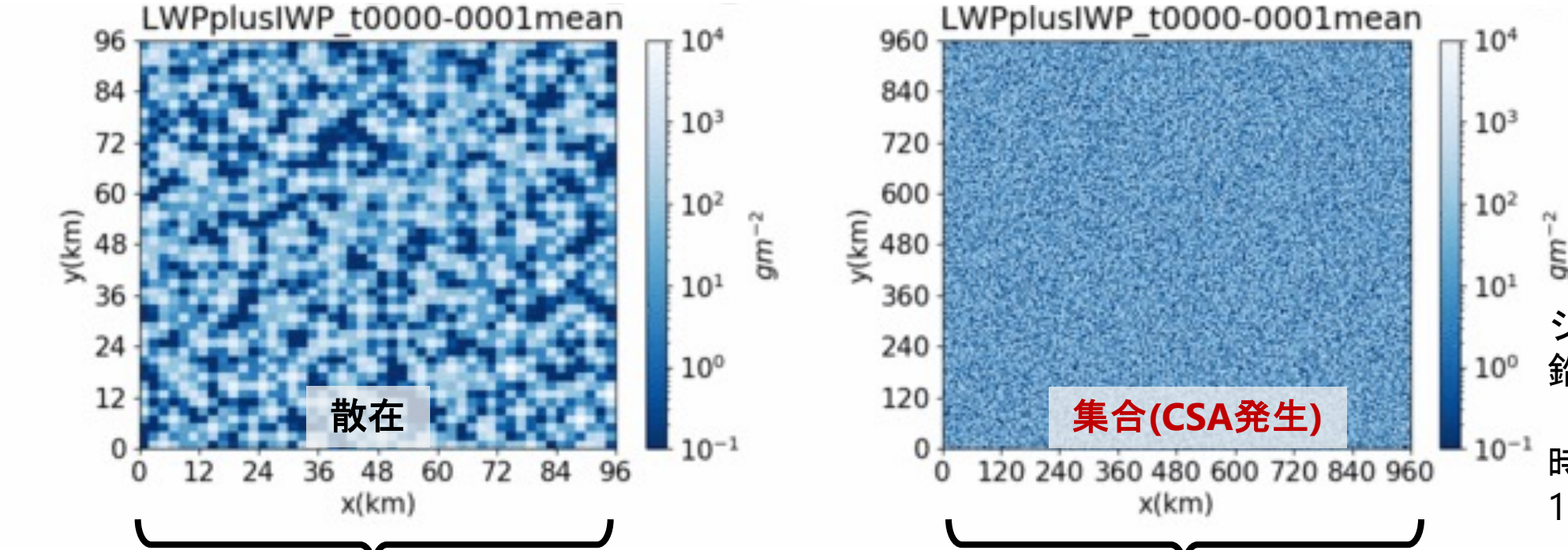

シェード:
鉛直積算凝結物量(g m^{-2})

時間:
1時間/フレーム

L ~ 100 km
H=2 km
積分時間50日

領域幅10倍

L ~ 1,000 km
H=2 km
積分時間40日

□ 領域幅が大きいとCSA発生(雲が自発的にクラスター化)

CSA発生条件：高解像度・広領域実験でのCSA

■ 水平格子幅H・水平領域幅Lが異なる6つの実験における水蒸気場.

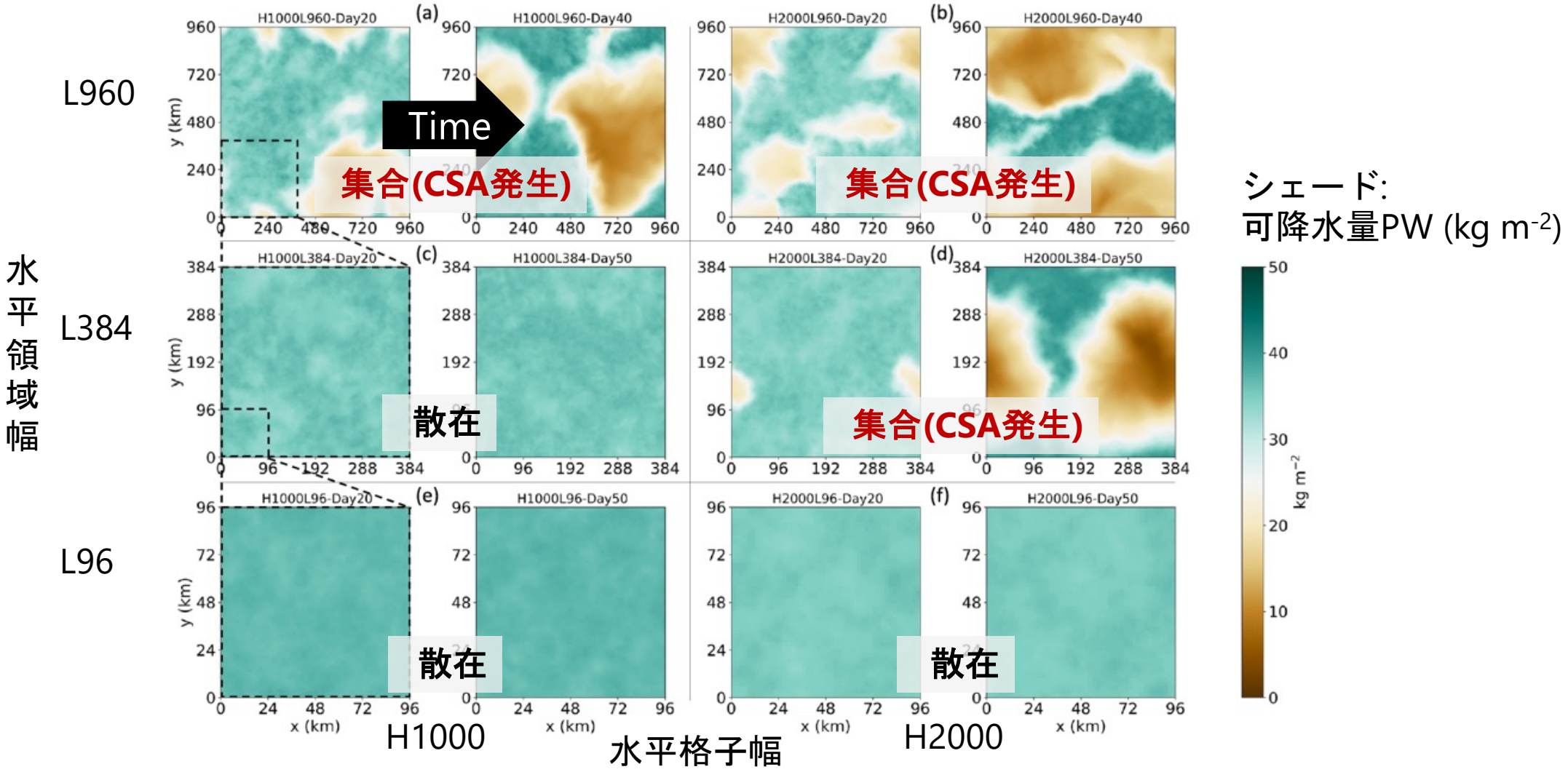

□ 高解像度(H < 2000 m)でも領域幅十分大きければ, CSA発生.

Yanase et al. (2020) Fig. 1に基づく

CSA発生条件：RCEレジームダイアグラム

■ 様々なH・Lに対するRCEレジーム.

(a) 乾燥パッチ面積率の時間発展
- 増加するものを集合と判定.

(b) RCEレジーム図. (a)に基づく判定.
- 線II, IIIはMH12とよく対応.
  線IIIの臨界長さは約200 km.

- 線Iは新発見のレジーム境界.
  臨界領域幅約**500 km**.

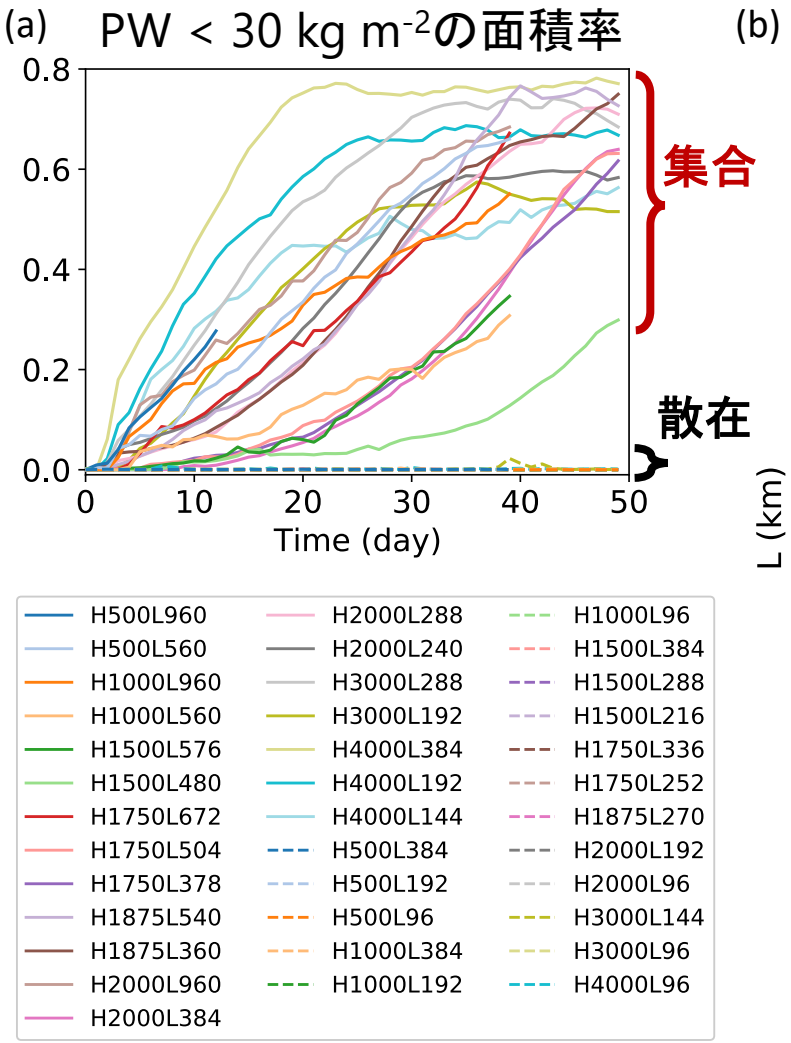

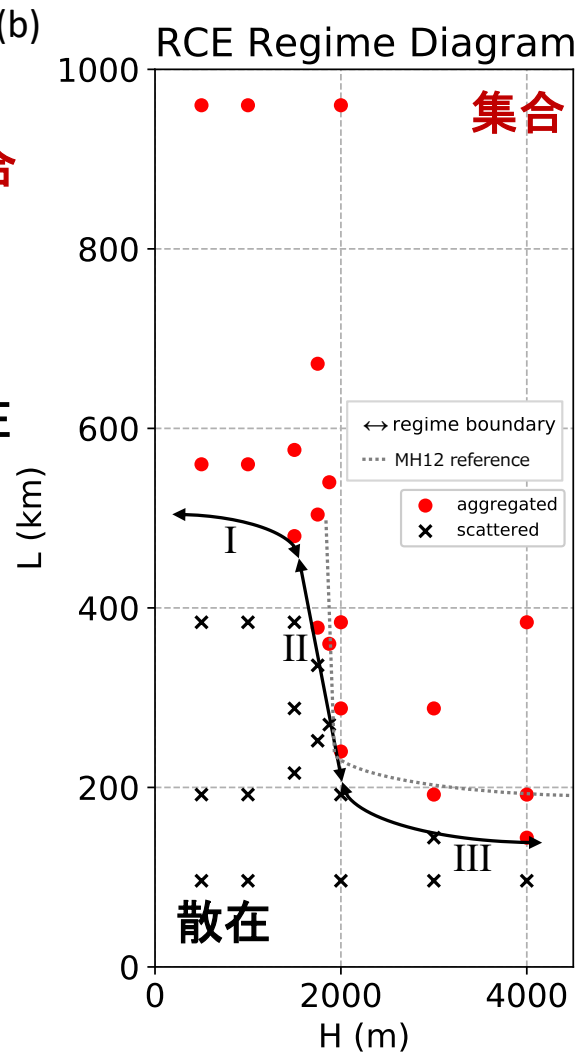

□ CSAに約500 kmの特徴的な長さが存在することを示唆.

Yanase et al. (2020) Fig. 2に基づく

◘ なぜCSA発生は領域幅に依存? 既往研究が提示したメカニズムは?

- 湿潤域における降水蒸発に伴う冷気プールがもつ抑制効果
  - ➢ 通常実験(左)と降水蒸発抑制実験(右)の地表付近水蒸気量
    Jeevanjee & Romps (2013) Figs.1&2

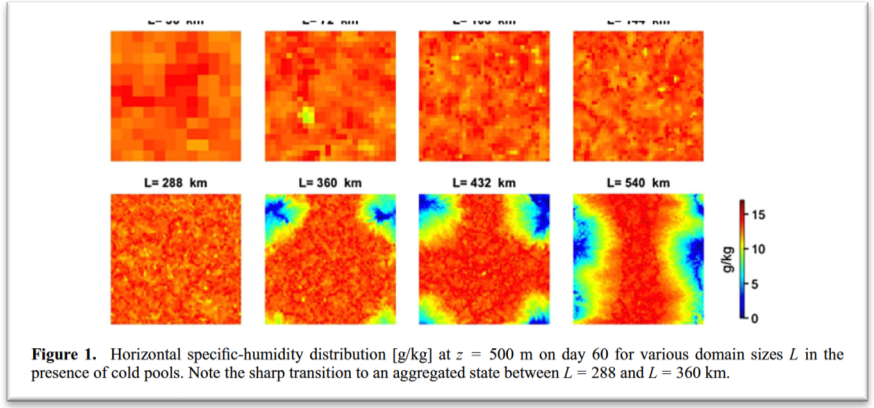

Figure 1. Horizontal specific-humidity distribution [g/kg] at z = 500 m on day 60 for various domain sizes L in the presence of cold pools. Note the sharp transition to an aggregated state between L = 288 and L = 360 km.

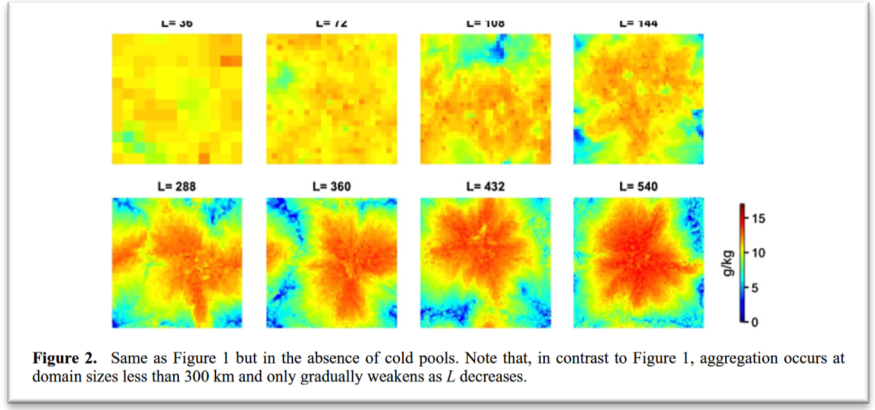

Figure 2. Same as Figure 1 but in the absence of cold pools. Note that, in contrast to Figure 1, aggregation occurs at domain sizes less than 300 km and only gradually weakens as L decreases.

  - ➢ 蒸発駆動冷気プールに伴う地表付近の循環
    Tompkins (2001) Fig. 14 に基づく

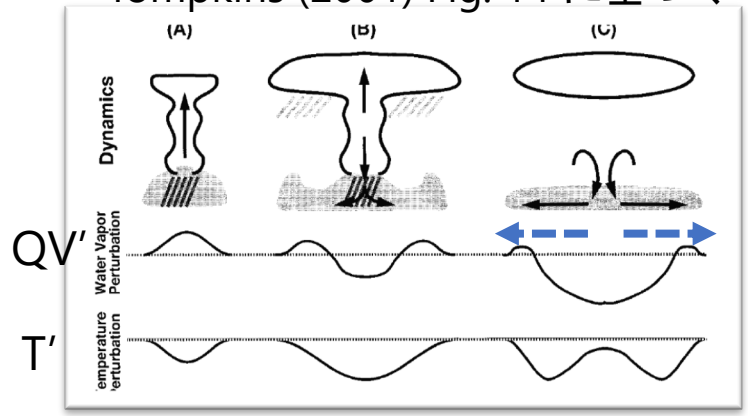

- 乾燥域における放射冷却に伴う冷気プールがもつ促進効果
  - ➢ 乾燥域下層に人為的に強い冷却を与えた実験のPW
    Muller & Bony (2015) Fig.1

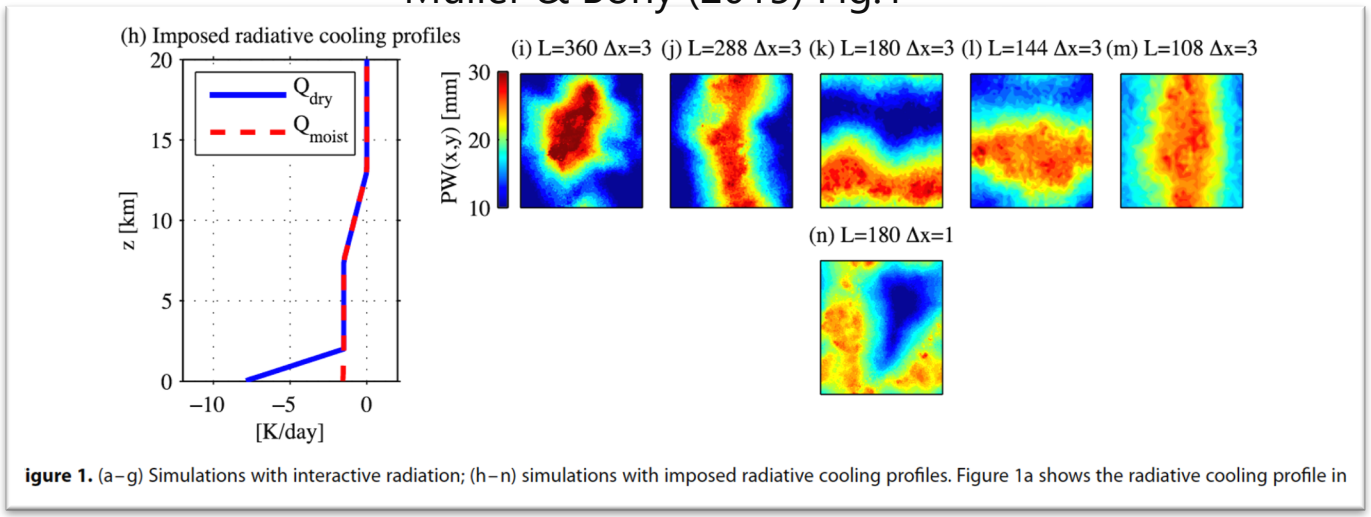

igure 1. (a–g) Simulations with interactive radiation; (h–n) simulations with imposed radiative cooling profiles. Figure 1a shows the radiative cooling profile in

  - ➢ 放射駆動冷気プールに伴う循環
    Coppin & Bony (2015) Fig. 13a

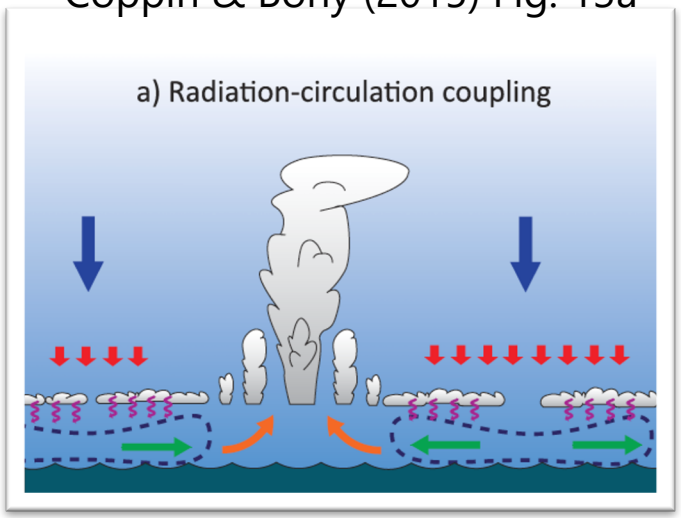

CSA発生条件：下層水蒸気輸送

■ CSA発生(≒水蒸気水平不均一性の増幅)を抑制・促進させる地表付近の水蒸気水平輸送.

- 湿潤域の蒸発駆動冷気プールによる抑制効果 vs. 乾燥域の放射駆動冷気プールによる促進効果

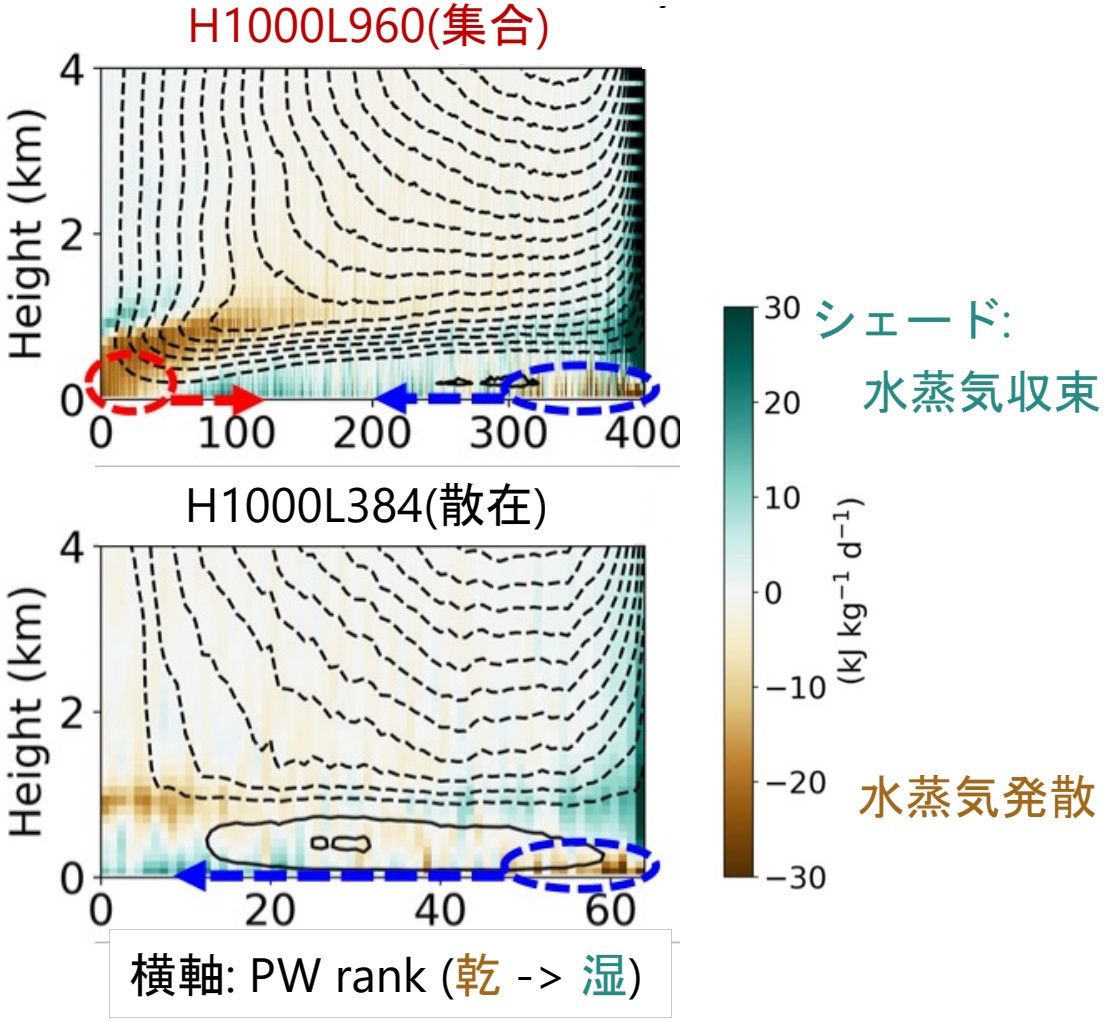

コンター:
Bretherton et al. (2005)の有効流線関数$\Psi^{BBK05}{}_{i,z}$

$$\Psi_{i,z}^{\mathrm{BBK05}} \equiv \sum_{j=1}^{i} (\rho w)_{j-1/2,z}$$

iはPW rank
破線:反時計回り; 実線:時計回り循環
PW rankは$(48\mathrm{km})^2$ブロック平均PWの昇順

Yanase et al. (2020) Fig. 3に基づく

□ 領域幅大の時に促進効果が抑制効果を上回りCSA発生

CSA発生条件：下層流れ場と水平スケール

□ では, なぜ臨界長さ(~数100km)より領域幅大(領域幅小)の時に促進効果(抑制効果)が支配的になる?

- 相反する効果の速度スケール比較:
  1. RCE下における冷気プール速度u_cは 2–5 m/s (Tompkins, 2001)
  2. 放射冷却に駆動される境界層内の風速は下降流域の空間規模に依存 (Wing & Cronin, 2016)
     - 典型的な下降流速度w_{sub} , 境界層厚みz_{pbl}(Tompkins & Craig, 1998b)を連続式(円筒)に代入: $u_s(r) = \frac{w_{sub}}{2z_{pbl}} r$
       → 数100kmの空間規模rにおいて数m/sの速度

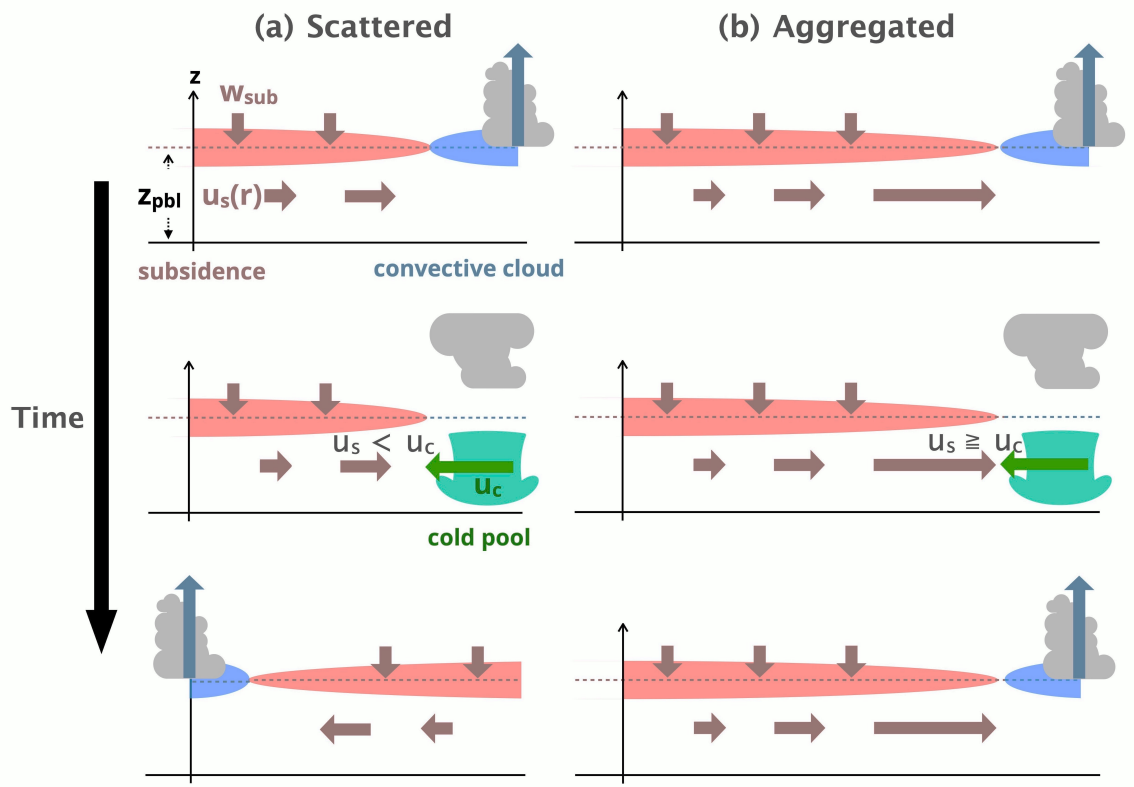

□ 相反する効果をもつ下層の流れの拮抗によりCSA発生有無決定

Yanase et al. (2020) Fig. 4

CSA発生条件：解像度依存性

■ なぜ格子幅2000 mで臨界長さが大きく変化?

- 低解像度RCE実験: 下層雲が多く, 放射冷却が強い (Yanase & Takemi, 2018; Muller & Bony, 2015)
  - 低解像度実験は高解像度実験と比べて, 「下層雲多 -> 放射冷却強 -> 促進効果強 -> 臨界長さ短」.
  - よって, 同じ領域幅でも低解像度の方がCSA発生しやすい.

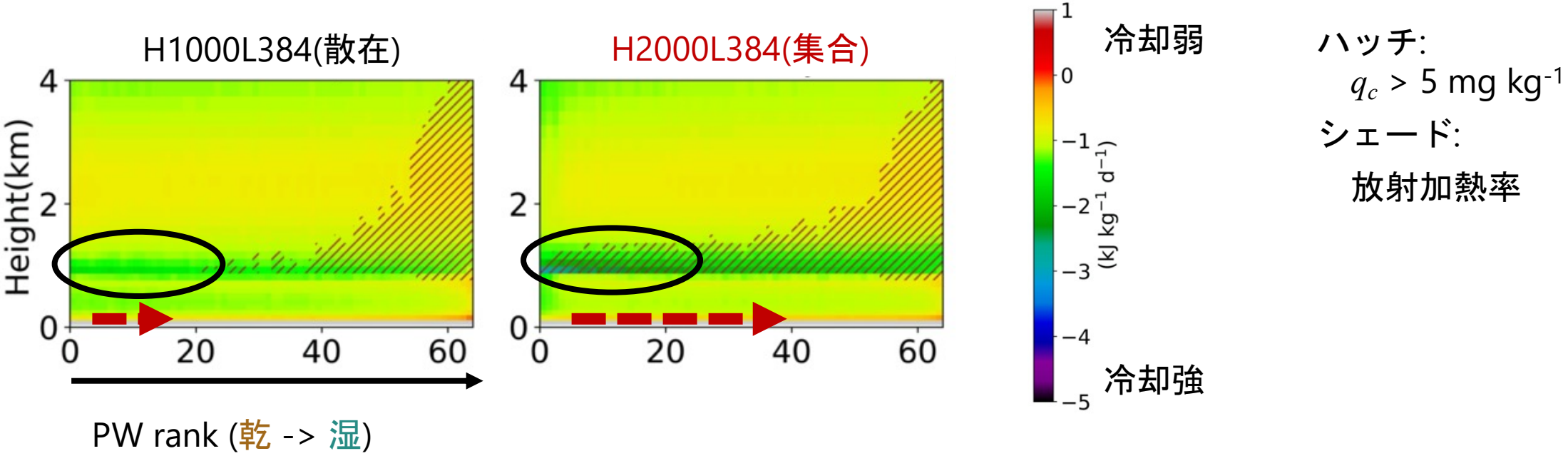

■ CSA発生の解像度依存性には, 下層雲及び放射冷却が役割を担う.

第3章のまとめ

- 湿潤対流の自己集合化の発生条件を調査するために,
  SCALE-RMを用いたRCE実験を, 様々な水平格子幅H・水平領域幅Lで系統的に実行.

- 高解像度[H≦1 km]・広領域[L≧500 km]において, 自己集合化が発生することを初めて発見し,
  H-L空間におけるレジーム図を定性的に更新.

- 集合化発生有無は, 地表付近の水平水蒸気輸送に関する相反する効果の拮抗により決定.
  (1)湿潤域の降水蒸発で駆動される冷気プール → 水蒸気水平不均一性を減衰させ, CSA発生を抑制
  (2)乾燥域の放射冷却で駆動される冷気プール → 水蒸気水平不均一性を増幅させ, CSA発生を促進

- (2)は水平規模に依存するため, 領域幅が臨界長さを超えると(2)が(1)を上回り, 集合化発生に至る.

- 臨界長さの解像度依存性は, 下層雲量および放射冷却量の増減が鍵.

目次

① **Yanase, T.**, Nishizawa, S., Miura, H., Takemi, T., & Tomita, H. (2020).
New critical length for the onset of self-aggregation of moist convection. *Geophys. Res. Lett.* **[published; 主に3章の内容]**

② **Yanase, T.**, Nishizawa, S., Miura, H., Takemi, T., & Tomita, H. (2021).
Low-level circulation and its coupling with free-tropospheric variability as a mechanism of spontaneous aggregation of moist convection. *J. Atmos. Sci.* **[under review; 主に4章の内容]**

CSA発生メカニズム：はじめに

■ 本章の目的：領域幅増加に伴うCSA発生メカニズムを，下層循環の発達とその自由対流圏との結合の観点から解明

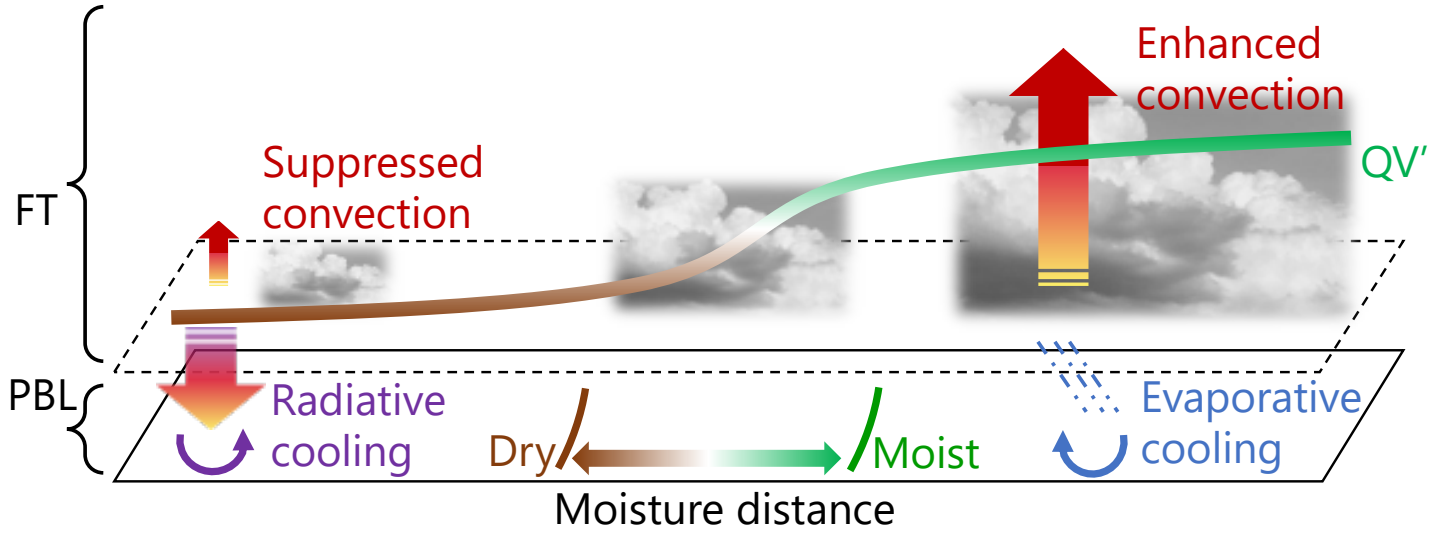

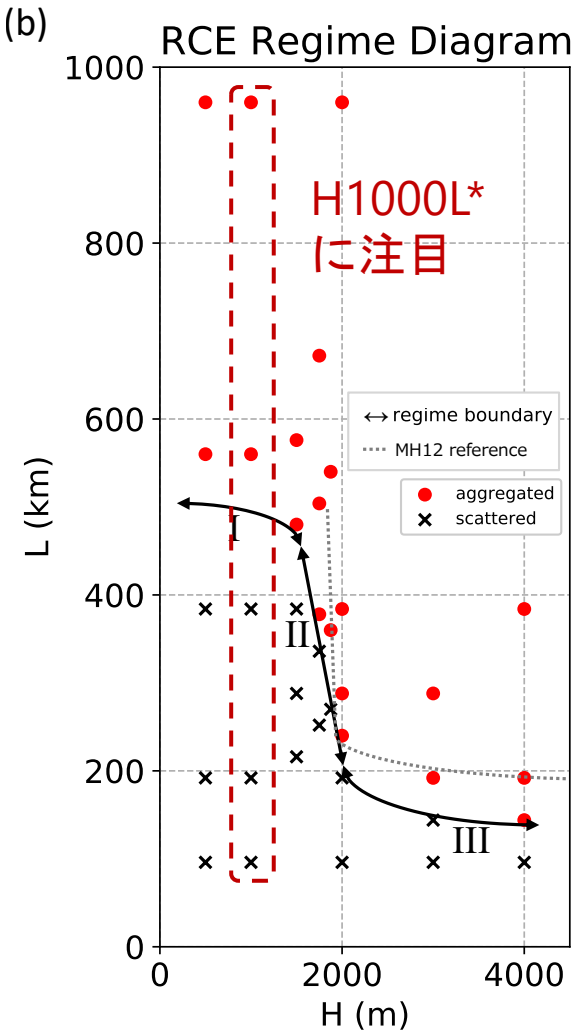

解析の焦点

- 水蒸気–高度空間の循環
  - ➢ 運動学的・力学的特徴を定量化するため，新たな流線関数・渦度源
- トリガーメカニズム (乾燥域における自由大気の下降流の境界層への貫入)
  - ➢ 弱温度勾配(WTG)近似に基づく，非断熱加熱と自由対流圏鉛直流の関係
- 放射・対流・水蒸気の水平変動性
  - ➢ 水蒸気と非断熱加熱の関係
  - ➢ 水蒸気・大気運動の水平変動性とその水平スケール

CSA発生メカニズム：水蒸気–高度空間の循環

■ 運動学的特徴：準3次元流線関数$\psi_{i,z}$

- $\Psi^{BBK05}{}_{i,z}$と異なり, 水平ソートを回避するため, 水平長さを定義可.

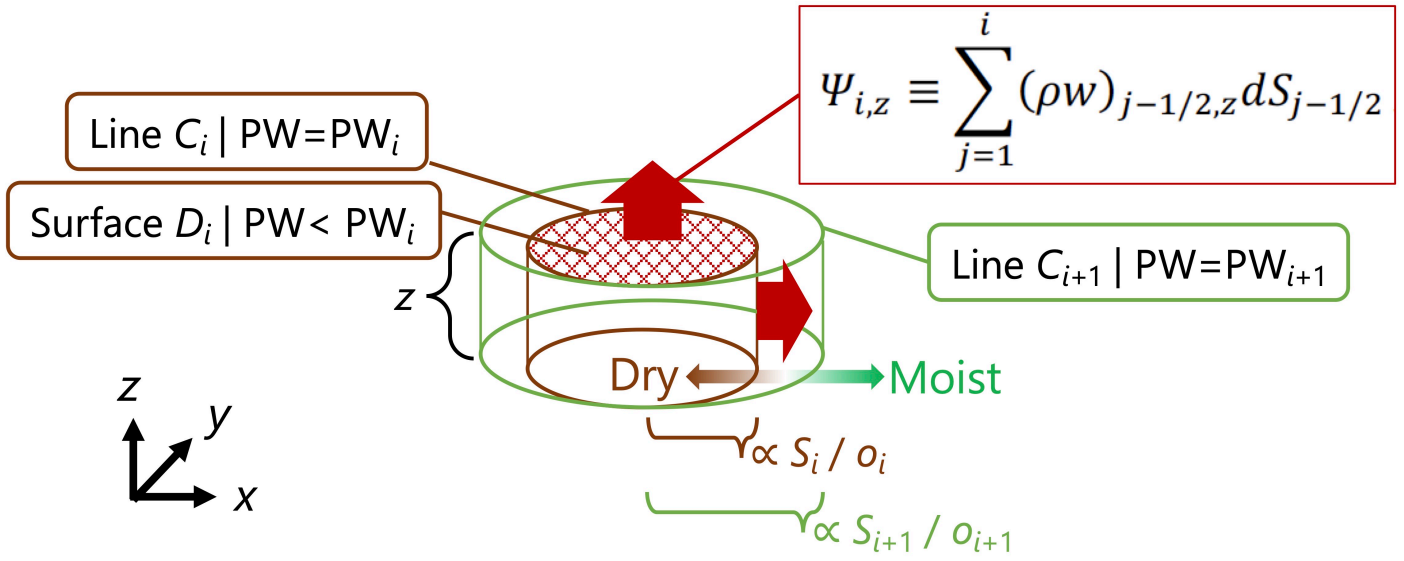

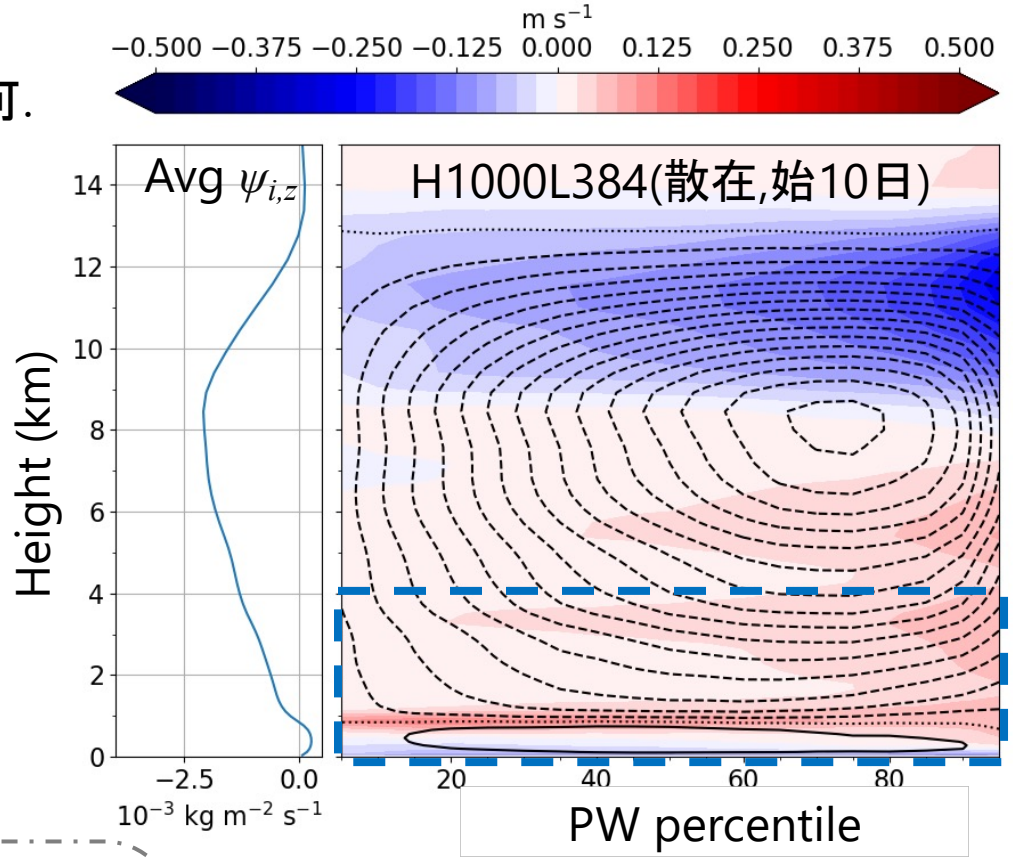

● 質量保存式
(地表面・等高度水平面・等PW鉛直面が囲う体積)

$$\oint_C \int_0^z \rho \tilde{v} dz' d\tilde{x} + \iint_D (\rho w)|_{z'=z} dS = 0$$

C : 線積分の線 (等PW線)
D : 面積分の面 (等PW線が囲う面)
$\tilde{v}$: 線Cを横切る水平風速

また, 次の様に書き, $o_i U_{i,z} + S_i W_{i,z} = 0$, 水蒸気距離 S_i/o_i を定義.

コンター:
計算領域面積で割った$\psi_{i,z}$
i: 等PW線のインデックス
破線: 負, 反時計回り循環
実線: 正, 時計回り循環

シェード:
等PW線を横切る水平風速 $\tilde{v}$

CSA発生メカニズム：水蒸気–高度空間の循環

■ 運動学的特徴の散在・集合間比較

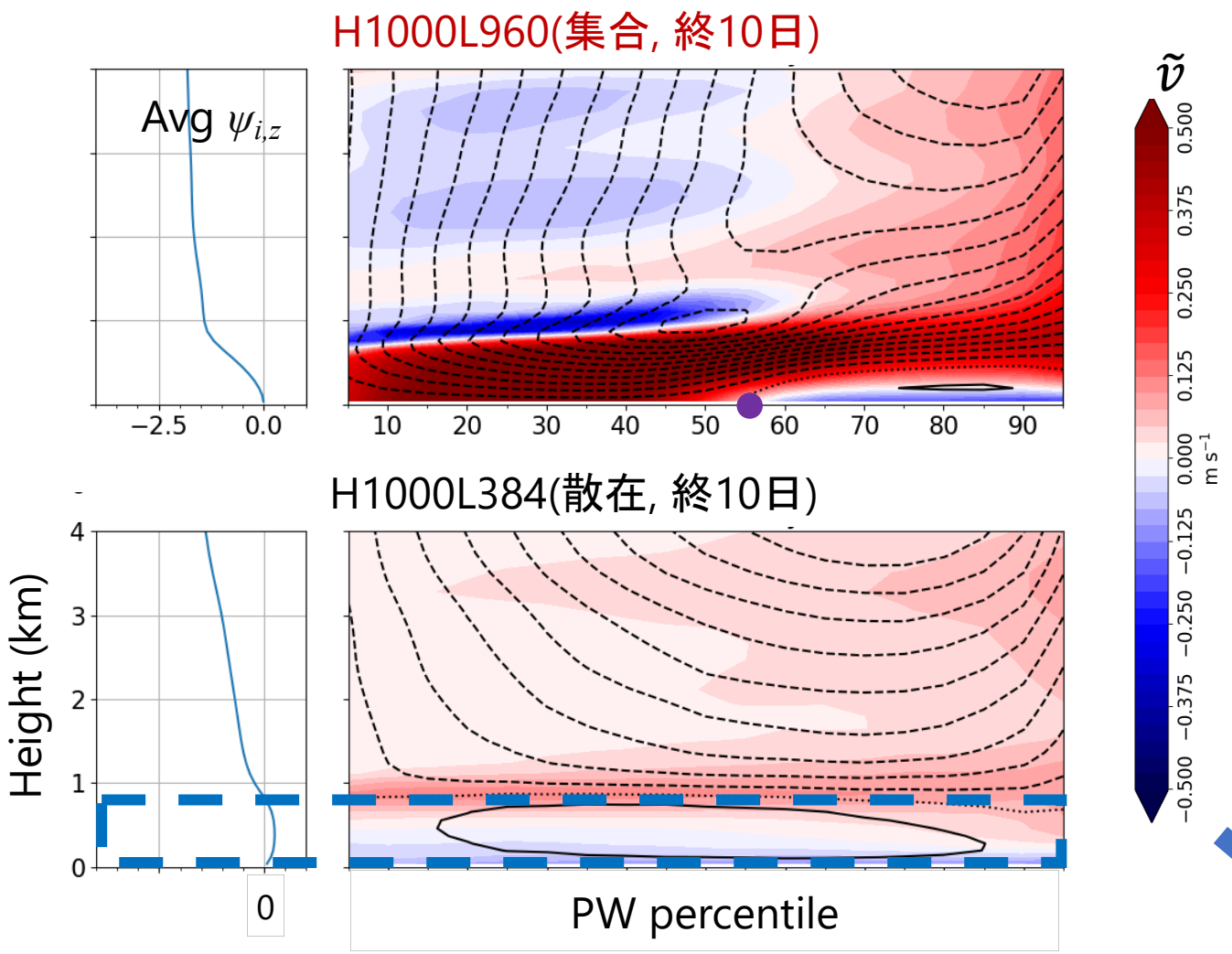

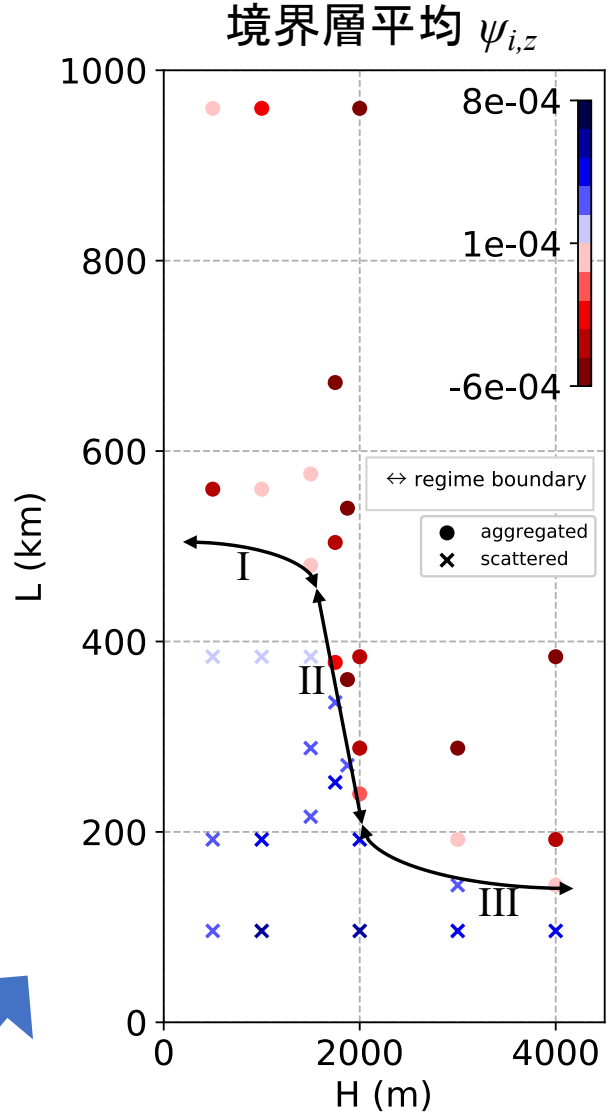

□ 散在：下層で時計回り卓越.　集合：乾燥域で, 自由大気の循環が境界層に入り, 反時計回り卓越.

□ 境界層平均Q3D-SFは, 散在は集合よりも大きな値.

CSA発生メカニズム：水蒸気–高度空間の循環

■ 力学的特徴：下層循環を駆動するトルクと放射・蒸発冷却

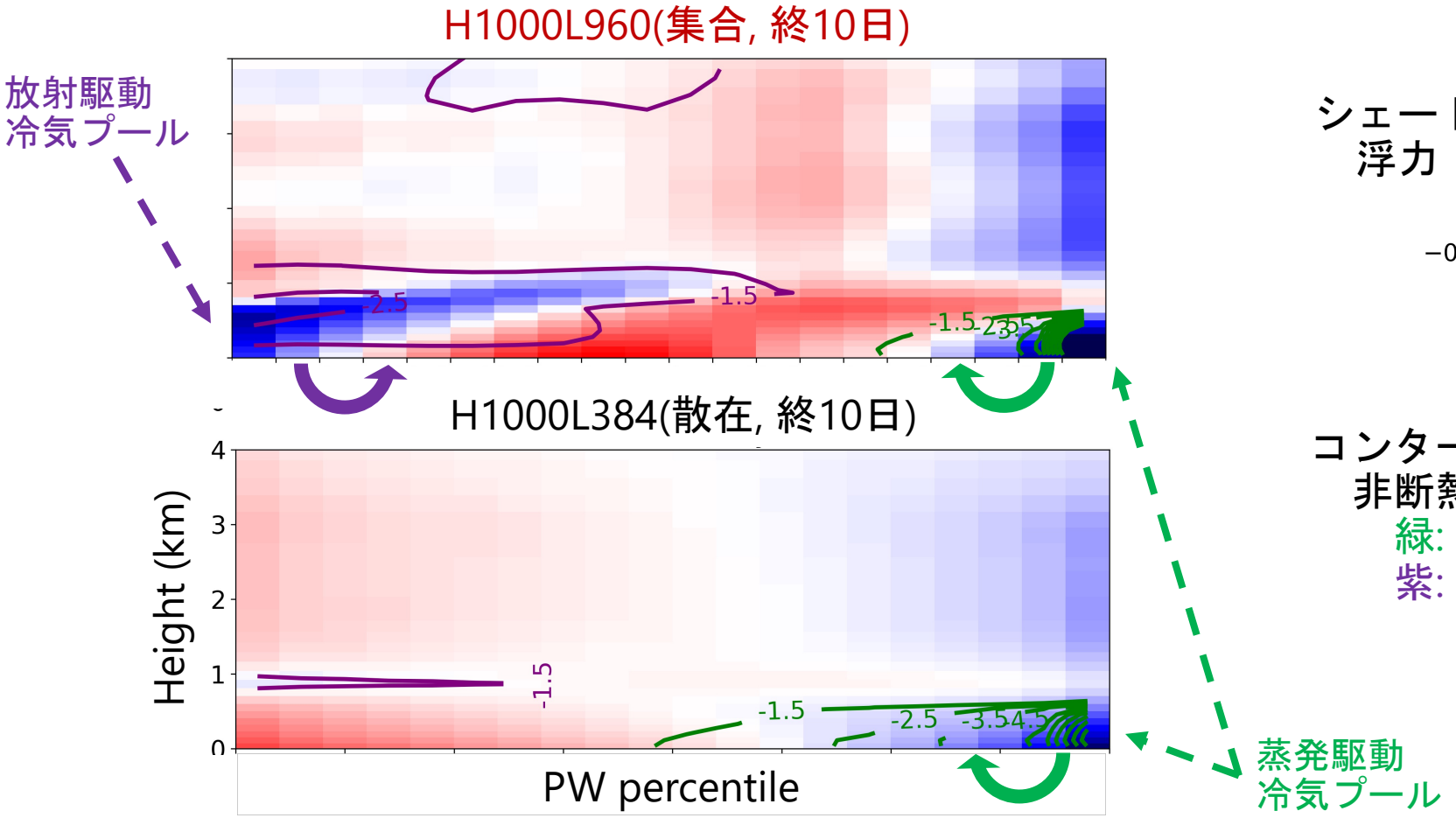

シェード:
浮力

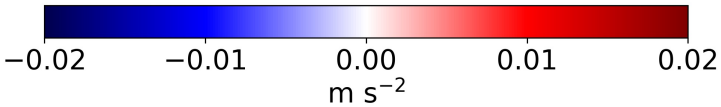

コンター:
非断熱加熱率(-1.5 kJ kg^{-1} day^{-1}以下のみ)
緑: 蒸発冷却
紫: 放射冷却

□ 湿潤域の蒸発冷却は, 散在・集合両方の下層時計回り循環を駆動.

□ 乾燥域の放射冷却は, 集合の下層反時計回り循環を駆動.

CSA発生メカニズム：水蒸気–高度空間の循環

■ 運動学・力学的特徴の時間発展(H1000L960, 集合)

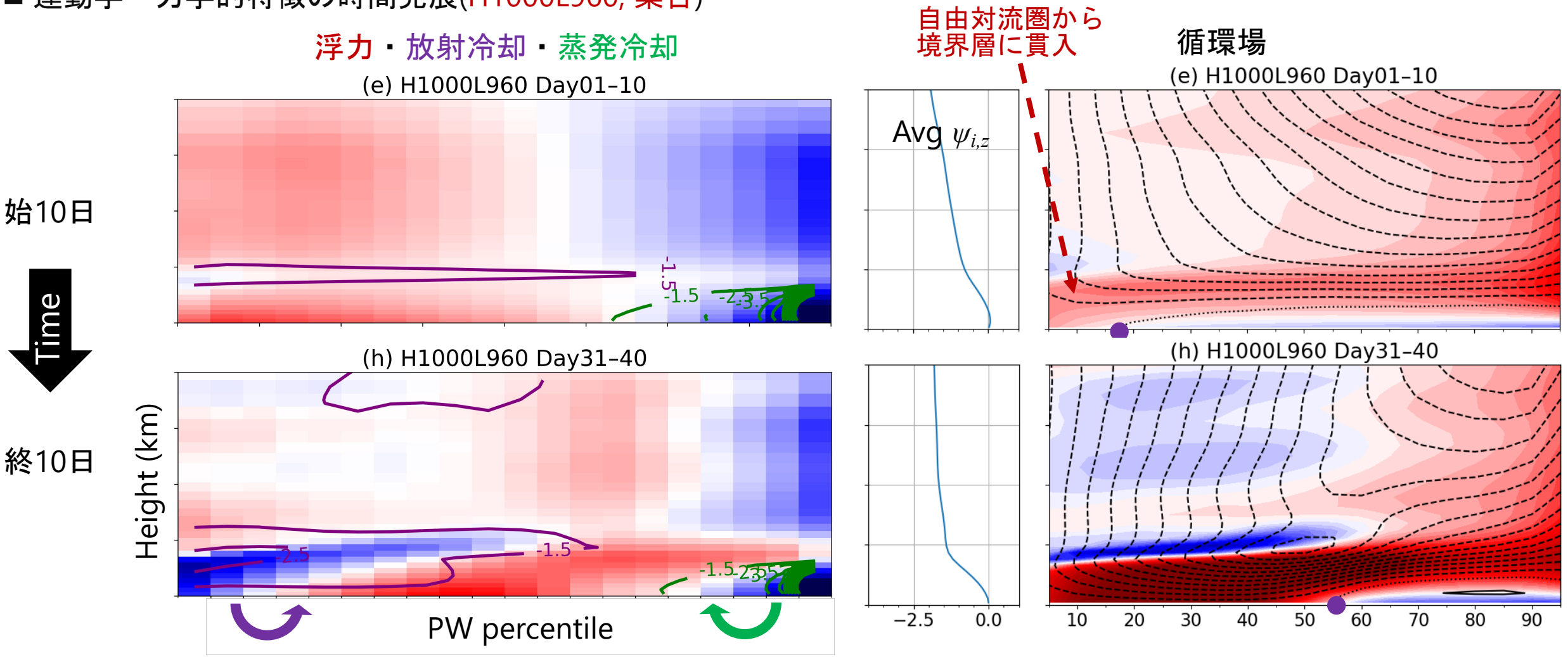

□ 乾燥域における, 放射による浮力勾配は初期(始10日)では顕著ではない.

□ 乾燥域における, 自由対流圏からの境界層への下降流の貫入が先行. → なにがこの貫入を生むのか?

CSA発生メカニズム：トリガーメカニズム

■ 乾燥域の鉛直流. 境界層上昇流と自由大気下降流の拮抗.

始10日平均
PW50%ile以下平均
鉛直マスフラックス

● 弱温度勾配(WTG)近似
  - コリオリ弱環境で有効
  - 非断熱加熱からw診断

$$w_{\mathrm{WTG}}\frac{\mathrm{d}s}{\mathrm{d}z} = Q_1$$

ここで
s ：乾燥静的エネルギー
Q_1 ：加熱率

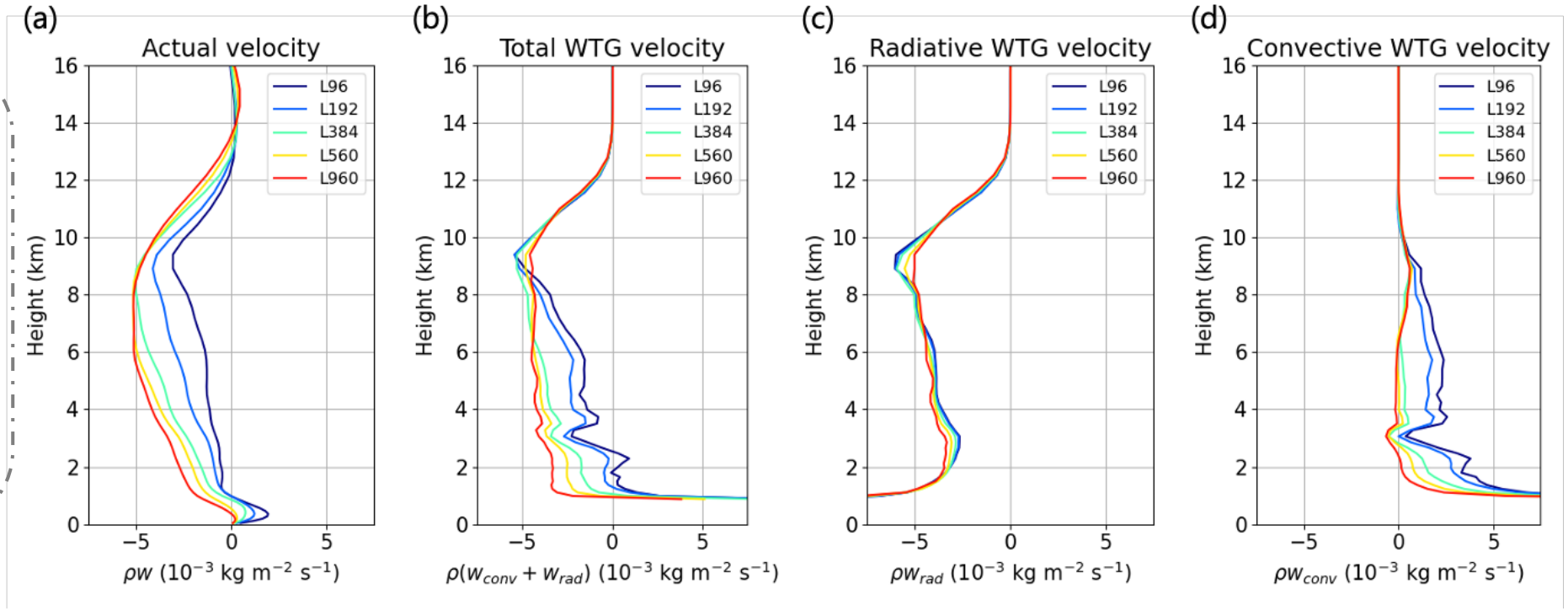

□ 放射冷却による下降流の領域幅に対する変化は小さい.

□ 対流加熱の弱化が, 正味の下降流の強化に大きく寄与. → なにがこの非断熱加熱の変動を引き起こすのか?

CSA発生メカニズム：放射・対流・水蒸気の水平変動性

■ 非断熱加熱と水蒸気量の関係

- 放射–水蒸気関係 (Bretherton et al. 2005; Beucler and Cronin 2016; etc)
- 対流–水蒸気関係 (Tompkins 2001; Takemi et al. 2004; Bretherton et al. 2005; etc)

始10日平均
高度6km以下質量重付平均
× ：PW10%ileごと平均
▲：PW50%ileごと平均

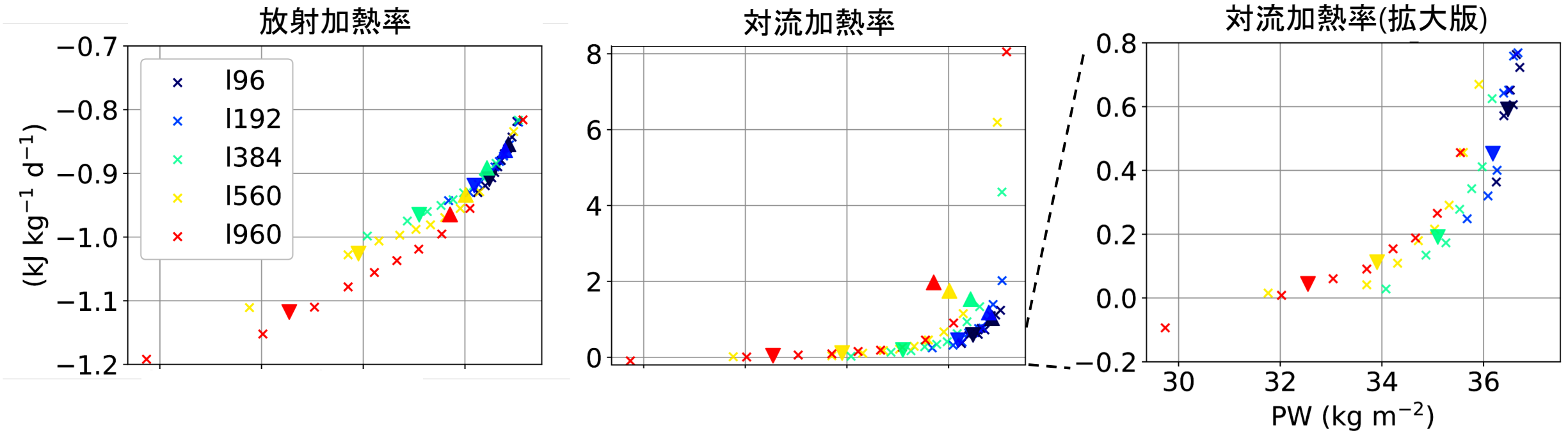

□ 放射加熱・対流加熱ともに, 水蒸気に対して単調増加. 実験間のばらつきはあるものの, 似た様な曲線にのる.

□ 水蒸気の変動幅の増加に伴い, 加熱の変動幅が増加している.

CSA発生メカニズム：放射・対流・水蒸気の水平変動性

■ 水蒸気変動性の水平スケール

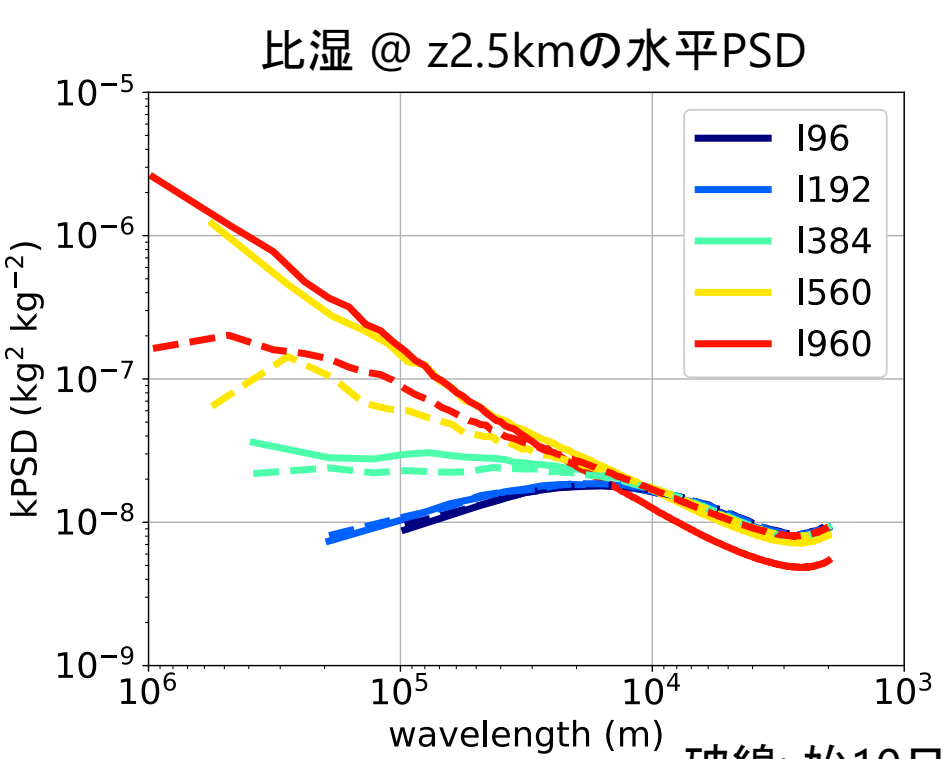

破線: 始10日平均
実線: 終10日平均
PSDに波数kを乗ずる

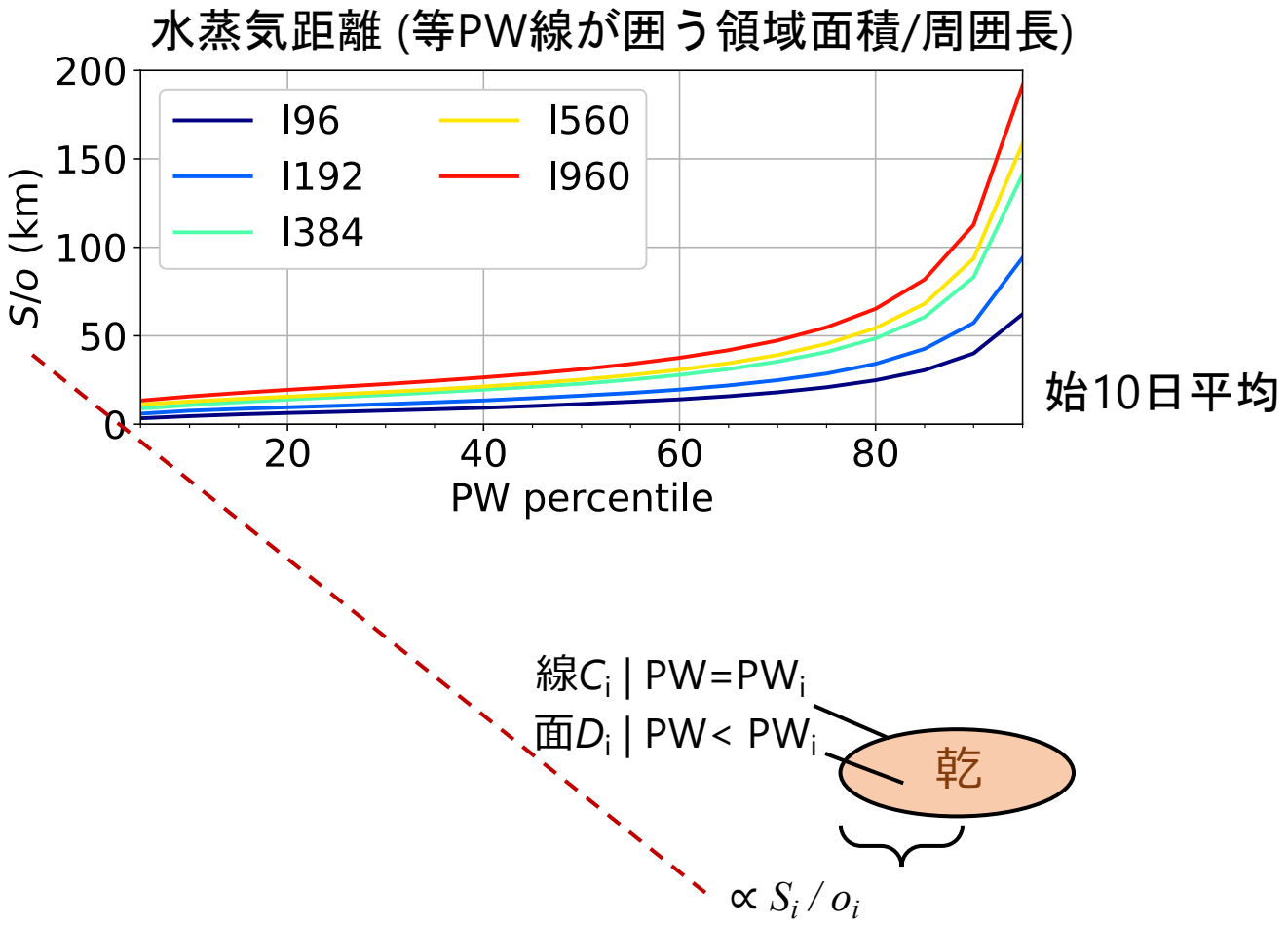

- 領域幅増加とともに, 長波長により多くのパワー. 水平分散の増加に寄与.
- 領域幅増加とともに, 水蒸気距離(乾燥域から湿潤域までの距離)も, いずれのPW%ileにおいても増加.

CSA発生メカニズム：放射・対流・水蒸気の水平変動性

■ 大気運動の水平スケール

水平成分 @ z2.5kmの水平PSD

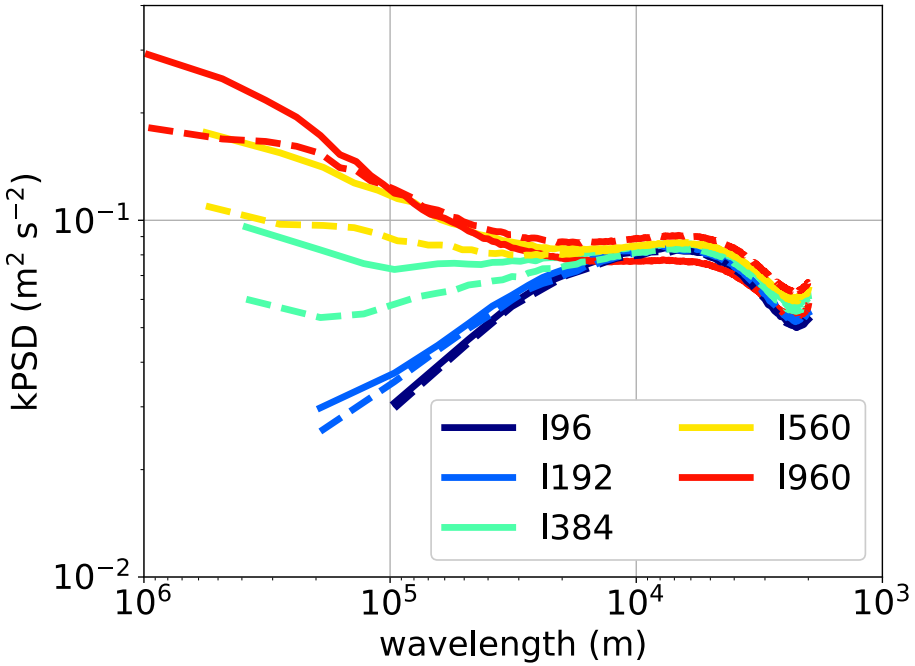

鉛直成分 @ z2.5kmの水平PSD

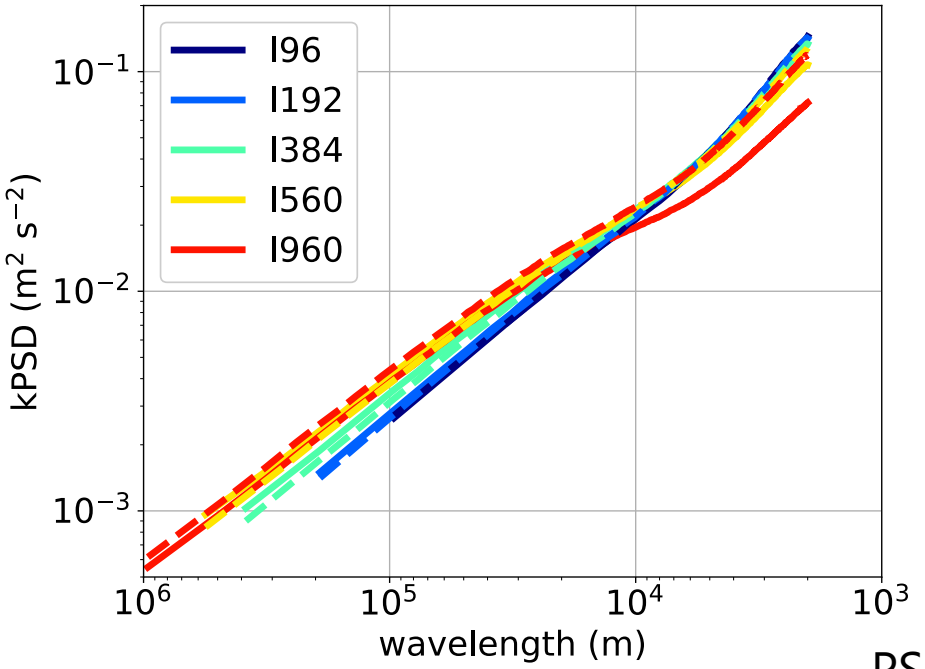

破線: 始10日平均
実線: 終10日平均
PSDに波数kを乗ずる

- 水平成分: 領域増加とともに, 長波長により多くのパワー. 水蒸気と類似.
- 鉛直成分: どの実験でも, 短波長にパワー多く持つ. 領域増加とともに, 長波長のパワー少し増加.

- 散在レジーム: 小規模・鉛直・対流運動が卓越
- 集合レジーム: 大規模・水平・循環運動が卓越

CSA発生メカニズム：まとめ

- 湿潤対流の自己集合化の発生メカニズムを調査するために, RCE実験の領域幅依存性を調査.
- 散在状態と集合状態は, 下層循環パターンに明確な違い. 乾燥域の放射冷却が作る浮力勾配が重要.
- 集合状態への遷移のトリガーは, 乾燥域における自由大気から境界層への鉛直貫入.
- 乾燥域における正味の下降流の強化は, 対流加熱の弱化が直接的要因. 放射冷却は間接的要因.
- 対流加熱は水蒸気量と結び付いており, 水蒸気変動及び水平運動は領域幅相当の最大水平スケールで規定される.

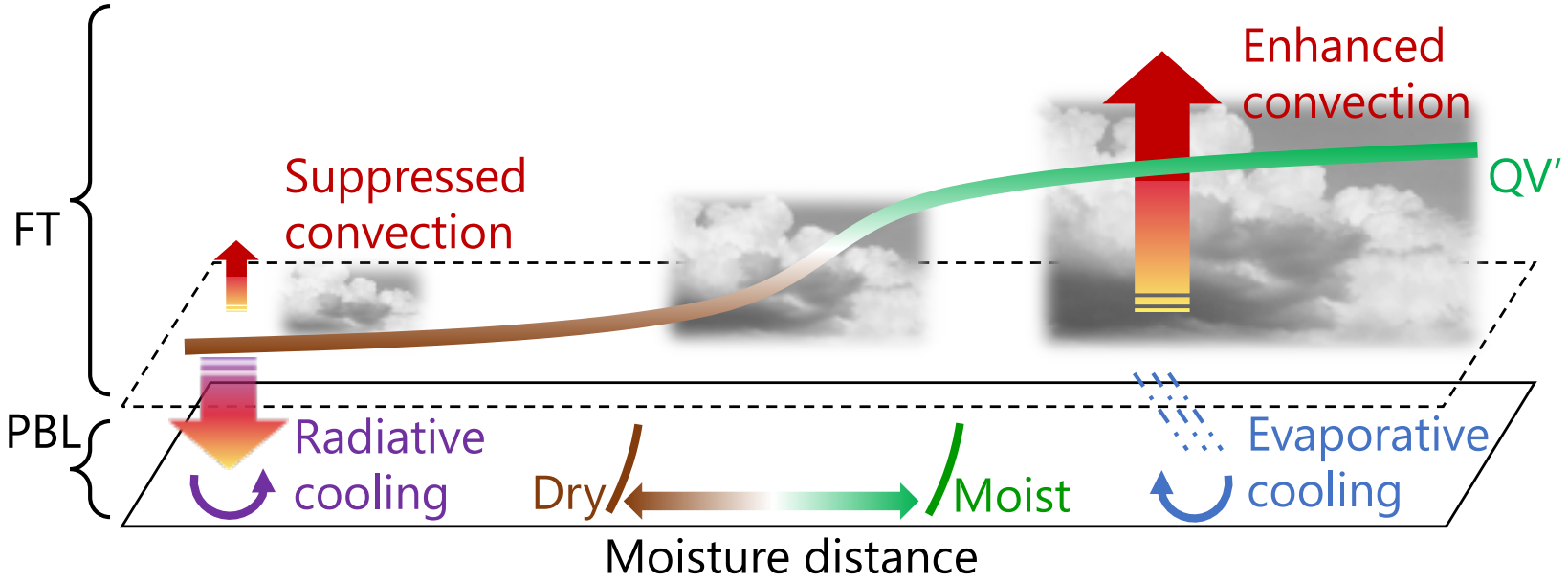

目次

① **Yanase, T.**, Nishizawa, S., Miura, H., Takemi, T., & Tomita, H. (2020).
New critical length for the onset of self-aggregation of moist convection. *Geophys. Res. Lett.* **[published; 主に3章の内容]**

② **Yanase, T.**, Nishizawa, S., Miura, H., Takemi, T., & Tomita, H. (2021).
Low-level circulation and its coupling with free-tropospheric variability as a mechanism of spontaneous aggregation of moist convection. *J. Atmos. Sci.* **[under review; 主に4章の内容]**

総括

■ 結語

- 対流の組織化・集合化は, 気候における雲の役割をより深く理解するための鍵.
- CSAはどのような条件(e.g., 空間スケール)で発生するのか?
  - CSA発生条件・メカニズムを理解するため, 水平領域幅・水平格子幅を変えたRCE実験.
  - 水平領域幅約500km以上でCSA発生. メソαスケール以上で重要なプロセスであることを示唆.
  - 下層の流れが拮抗し, 逆勾配的な下層水平水蒸気輸送が卓越するとCSA発生.
- CSAはその空間スケールに関連してどのようなメカニズムで発生するのか?
  - 散在・集合間で下層循環パターンに明瞭な違いがあることを定量化.
  - 乾燥域の下降流の境界層への貫入がトリガー要因で, 放射冷却による浮力勾配が発達要因.
  - 乾燥域の下降流の強化は対流加熱の弱化に起因し, 対流加熱の弱化は水蒸気量の水平分散の増加に起因.
  - 水蒸気量及び水平運動の変動性は, 長波長からの寄与が大きく, 水平領域幅による制約を受ける.

● 水蒸気の水平変動性, 放射・対流, および下層循環を統合し, 雲の組織化メカニズムに関する新たな視点を提示.

■ 展望

- 集合化した対流が複数共存する実験(e.g., 水平領域数千~万km)を行うことで, 「自然な」特徴空間スケールの特定.
- 力学的制約(e.g., コリオリ力)や熱力学的制約(e.g., SST勾配)を与えることで, 組織化形態の遷移の理解.

謝辞・文献

- 本研究が用いた大気モデルSCALE Version 5.3.3を提供していただいたTeam SCALEに感謝します.
- 本研究の数値実験には理化学研究所「京」コンピュータ(Project ID: hp170323), 京都大学学術情報メディアセンターおよび東京大学情報基盤センターのスーパーコンピュータを利用しました.
- 本研究は理化学研究所 大学院生リサーチ・アソシエイト制度の下での成果です.
- 本研究は科研費(21H01591, 19H01974)の助成を一部受けたものです.

① **Yanase, T.**, Nishizawa, S., Miura, H., Takemi, T., & Tomita, H. (2020). New critical length for the onset of self-aggregation of moist convection. *Geophys. Res. Lett.*, **47**, https://doi.org/10.1029/2020GL088763.

② **Yanase, T.**, Nishizawa, S., Miura, H., Takemi, T., & Tomita, H. (2021). Low-level circulation and its coupling with free-tropospheric variability as a mechanism of spontaneous aggregation of moist convection. *J. Atmos. Sci.* [under review]

ご静聴ありがとうございました

補足

年代順的なRCE研究と使用モデル階層(1/2)

※必ずしも網羅的ではない

■ 1990年代まで

Tao et al. (1999)によるまとめ

	Model	Domain (dx)	Large-scale forcing	time (days)	Case
①	Nakajima and Matsuno (1988)	2D No ice	512 km (1000 m)	Constant radiative cooling	2.5	East Atlantic
	Islam et al. (1993)	3D	60 × 60 km² (2000 m)	Constant radiative cooling	4	West Indies
②	Held et al. (1993)	2D 3 ice	640 km (5000 m)	Cloud-radiative forcing	42	Tropics
	Sui et al. (1994); Lau et al. (1993); Lau et al. (1994)	2D 3 ice	768 km (1500 m)	Large-scale velocity and radiative forcing	52	West Pacific
	Randall et al. (1994)	2D 3 ice	256 km (2000 m)	Radiative forcing	100	East Atlantic
	Grabowski et al. (1996)	2D 2 ice	900 km (1000 m)	Large-scale velocity and radiative forcing	25	West Pacific
	Robe and Emanuel (1996)	3D No ice	60 × 60 km² (2000 m)	Constant radiative cooling	6–30	West Indies
③	Tompkins and Craig (1998)	3D 3 ice	100 × 100 km² (2000 m)	Cloud-radiative forcing	70	Radiative–convective equilibrium
	Xu and Randall (1999)	2D 3 ice	512 km (2000 m)	Constant forcing in T and Q_v and radiative forcing	29	West Pacific and East Atlantic

Time

- 放射：一定冷却(/ニュートン冷却)① / 放射伝達②,③
- 運動：2次元①,② / 3次元③

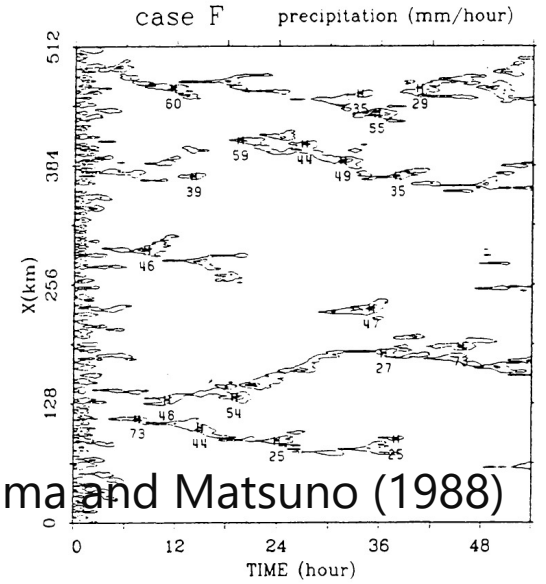

Nakajima and Matsuno (1988)

Fig. 8. Time evolution of horizontal distribution of surface precipitation intensity in case F. The maximum value is 73 mm/hr.

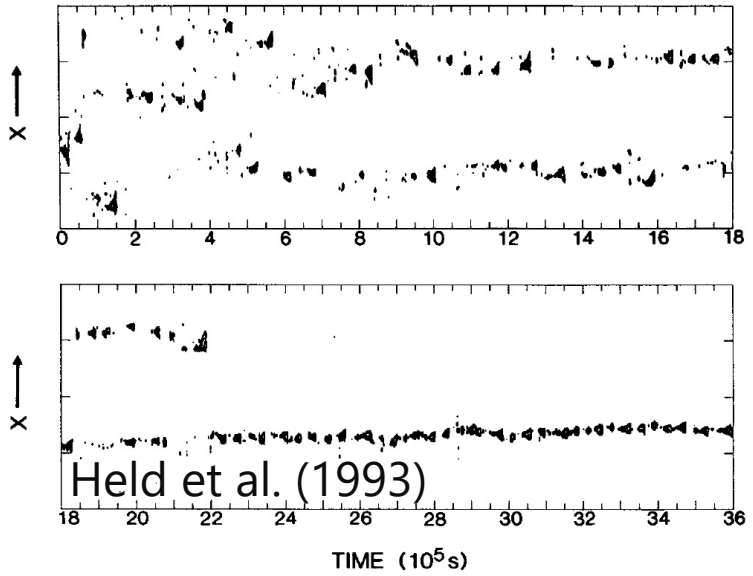

Held et al. (1993)

FIG. 4. Precipitation as a function of time and x in the case in which the mean wind is constrained to vanish.

Tompkins and Craig (1998)

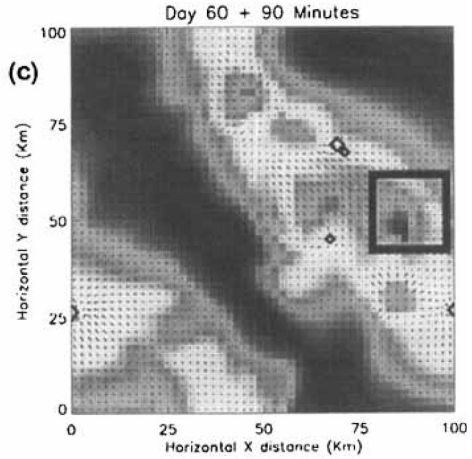

Figure 6. Water-vapour mixing ratio in the lowe (c) 90 and (d) 135 minutes later. Horizontal velo in all four pictures does not exceed 7 m s^{-1}). The indicate the areas of deep convective activity with the moist band caused by the do

年代順的なRCE研究と使用モデル階層(2/2)

※必ずしも網羅的ではない

■ 2000年代

Bretherton et al. (2005) Self-aggregation発現に関して放射・地表水平均一化実験, 領域幅実験など色々やった.

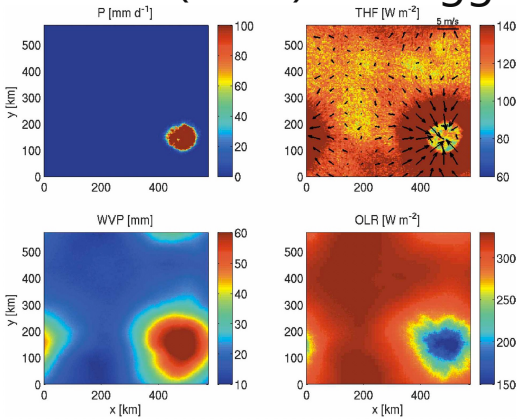

FIG. 3. As in Fig. 1, but for day 50.

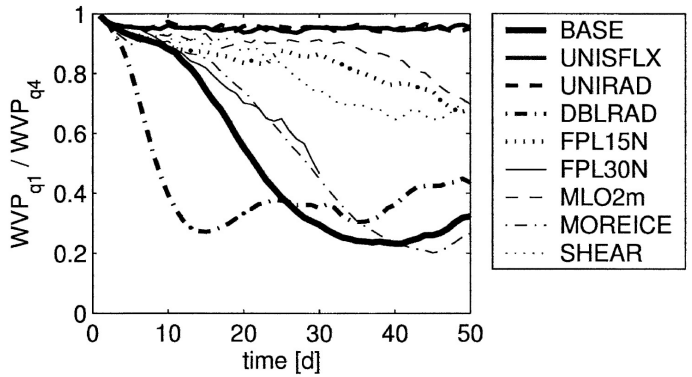

FIG. 13. Time series of daily averaged WVP interquartile ratio for the base simulation and several sensitivity studies to changed model physics.

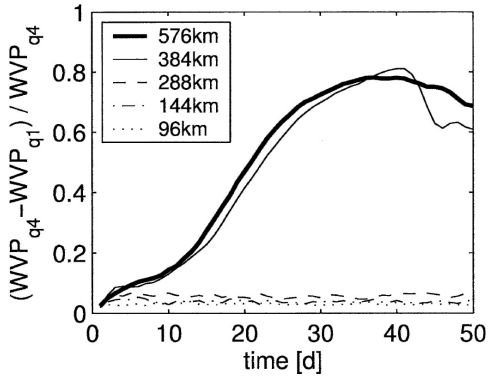

FIG. 12. Time series of daily averaged WVP interquartile ratio for BASE-like simulations with a range of domain sizes.

Tompkins (2001) チャネル領域； Nolan et al. (2007) f面RCE； Satoh and Matsuda (2009) 小惑星RCE； …

■ 2010年代以降

Khairoutdinov and Emanuel (2010); Muller and Held (2012); Craig and Mack (2013); Jeevanjee and Romps (2013); Wing and Emanuel (2014); Muller and Bony (2015); Coppin and Bony (2015); Arnold and Randall (2015); Reed et al. (2015); Wing and Cronin (2016); Holloway and Woolnough (2016); Hohenegger and Stevens (2016); Cronin and Wing (2017); Becker et al. (2018); Yang (2018); Haerter (2019); Windmiller and Craig (2019); **Yanase et al. (2020);** Wing et al. (2020), …

- 領域：Regional / Global
- 積雲：雲解像 / スーパーパラ / 積雲パラ
- 自転：f=0 / f≠0 / コリオリ
- 海面：Fixed SST / Interactive SST

最近のレビュー論文：Wing et al. (2017), Holloway et al. (2017), Muller et al. (2022)

補足：気候モデルの階層

“A perspective on climate model hierarchies” (Jeevanjee et al. 2017, JAMES)

モデルを構成する要素に関する”軸”を導入し, 包括性・複雑性の観点から整理.

RCEは境界強制を単純化した枠組み

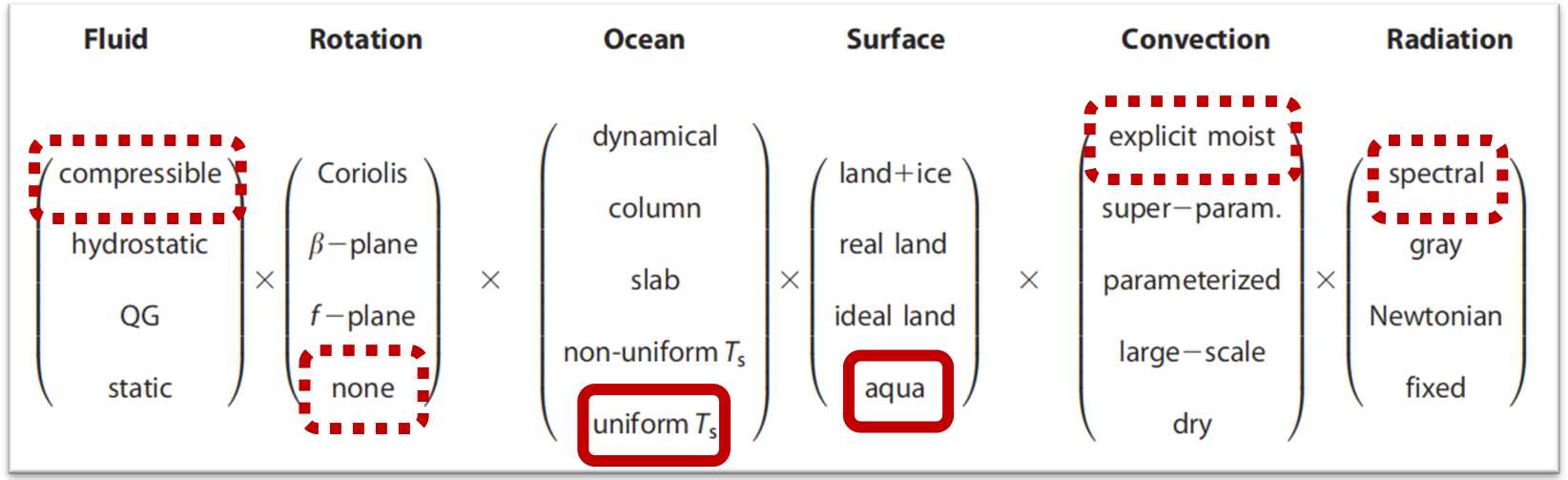

$$\underbrace{\text{Fluid} \times \text{Rotation}}_{\text{Dynamics}} \times \underbrace{\text{Ocean} \times \text{Surface}}_{\text{Boundary Forcing}} \times \underbrace{\text{Convection} \times \text{Radiation}}_{\text{Bulk Forcing}}, \qquad (2)$$

補足：準3次元流線関数と運動量の回転

$$\hat{\Psi} \equiv \int_{\tilde{Y}_{roof}} \rho w d\tilde{y} = -\int_{Z_{wall}} \rho \tilde{v} dz$$

$$\eta \equiv \frac{\partial \bar{\rho} w}{\partial \tilde{y}} - \frac{\partial \bar{\rho} \tilde{v}}{\partial z}$$

$$\left(\frac{\partial^2}{\partial \tilde{y}^2} + \frac{\partial^2}{\partial z^2} \right) \hat{\Psi} = \eta$$

$$\Psi \propto \hat{\Psi} \propto -\eta$$

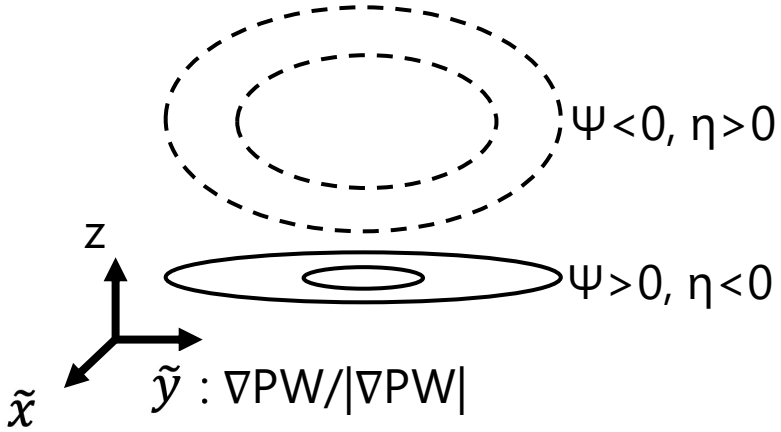

省略した内容の概要

■ 第2章: 数値モデル及び実験設定

- コントロールラン(H2000L96, 100日積分)の結果
  - 1ヶ月程度で準平衡状態に到達.
  - 準平衡状態における特徴量(e.g., OLR, PW)はRCEMIPモデルアンサンブル平均±1標準偏差範囲内.

■ 第3章: CSA発生条件

- 鉛直解像度依存性の検証
  - 鉛直層数半減/倍増実験. 鉛直層数によらず高解像度広領域においてCSAが発生.
- SGS乱流スキーム依存性の検証
  - 境界層パラメタリゼーション(MYNNスキーム)使用実験. SGS乱流スキームによらず広領域においてCSAが発生.

■ 第4章: CSA発生メカニズム

- 下層循環の力学的要因
  - 準3次元流線関数と整合的な渦度方程式に基づくトルクの解析. 浮力勾配と摩擦のバランスで循環が時間発展.
- トリガーメカニズム
  - 乾燥域下降流の半経験的鉛直モード分解. 領域幅増加に伴い, bottom-heavyになり, 境界層循環が相対的に弱化.
- 非断熱加熱の変動性と水平スケールの関係
  - 対流コア水平分布の解析. 領域幅増加に伴い, 下降流域サイズ増加.

博論図一覧

図1.1: 全球的なエネルギーの流れ

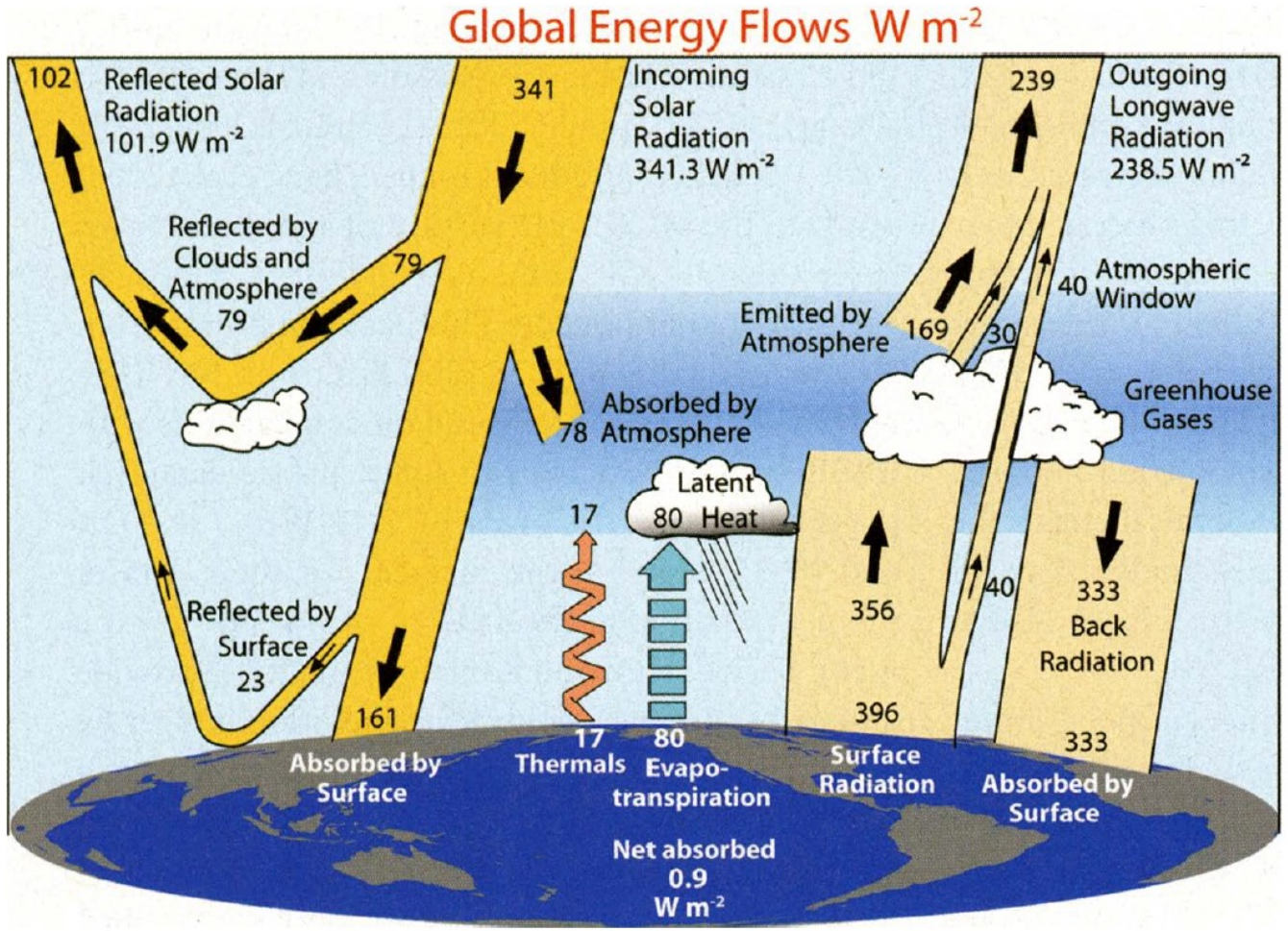

Global energy flow. Net solar shortwave radiative heating and net terrestrial longwave radiative cooling of Earth, respectively, are estimated as 239.4 W m−2 and 238.5 W m−2. Net shortwave heating and net longwave cooling of the atmosphere, respectively, are estimated as 78.2 W m−2 and 175.5 W m−2; the net radiative cooling of the atmosphere is 97.3 W m−2. Sensible and latent heat fluxes from the ground surface to the atmosphere, respectively, are estimated as 17 W m−2 and 80 W m−2. The estimates are derived in Mar 2000 to May 2004, the period covered by the Clouds and the Earth's Radiant Energy System. After Trenberth et al. (2009) Fig. 1.

図1.2: 放射・水–大気循環の間の結合の概念図

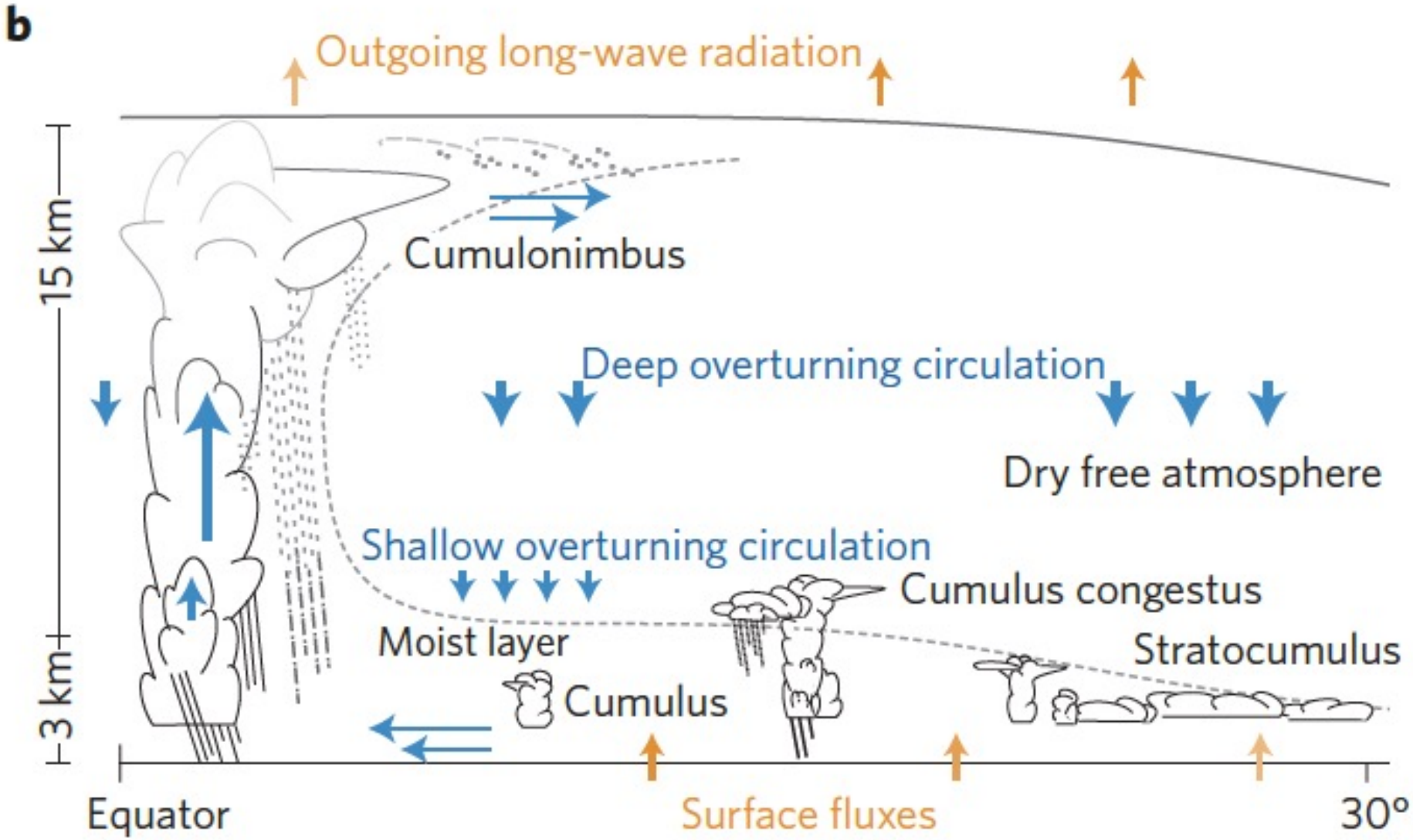

Schematic of the coupling among the radiation, water cycle, and atmospheric circulation. After Bony et al. (2015) Fig. 1b.

図1.3: 雲表現に起因した気候モデルの不確実性

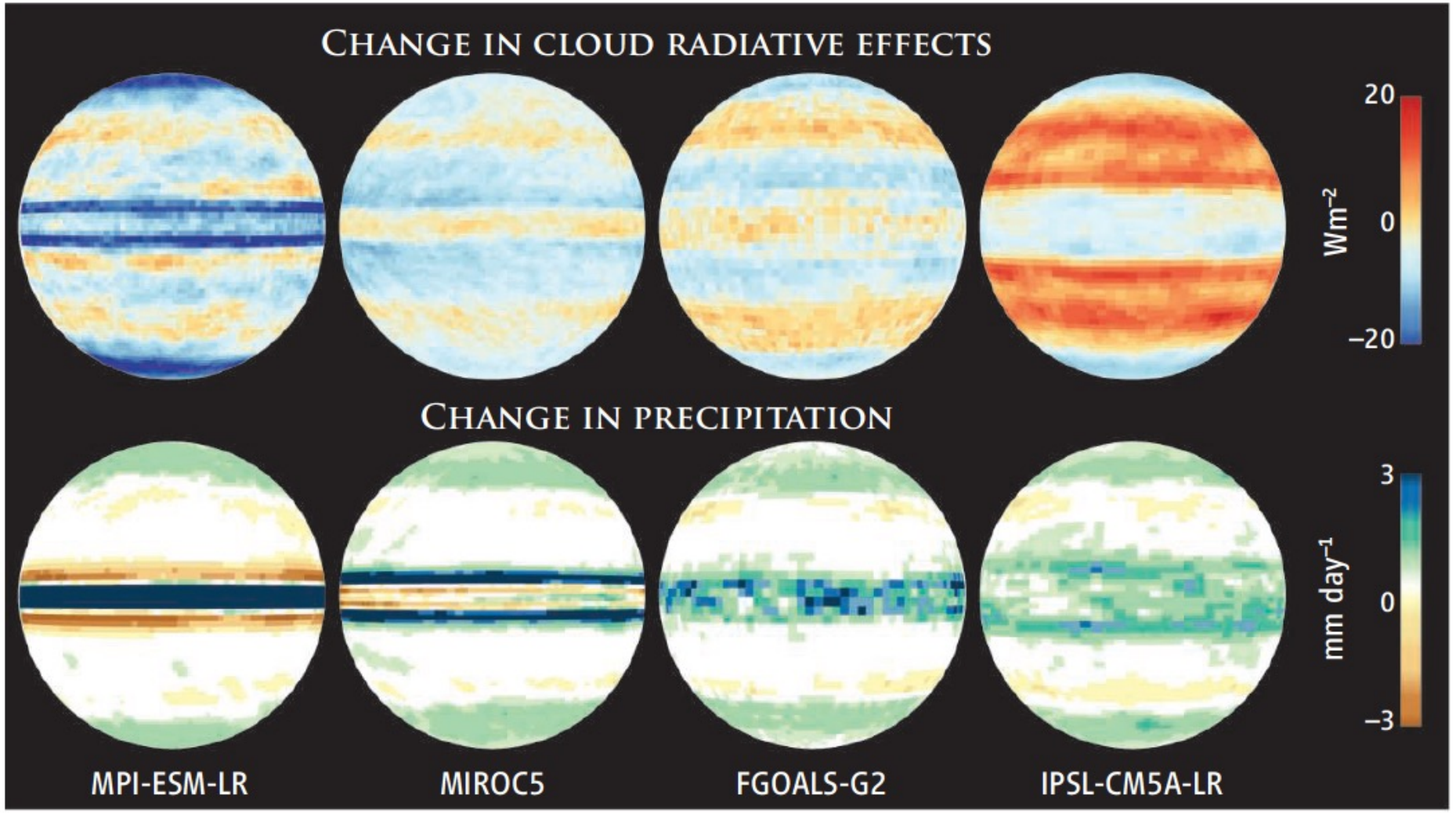

Uncertainty of climate models originated from cloud-related process. The response of cloud radiative effects and precipitation to uniform warming of 4 K under aquaplanet condition simulated by four different models from Phase 5 of the Coupled Model Intercomparison Project (CMIP5). After Stevens and Bony (2013).

図1.4: 気候における組織化対流の役割

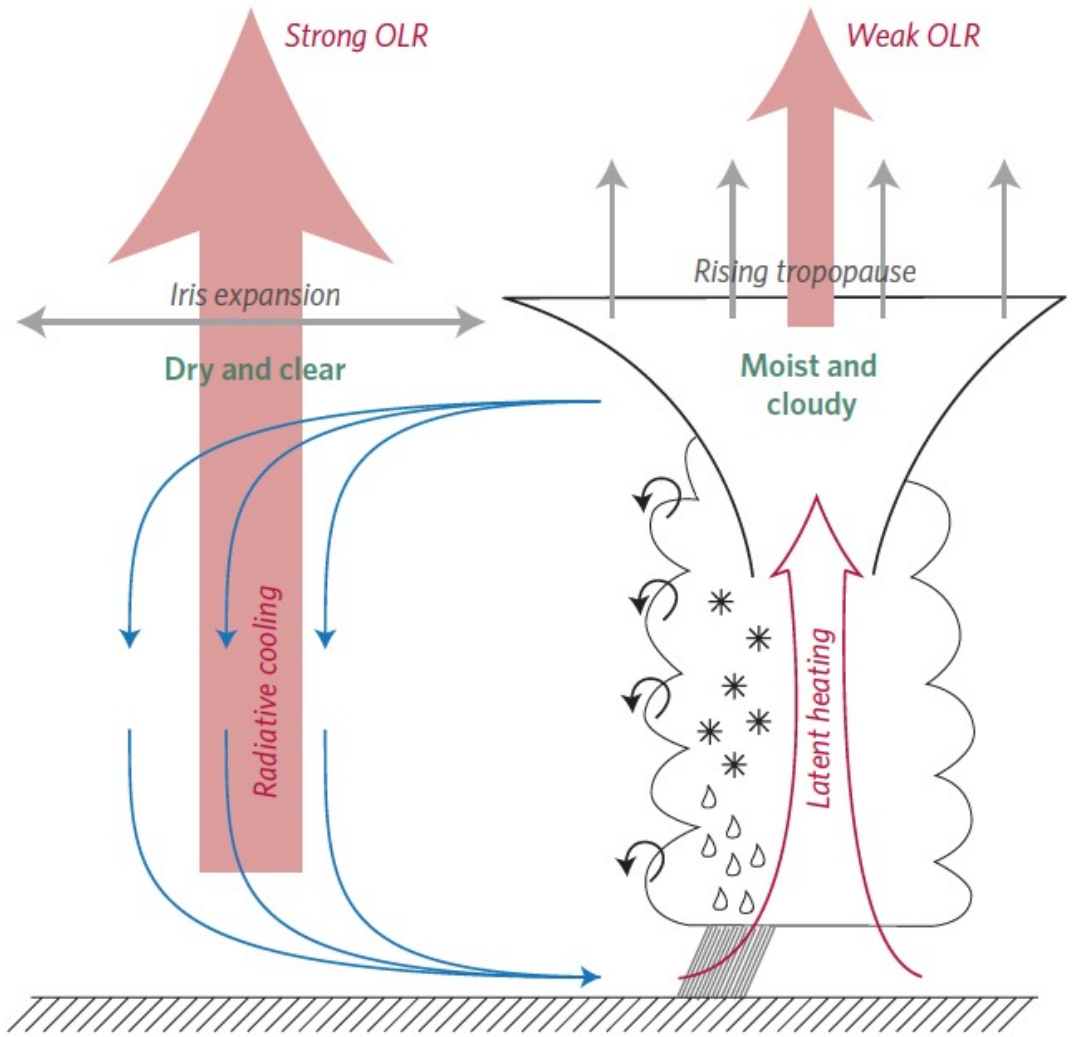

Possible role of organized convection on the climate feedback. If the outgoing longwave radiation increases associated with the response of the convective organization (or aggregation) to the warming, the process may act as negative feedback to the warming. After Mauritsen and Stevens (2015) Fig. 1.

図1.5: 熱帯大気で観測される雲クラスター

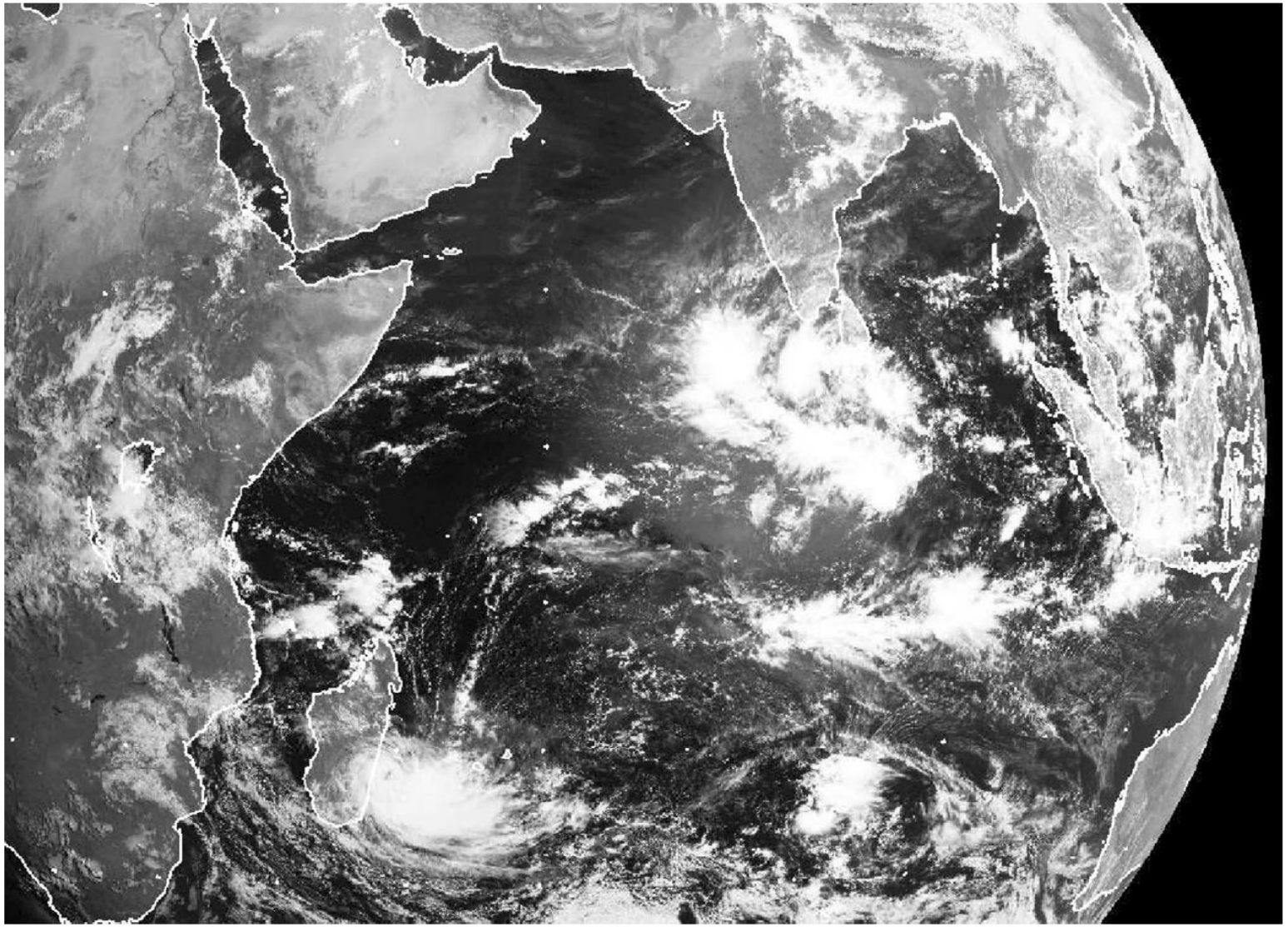

Cloud cluster observed in the tropical atmosphere. On 8 April 2009, during an active Madden–Julian Oscillation event. After Holloway et al. (2017) Fig. 1.

図1.6: 対流の自己集合化の例

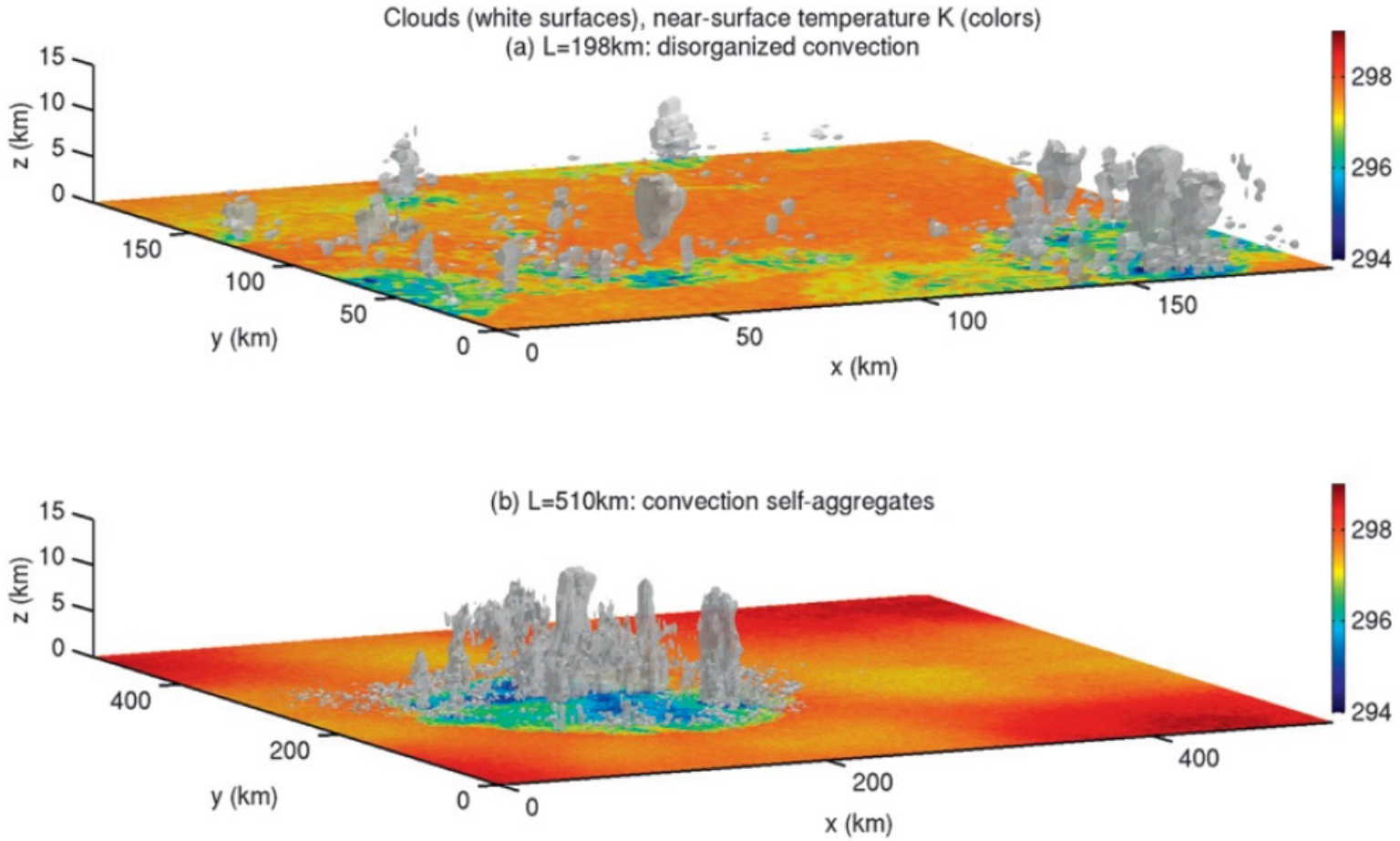

An example of the convective self-aggregation. In the numerical experiments of RCE under uniform sea surface temperature and uniform solar insolation, moist convection usually exhibits near random distribution (top; scattered state), but under certain condition it spontaneously organizes into the cloud cluster with coherent structure (bottom; aggregated state). After Muller and Held (2012) Fig. 1.

図1.7: 対流の集合化・放射・水蒸気関係の観測

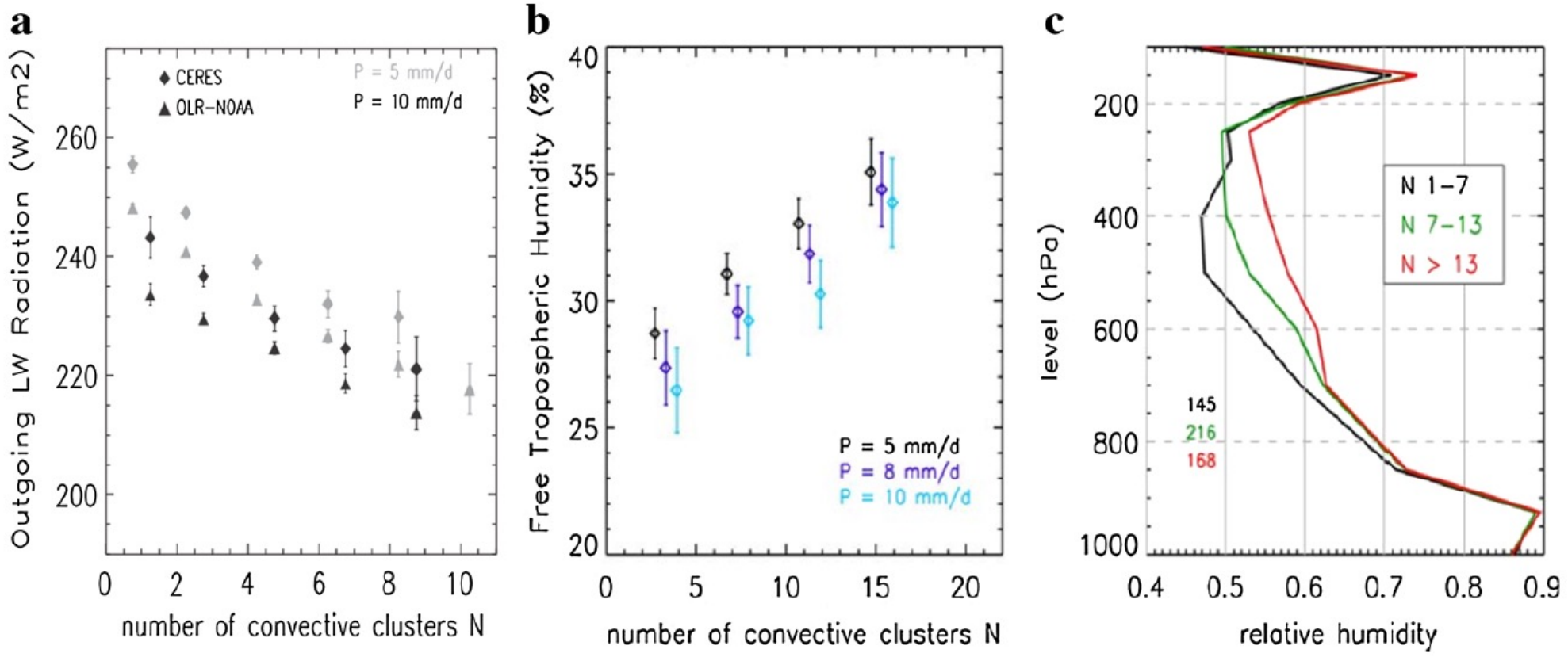

Observational evidence for the relationship among the convective aggregation, radiation, and moisture. (a) The relationship between number of convective clusters and outgoing longwave radiation for the satellite-derived samples covering a 10 ° by 10 ° area with certain precipitation amount. (b) As (a), but for free-tropospheric humidity of 3 ° by 3 ° samples. (c) As (b), but for the vertical profile of relative humidity of 8 mm day−1 samples. The smaller number of clusters, the more aggregated state. After Holloway et al. (2017) Fig. 2.

図1.8: 水平格子幅–領域幅に対するRCEレジーム

Where is the regime boundary?
What determines it?

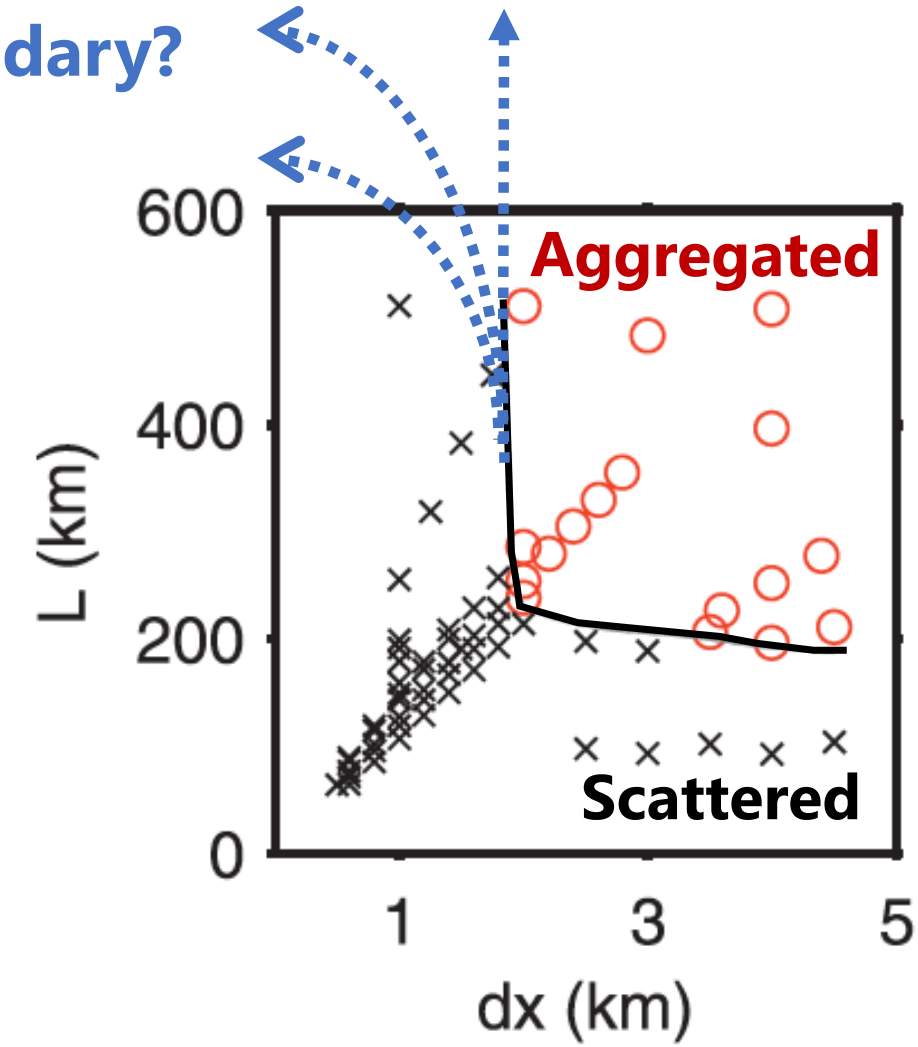

RCE regime in horizontal grid spacing–domain size parameter. After Muller and Held (2012) Fig. 6a modified by the author.

図1.9: 放射駆動冷気プールの役割

(a) RCE under enhanced rad. cooling in low-level dry-region

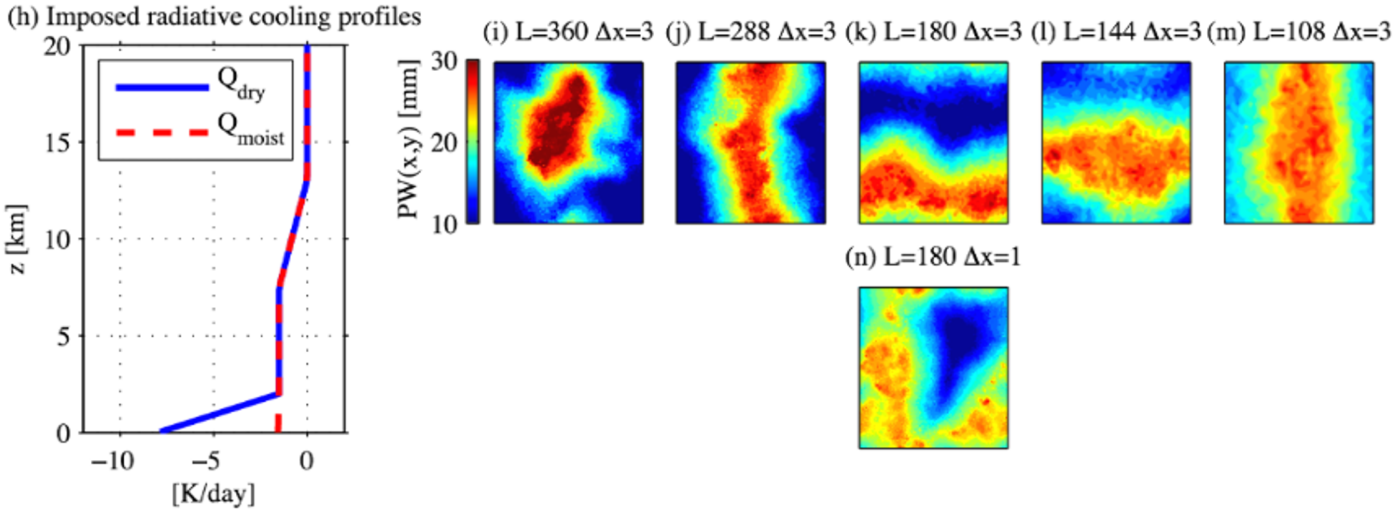

(b) Radiative cold pool

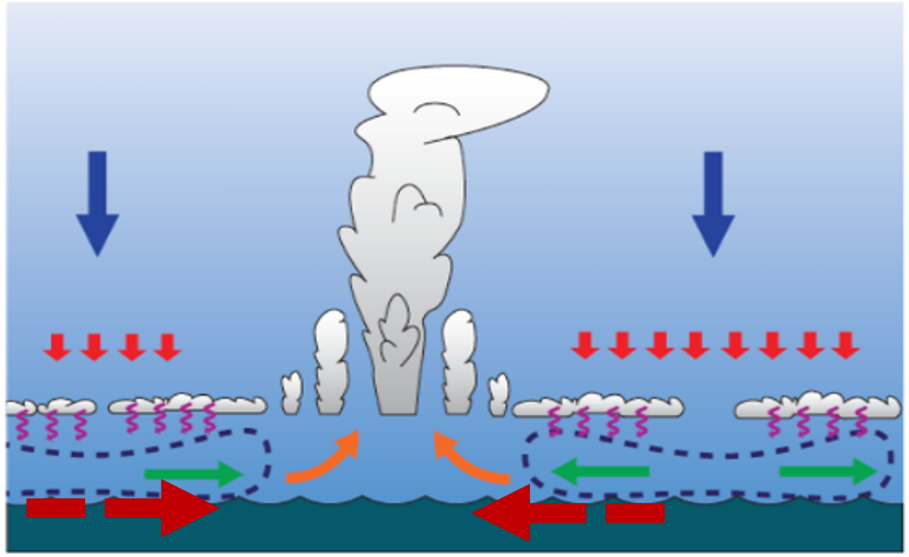

Schematic of the role of radiatively driven cold pools. (a) Vertical profile of imposed radiative cooling in the moist and dry regions (left). The cooling is strengthened below 2 km height in the dry region. Horizontal distribution of precipitable water in RCE experiments with different domain sizes (right-upper 4 panels; the domain size increases right to left). A high-resolution experiment is also shown (right-lower panel). After Muller and Bony (2015) Fig. 1. (b) Schematic of the radiatively driven cold pool. The cold pool horizontally transports moisture from the dry subsidence region to the moist convective region (red dashed arrows). After Coppin and Bony (2015) Fig. 13a.

図1.10: 蒸発駆動冷気プールの役割

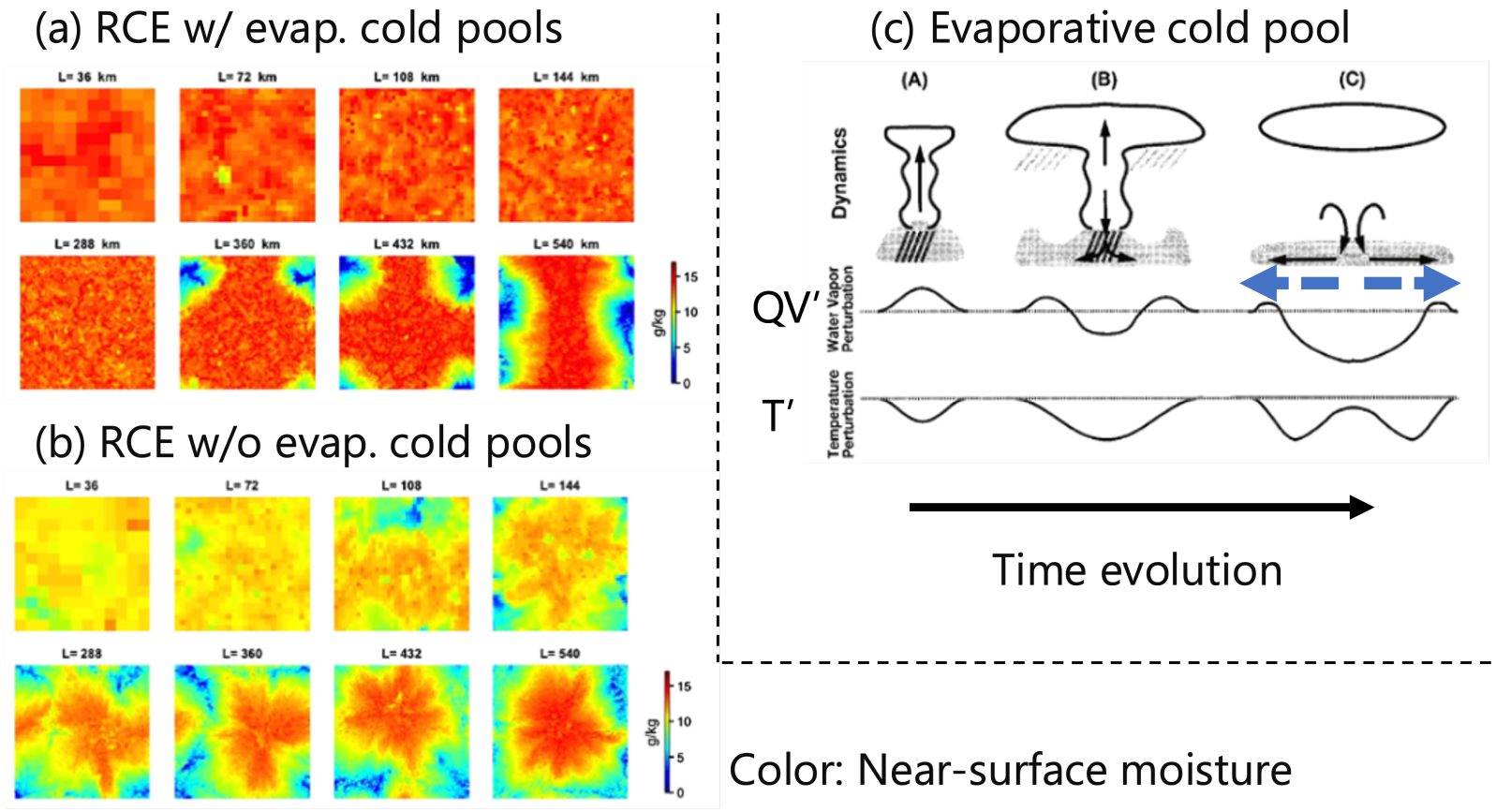

Schematic of the role of evaporatively driven cold pools. (a) Horizontal distribution of near-surface moisture content in RCE experiments with different domain sizes. The domain size increases in calendar order. After Jeevanjee and Romps (2013) Fig. 1. (b) Same as (a), but the evaporation process in the microphysics scheme is turned off below 1 km height. After Jeevanjee and Romps (2013) Fig. 2. (c) Schematic of the development of evaporatively driven cold pool. Cloud dynamics and accompanied perturbation of moisture and temperature near the surface. The cold pool as a density current horizontally transports moisture outward from the center of the system (blue dashed arrows). After Tompkins (2001a) Fig. 14.

図2.1: 大気現象の水平スケールとメソスケール

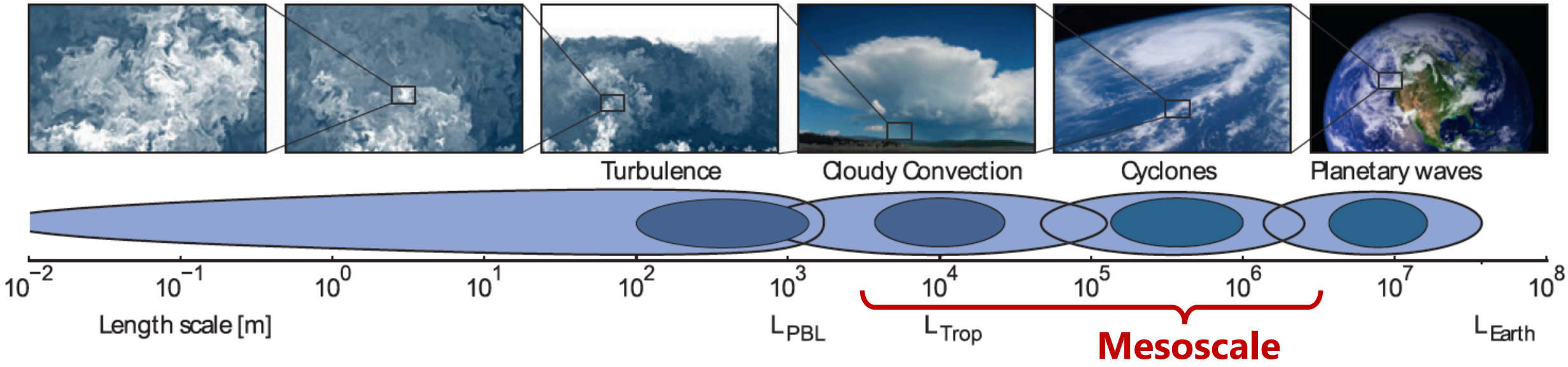

Schematic of the horizontal scale of meteorological phenomena and mesoscale range. LPBL, LTrop, and LEarth, respectively, denote the depth of the planetary boundary layer, the depth of the troposphere, and the circumference of Earth. After Schalkwijk et al. (2015) Fig. 1.

図2.2: RCE実験の概念図

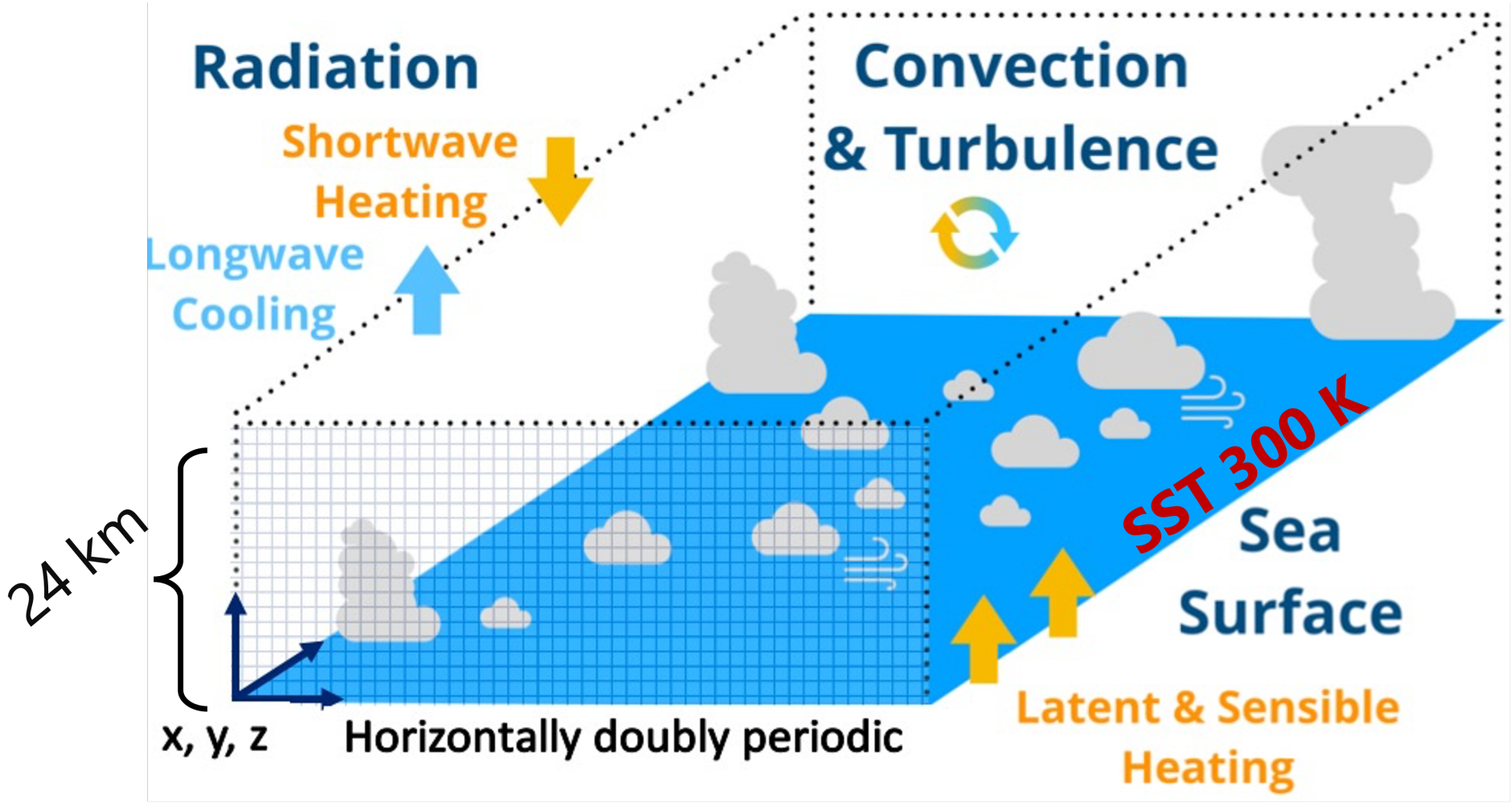

Schematic of RCE experiment

図2.3: 鉛直格子配置

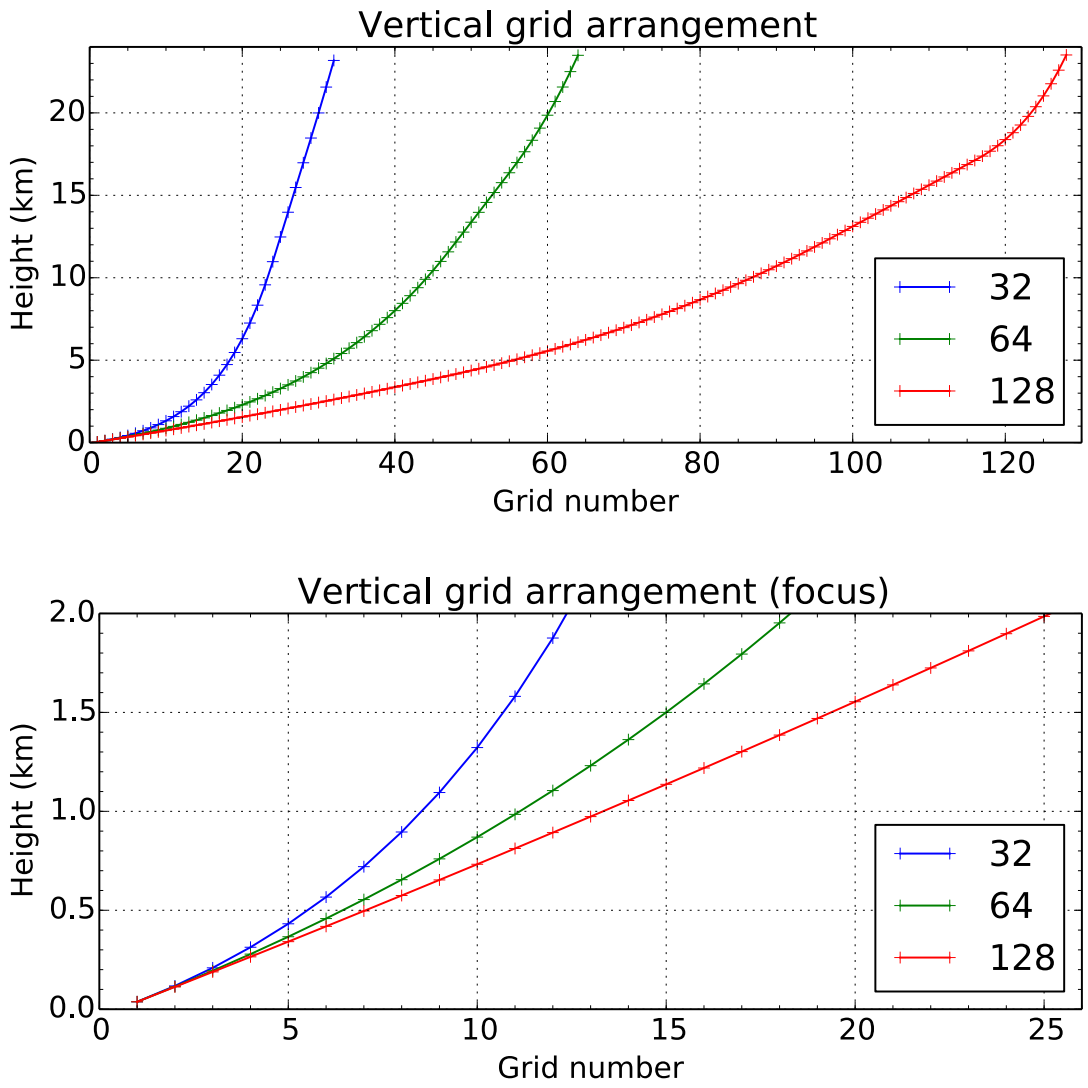

Vertical grid arrangement. The top panel shows three types of arrangement. The 64 layers arrangement is basically used. The 32 and 128 layers arrangements are used for the sensitivity test. The bottom panel focuses on the lower 2 km.

図2.4: コントロールランの熱力学変数鉛直分布

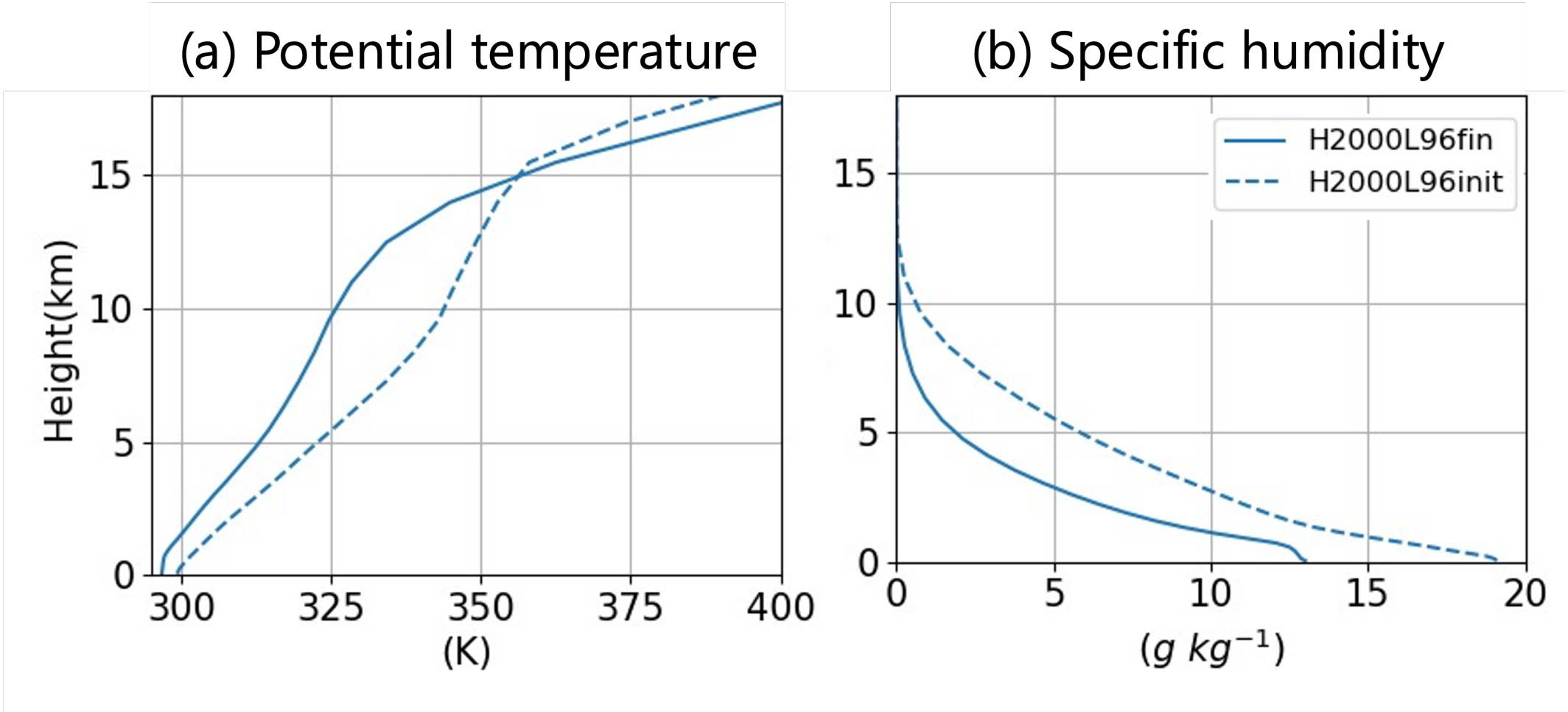

Vertical profile of thermodynamic variables on initial and final days of control experiment. (a) Potential temperature. (b) Specific humidity. The solid and dashed lines indicate final and initial states, respectively. Each value is a horizontal mean.

図2.5: コントロールランの熱力学変数時間発展

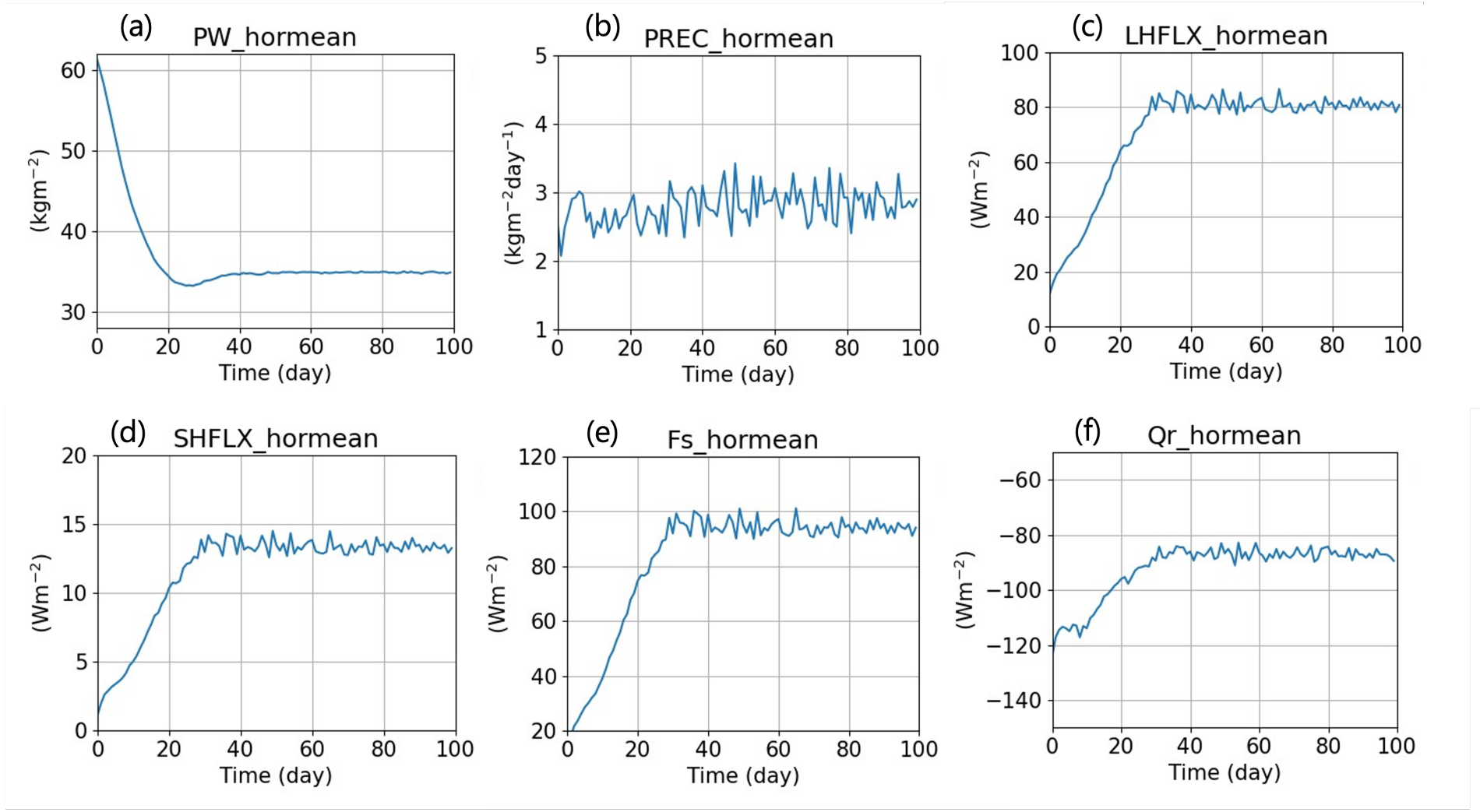

Time evolution of thermodynamic variables of control experiment. (a) Precipitable water. (b) Surface precipitation. (c) Surface latent heat flux. (d) Surface sensible heat flux. (e) Surface total heat flux (c+d). (f) Column net radiative flux convergence. Each value is a horizontal mean.

表2.1: 実験一覧

H (m)	L (km)	Integ. Duration (day)	Δt (s)
500	960	13	2
-	560	40	-
-	384	40	-
-	192	50	-
-	96	50	-
1000	960	40	3
-	560	40	-
-	384	50	-
-	192	50	-
-	96	50	-
1500	576	40	3
-	480	50	-
-	384	50	-
-	288	50	-
-	216	50	-
1750	672	40	3
-	504	50	-
-	378	50	-
-	336	50	-
-	252	50	-
1875	540	50	3
-	360	50	-
-	270	50	-
2000	960	40	6
-	384	50	-
-	288	50	-
-	240	50	-
-	192	50	-
-	96	50	-
3000	288	50	6
-	192	50	-
-	144	50	-
-	96	50	-
4000	384	50	12
-	192	50	-
-	144	50	-
-	96	50	-

Horizontal grid spacing, horizontal domain size, integration duration, and time step interval.

図3.1: 可降水量水平分布の格子幅–領域幅依存性

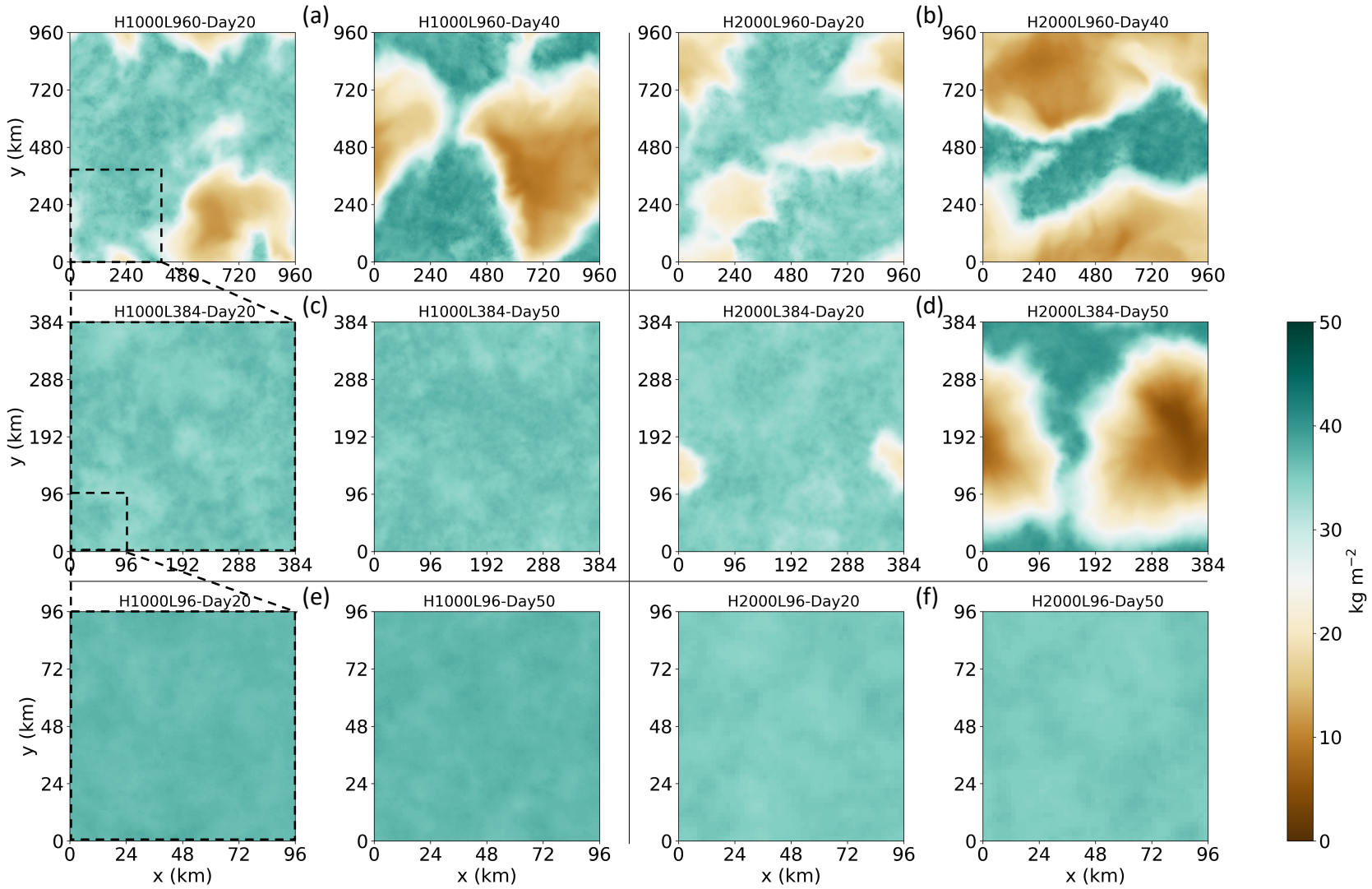

Horizontal distribution of precipitable water in experiments with different horizontal grid spacings and domain sizes. On Day 20 and on the last day of each experiment. (a) H1000L960, (b) H2000L960,(c) H1000L384, (d) H2000L384, (e) H1000L96, and (f) H2000L96. Dashed squares are drawn for size comparison. After Yanase et al. (2020, Fig. 1), licensed under CC BY 4.0.

図3.2: 乾燥パッチ面積率時間発展とRCEレジーム

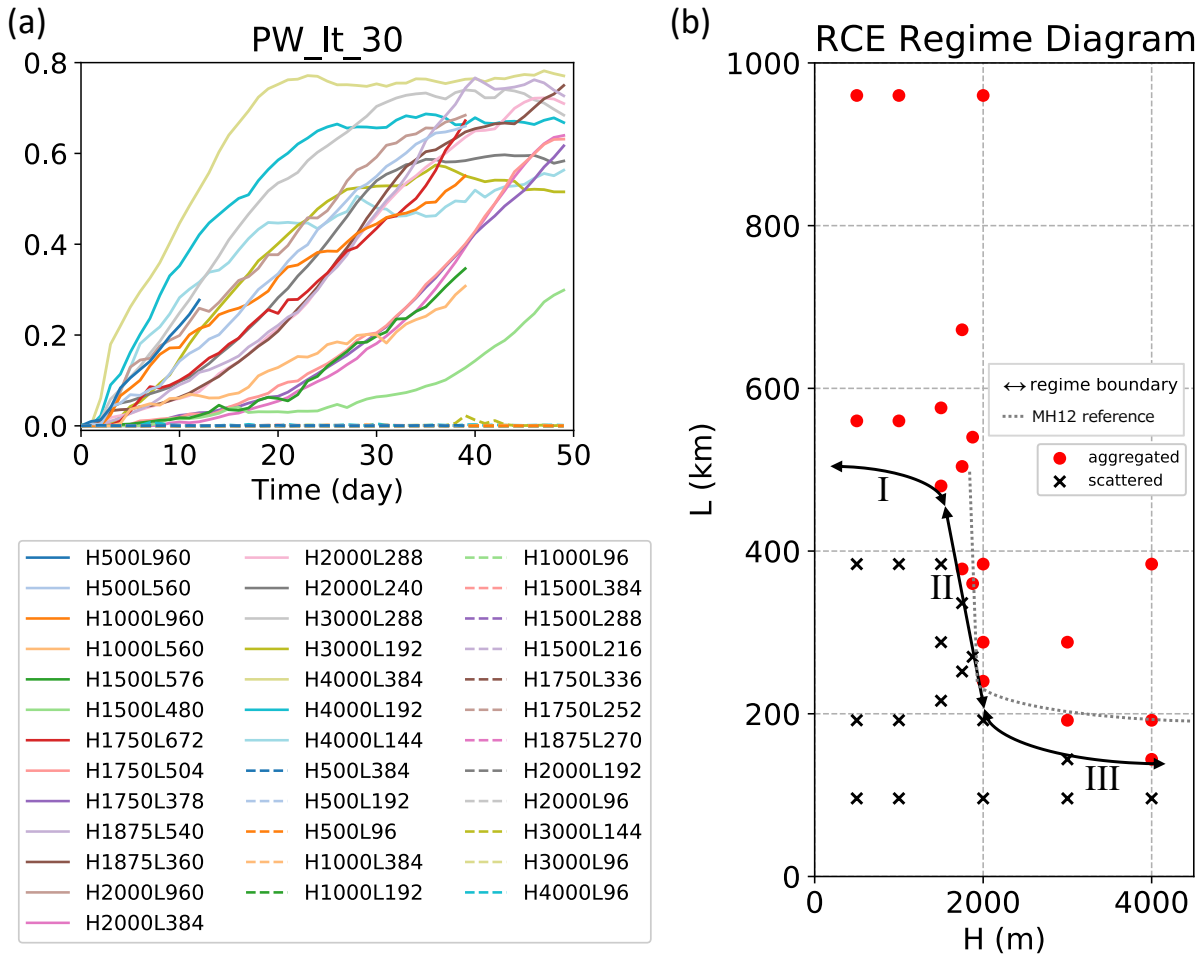

(a) Time evolution of dry patch fraction as a metric of CSA onset. The dry patch is defined as region where precipitable water is less than 30 kg m−2. Solid lines are aggregated cases, where dry patch fraction increases with time. Dashed lines are scattered cases, where dry patch fraction remains near-zero. (b) RCE regime diagram in resolution–domain size parameter space. Red circles are aggregated cases. Black crosses are scattered cases. The regime boundary line is drawn by hand, and it is separated into the lines I, II, and III, for convenience (see the main text). The regime boundary line based on Muller and Held (2012, Fig. 6a) is also drawn as a reference. After Yanase et al. (2020, Fig. 2), licensed under CC BY 4.0.

図3.3: 全実験の可降水量水平分布

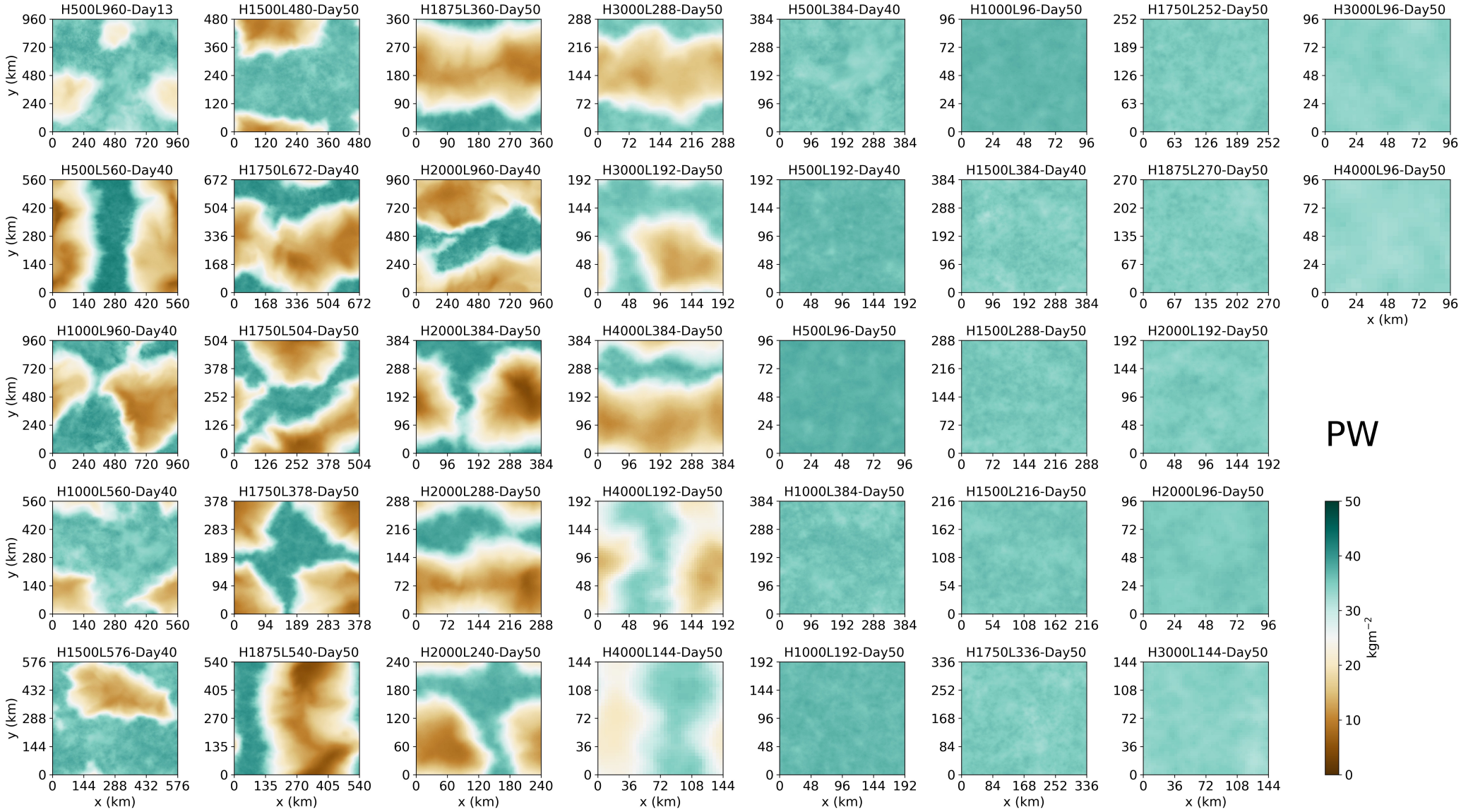

Horizontal distribution of precipitable water in all experiments. On the last day of each experiment. After Yanase et al. (2020, Fig. S1), licensed under CC BY 4.0.

図3.4: 可降水量四分位範囲の時間発展

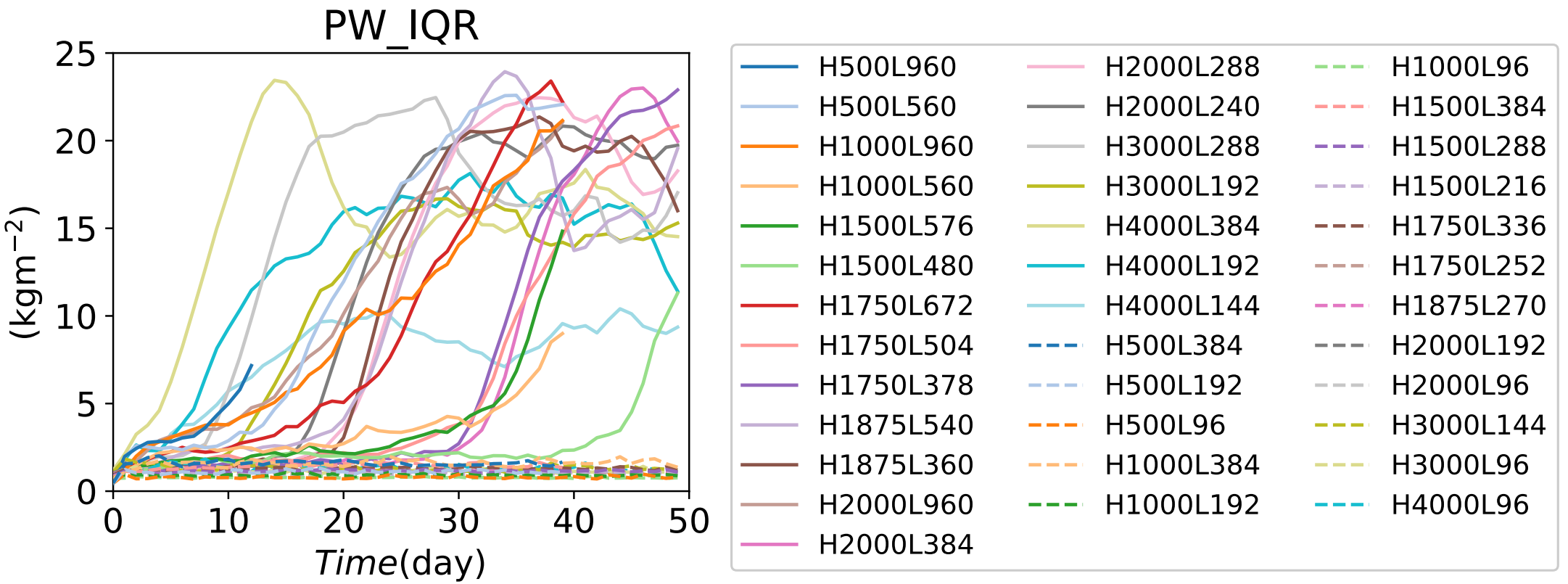

Time evolution of interquartile range of precipitable water in all experiments. After Yanase et al. (2020, Fig. S2), licensed under CC BY 4.0.

図3.5: 可降水量標準偏差の時間発展

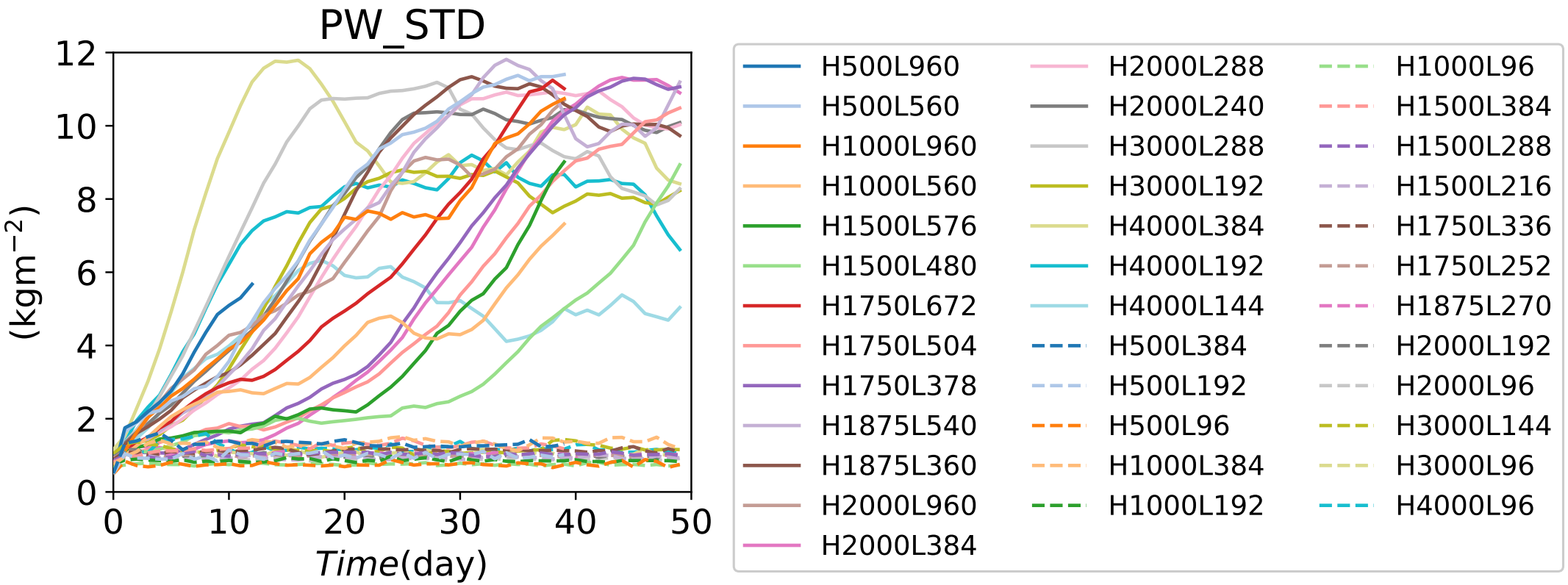

Time evolution of standard deviation of precipitable water in all experiments. After Yanase et al. (2020, Fig. S3), licensed under CC BY 4.0.

図3.6: 水蒸気–高度空間における水蒸気輸送

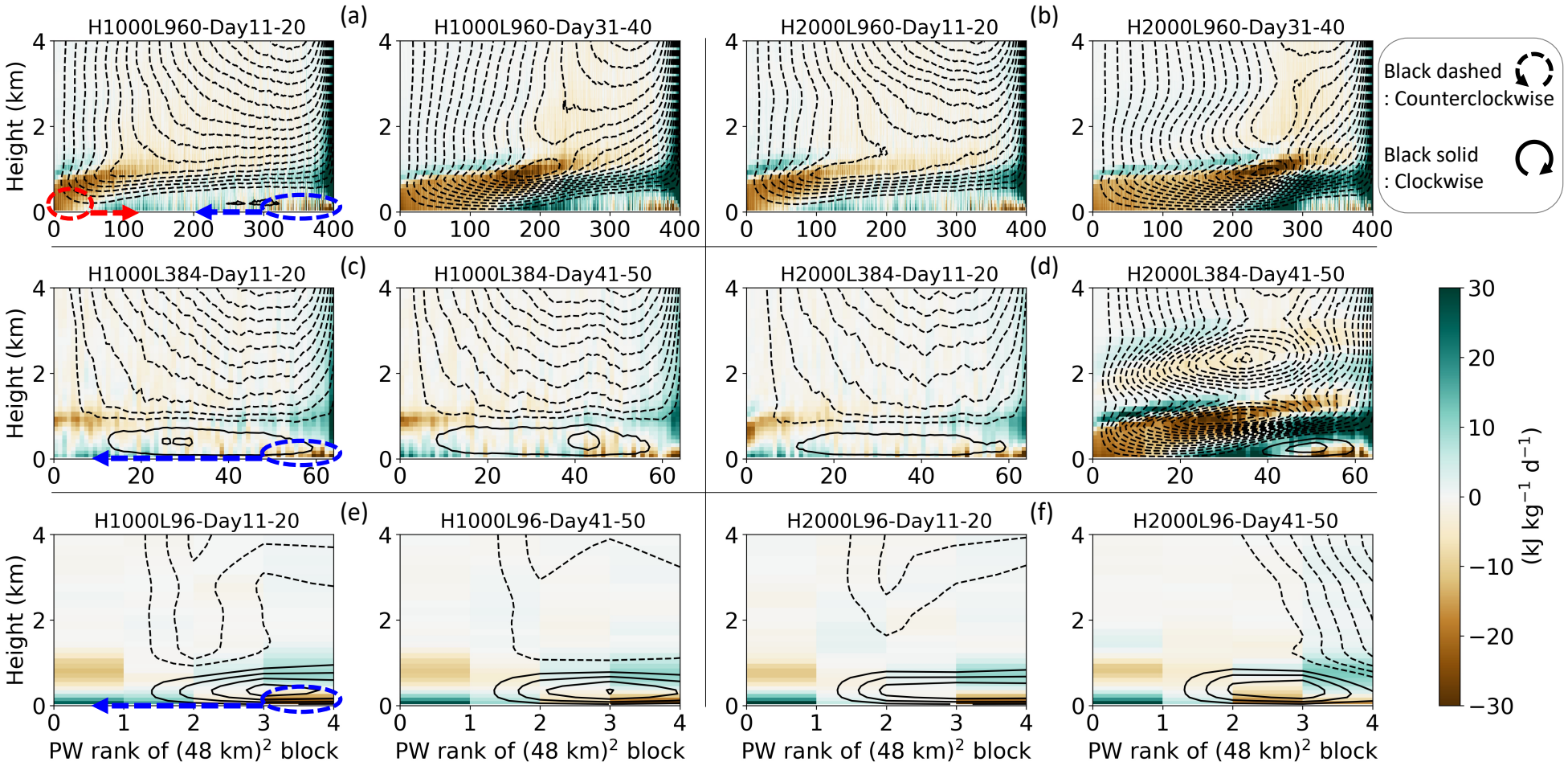

Circulation and moisture transport in moisture–height space. The contour is the effective stream function of Bretherton et al. (2005). The solid lines are positive values and the dashed lines negative; the former indicates counterclockwise circulation and the latter clockwise. The line interval is 0.01 kg m−2 s−1 for L384 and is varied to be proportional to the horizontal area of the computational domain for other cases. The shade is the horizontal flux convergence of water vapor. The experiments and times of panels are the same as Fig. 3.1 except for the average period is 10-day. After Yanase et al. (2020, Fig. 3), licensed under CC BY 4.0.

図3.7: 対流要素の水平分布と下降流域の関係

Convective core

Convection-free
continuous subsidence region

Subsidence size

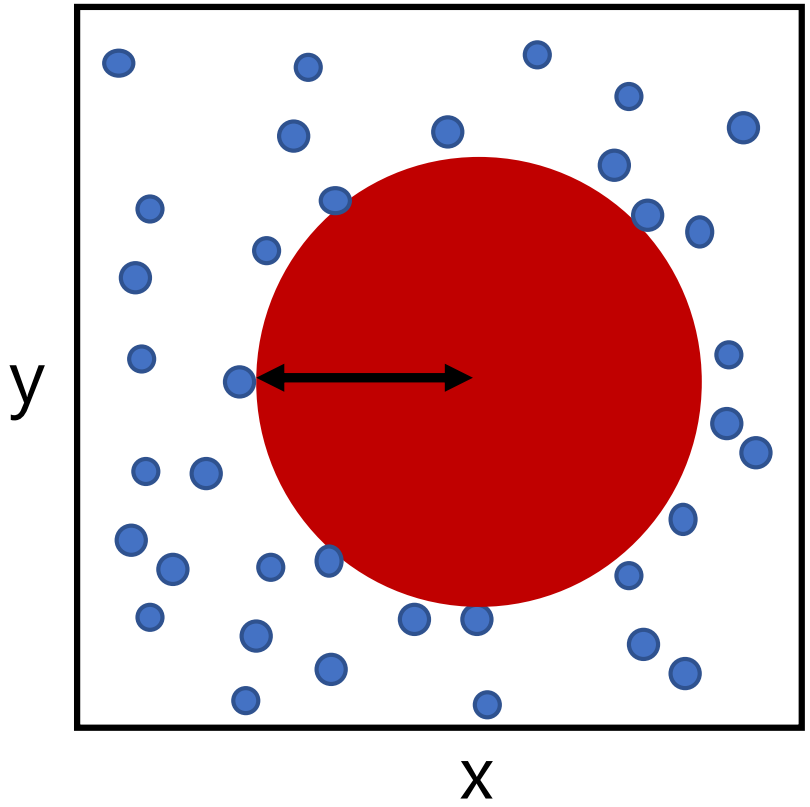

Schematic of horizontal distribution of convective elements and subsidence region

図3.8: 散在・集合レジームの概念図

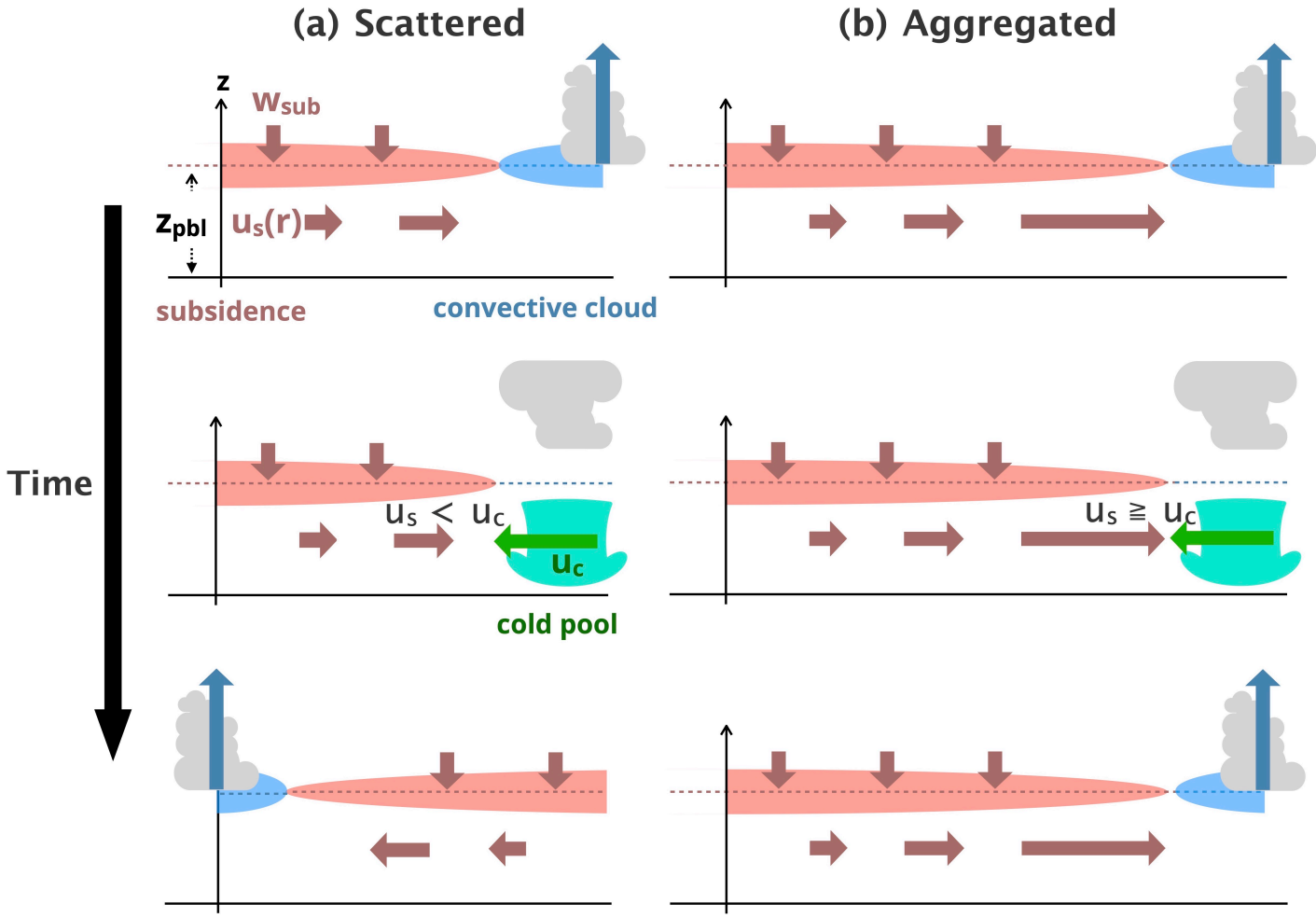

Schematic of scattered and aggregated regimes. The velocity scale of radiatively driven circulation us is a function of horizontal scale of subsidence r, along with the planetaly boundary layer depth zpbl and the subsidence velocity at the top of the layer wsub. The velocity scale of evaporatively driven circulation uc competes us at the end of lifecycle of convective cloud, and the competition determines where the convective cloud in the next generation occurs. The scattered regimes is preferred when uc overwhelms us (a), and the aggregated regimes is preferred when us overwhelms uc (b). After Yanase et al. (2020, Fig. 4), licensed under CC BY 4.0.

図3.9: 水蒸気–高度空間における放射冷却と雲域

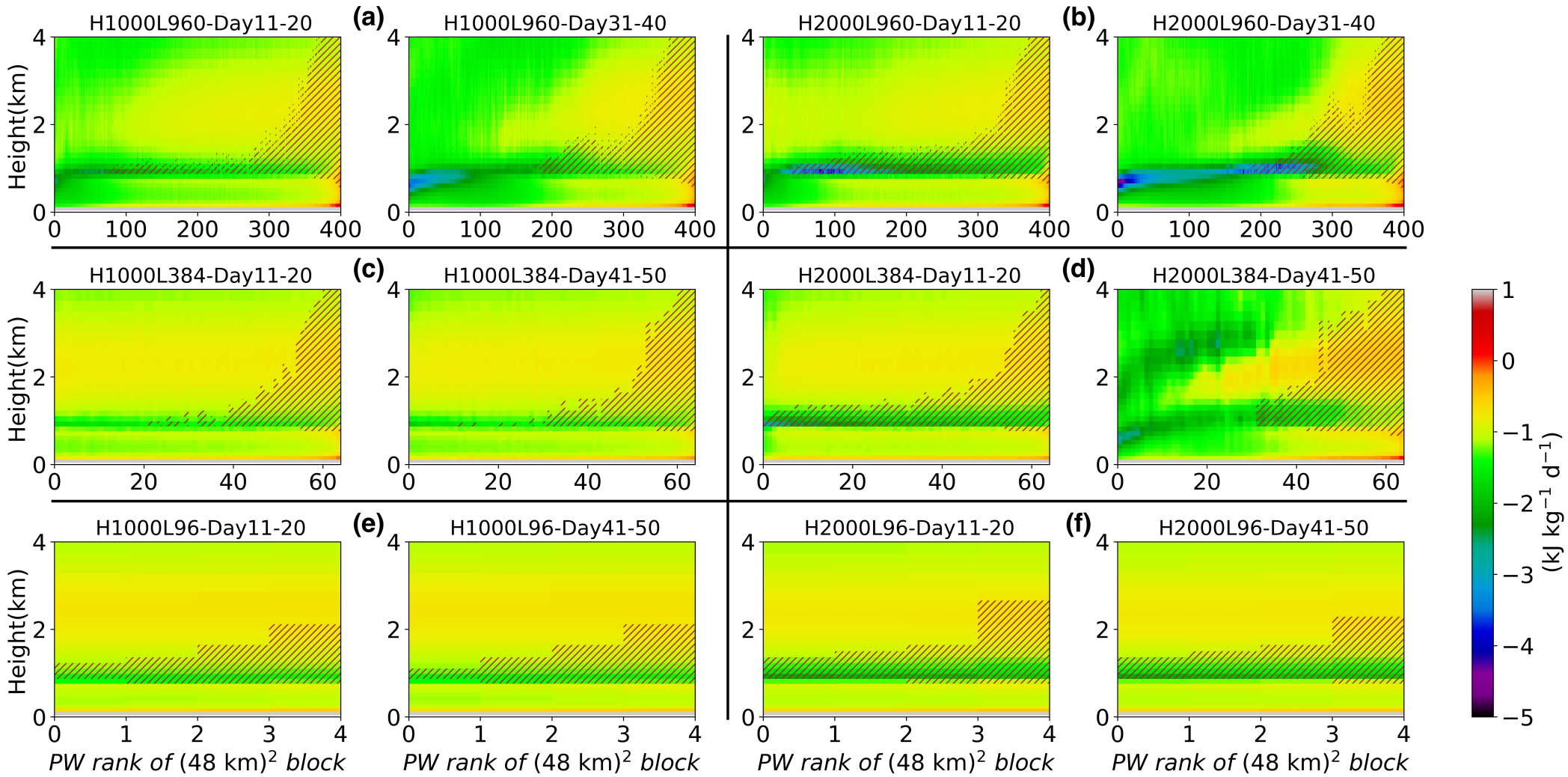

Radiative heating and cloud cover in PW rank–height space. The shade is radiative heating rate. The hatch is the cloud area defined as the place where the mass concentration of cloud water is larger than 5 Å~ 10−6 kg kg−1. The shown cases are same as Fig. 3.6. After Yanase et al. (2020, Fig. S4), licensed under CC BY 4.0.

図3.10: 鉛直層数半減/倍増実験における可降水量

- 鉛直層数を倍増させたら, CSA発生は変わるか? (e.g., 水平・鉛直高解像度でも起きるか?)
  - 鉛直層数32(半減), 128(倍増)実験も要となるパラメータ(H, L)に対しては行った.
  - 例えば, H1000L960の鉛直層数32(半減), 128(倍増)実験においてもCSA発生を確認した.

(a) H1000L960,
32 vertical layers, Day40

(b) H1000L960,
128 vertical layers, Day30

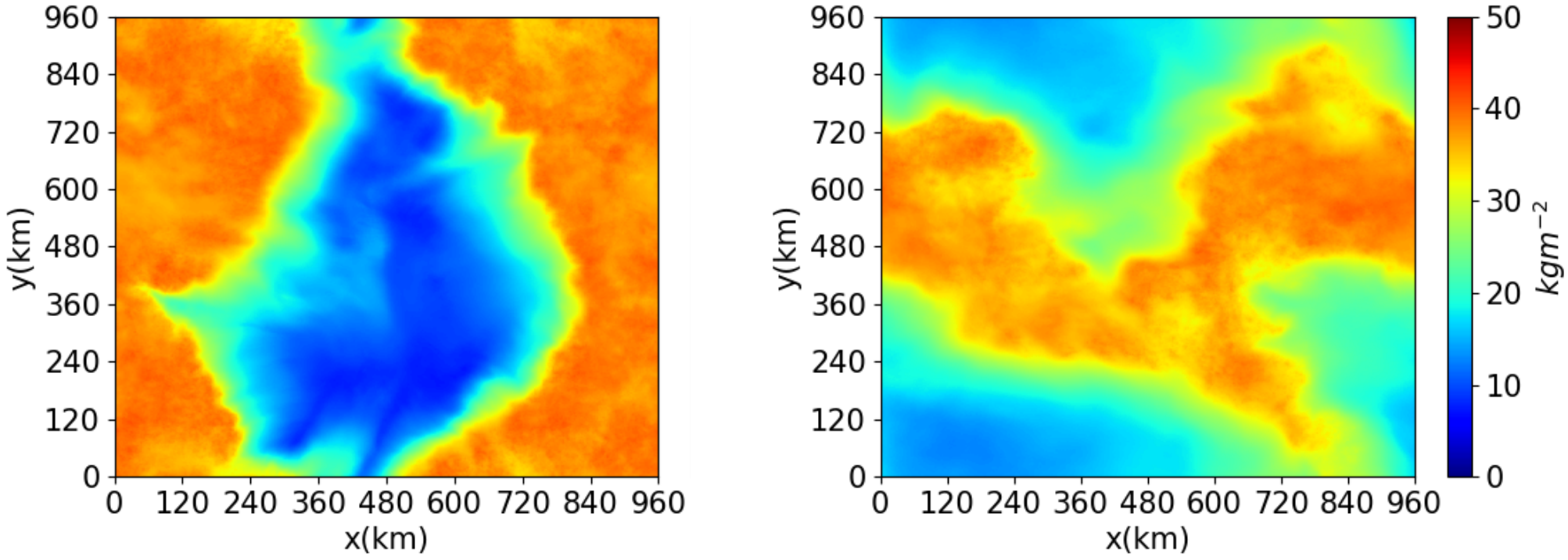

Horizontal distribution of precipitable water in different number of vertical layer experiments. (a) H1000L960 experiment with 32 vertical layers and (b) H1000L960 experiment with 128 vertical layers.

図3.11: MYNN使用実験における可降水量

□境界層スキーム使用するとCSA発生は変わるか?

- 境界層スキーム(MYNN)使用すると, H4000L384でCSA発生しなくなるが, より広領域では発生.

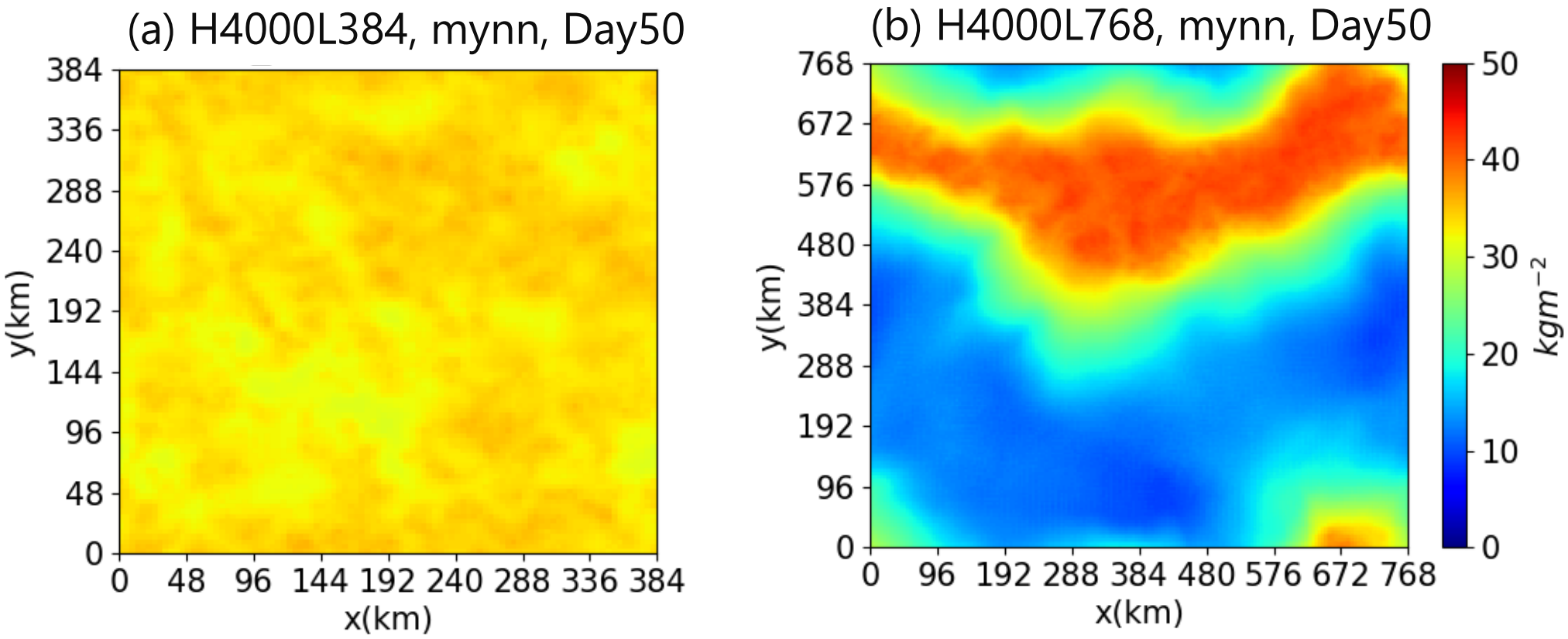

Horizontal distribution of precipitable water in sensitivity experiments using MYNN boundary layer turbulence scheme. (a) H4000L384 and (b) H4000L768.

図3.12: 放射冷却と雲域のSGS乱流依存性

□なぜ境界層スキームを使うと, 狭領域低解像度実験でCSA発生しなくなるのか?

- 境界層スキーム(MYNN)使用すると, Smagorinsky-Lillyのみ(original)と比べ,
  「乾燥域の下層雲減少->放射冷却弱化->臨界長増加」のため, CSA発生しにくくなる.

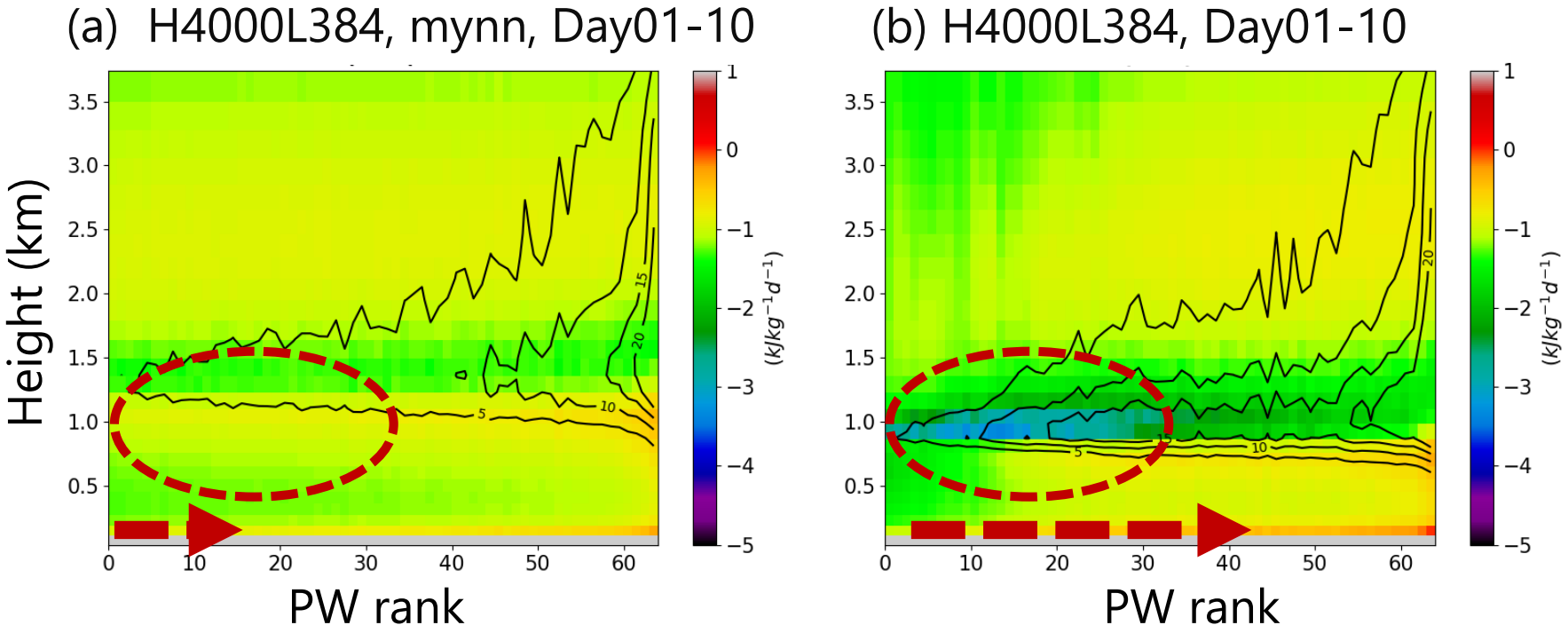

Radiative heating and cloud cover in PW rank–height space in different SGS turbulence scheme experiments. As in Fig. 3.9, but for (a) H4000L384 with MYNN and (b) H4000L384 without MYNN. Red circles indicate the low-cloud level in the dry regions. Red arrows indicate the radiatively driven divergent flow near the surface.

図4.1: 準3次元流線関数と水蒸気距離の概念図

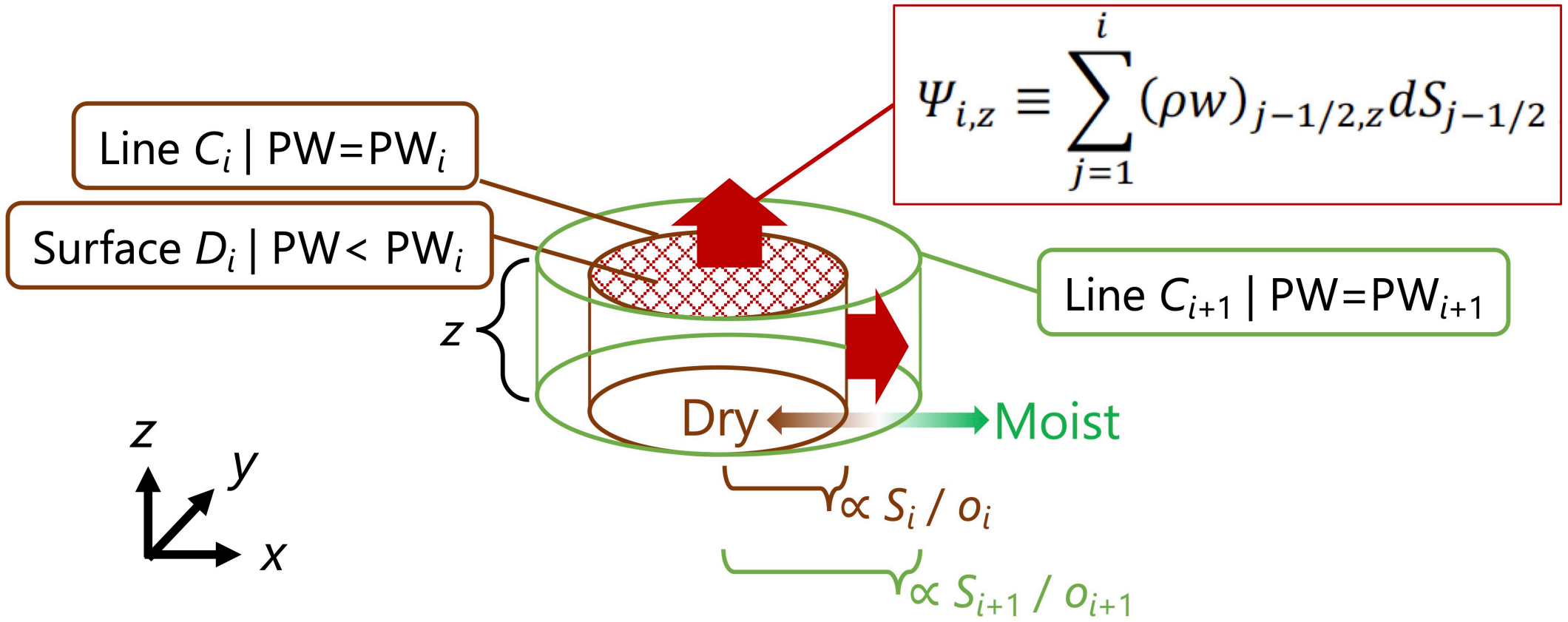

Schematic of the quasi-three-dimensional stream function and moisture distance. The horizontal domain is divided into dry and moist regions by isolines of precipitable water (lines Ci and Ci+1). The surface Di denotes the region enclosed by line Ci. The quasi-three-dimensional stream function Ψi,z denotes the vertical mass flux integrated over surface Di at height z. The area-to-perimeter ratio Si/oi, which we call moisture distance, is a length scale relevant to the geometrical shape of the region Si.

図4.2: 離散的な2次元空間における周囲長

1. 二次元離散データをある閾値で二値化
2. エッジ検出 & 縁辺グリッド検出 (※エッジを少なくとも1つ含むグリッド; エッジは黒白が接する辺.)

- 等値線の長さはエッジ数×水平格子幅
- 等値線を横切る流れはエッジでの水平フラックスから評価

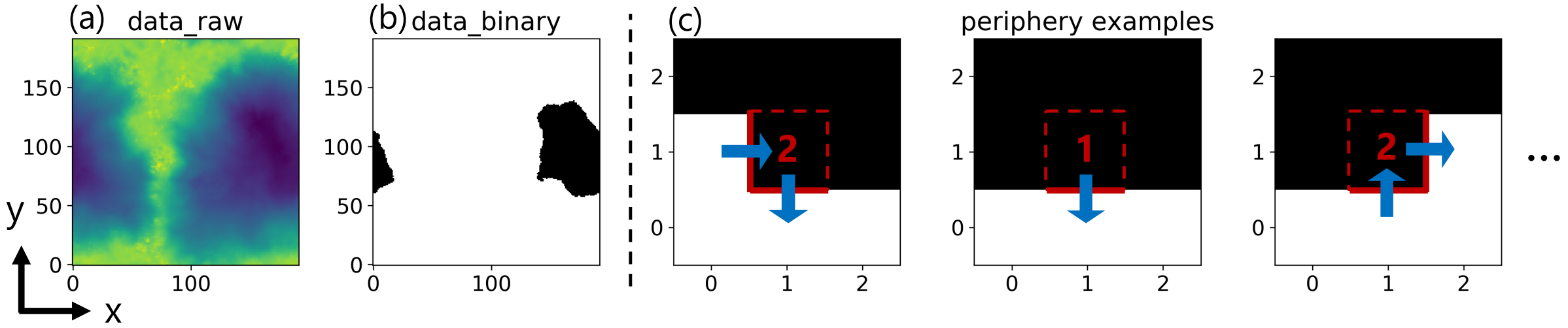

Schematic of a perimeter in a discrete two-dimensional field, especially about how an isoline, its length, and traversing flow are treated. (a) original two-dimensional field. (b) binarized two-dimensional field by a certain threshold value. (c) examples of the grids belonging to the periphery; the solid red line denotes the cell edge belonging to the isoline; the red characters denote the number of cell edges belonging to the isoline for each peripheral grid; the blue arrows denote the traversing flow across the isoline.

図4.3: 準3次元流線関数で見る循環場

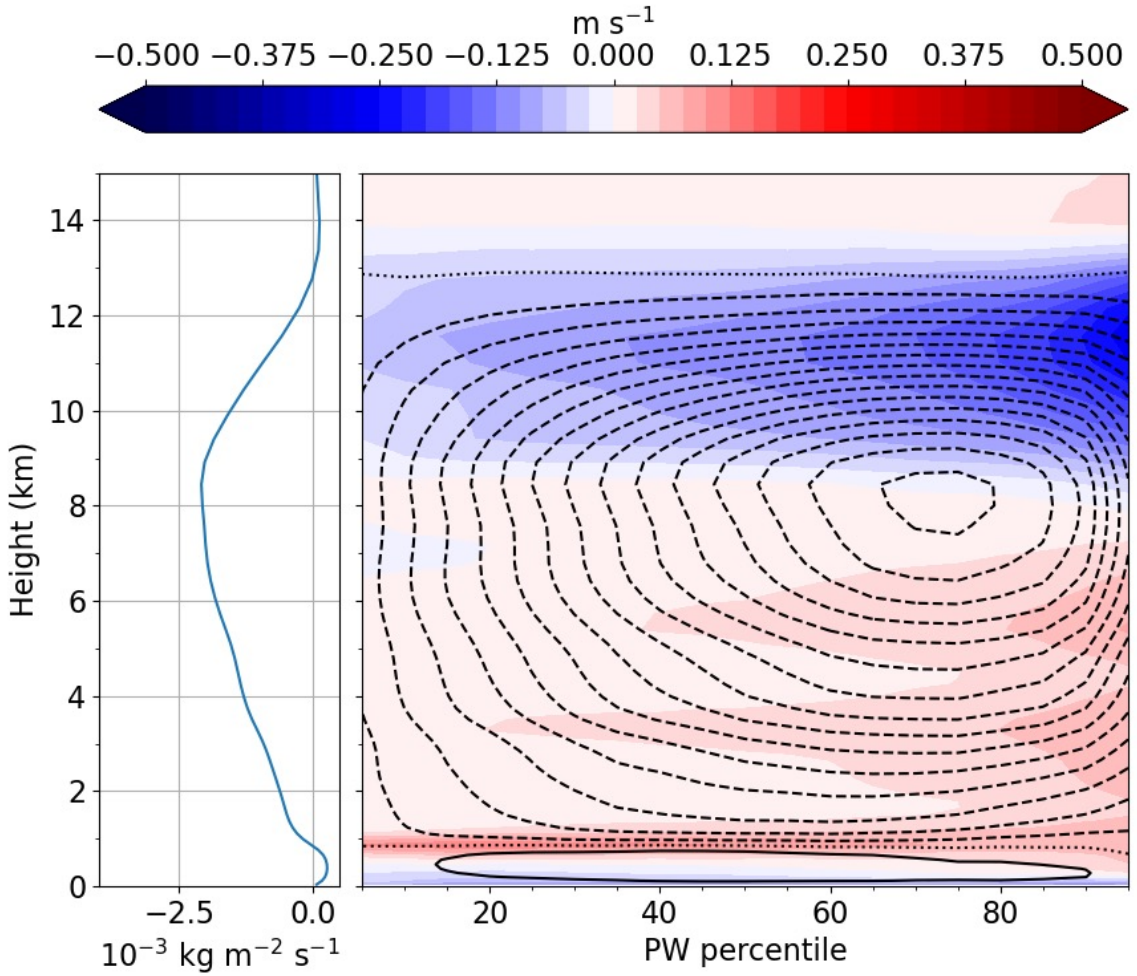

Circulation field quantified by quasi-three-dimensional stream function in moisture–height space for initial 10-day of H1000L384 (scattered case). The contour is normalized quasi-three-dimensional function, Ψi,z/L2; L is the domain size. The solid, dotted, and dashed lines denote positive, zero, and negative values, respectively, with the interval 2 * 10−4 kg m−2 s−1. The shaded denotes the horizontal wind speed traversing the PW isolines, $\tilde{v}$. The vertical profile in the left panel denotes the normalized quasi-three-dimensional function averaged over the horizontal axis.

図4.4: 準3次元流線関数で見る循環場の比較

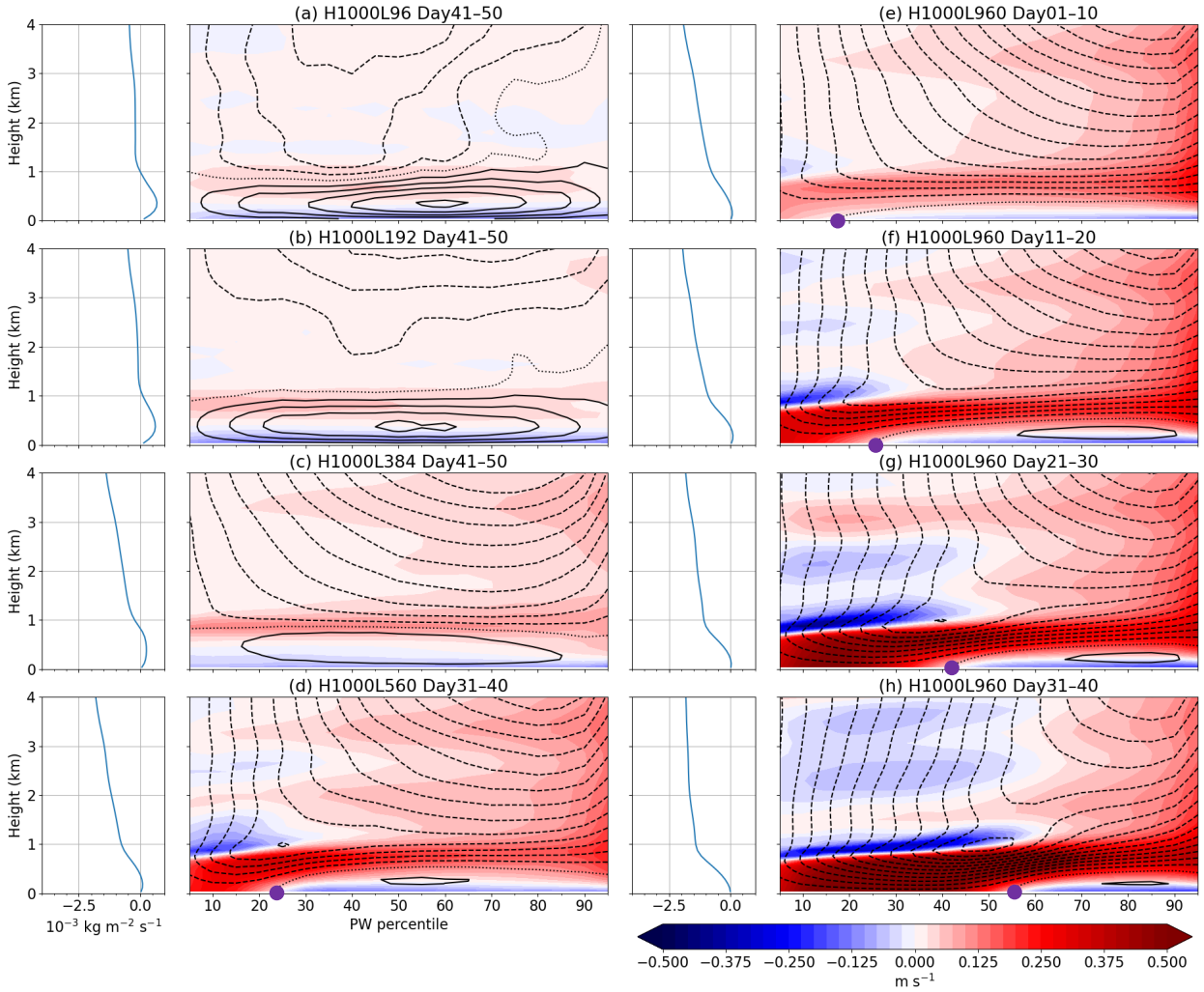

Circulation field quantified by quasi-three-dimensional stream function in moisture–height space for different domain size cases. As in Fig.4.3, but for different cases, different timing, and different vertical range. (a) Day 41–50 of H1000L96, (b) Day 41–50 of H1000L192, (c) Day 41–50 of H1000L384, (d) Day 31–40 of H1000L560, (e) Day 1–10 of H1000L960, (f) Day 11–20 of H1000L960, (g) Day 21–30 of H1000L960, and (h) Day 31–40 of H1000L960. The purple points denote the switching place of the traversing horizontal wind at the surface.

図4.5: 運動学的指標としての境界層平均Q3D-SF

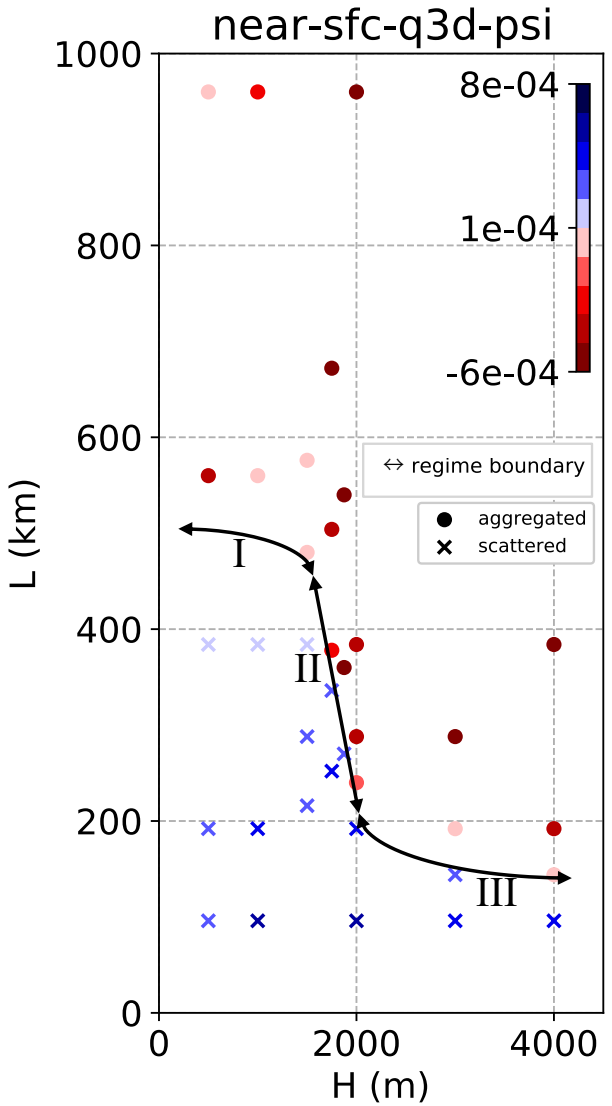

The normalized quasi-three-dimensional stream function averaged in the PBL as a kinematic metric of RCE regime. As in Fig. 3.2b, but the colors of markers are the metric averaged on final 10-day.

図4.6: 水蒸気–高度空間における浮力・蒸発・放射

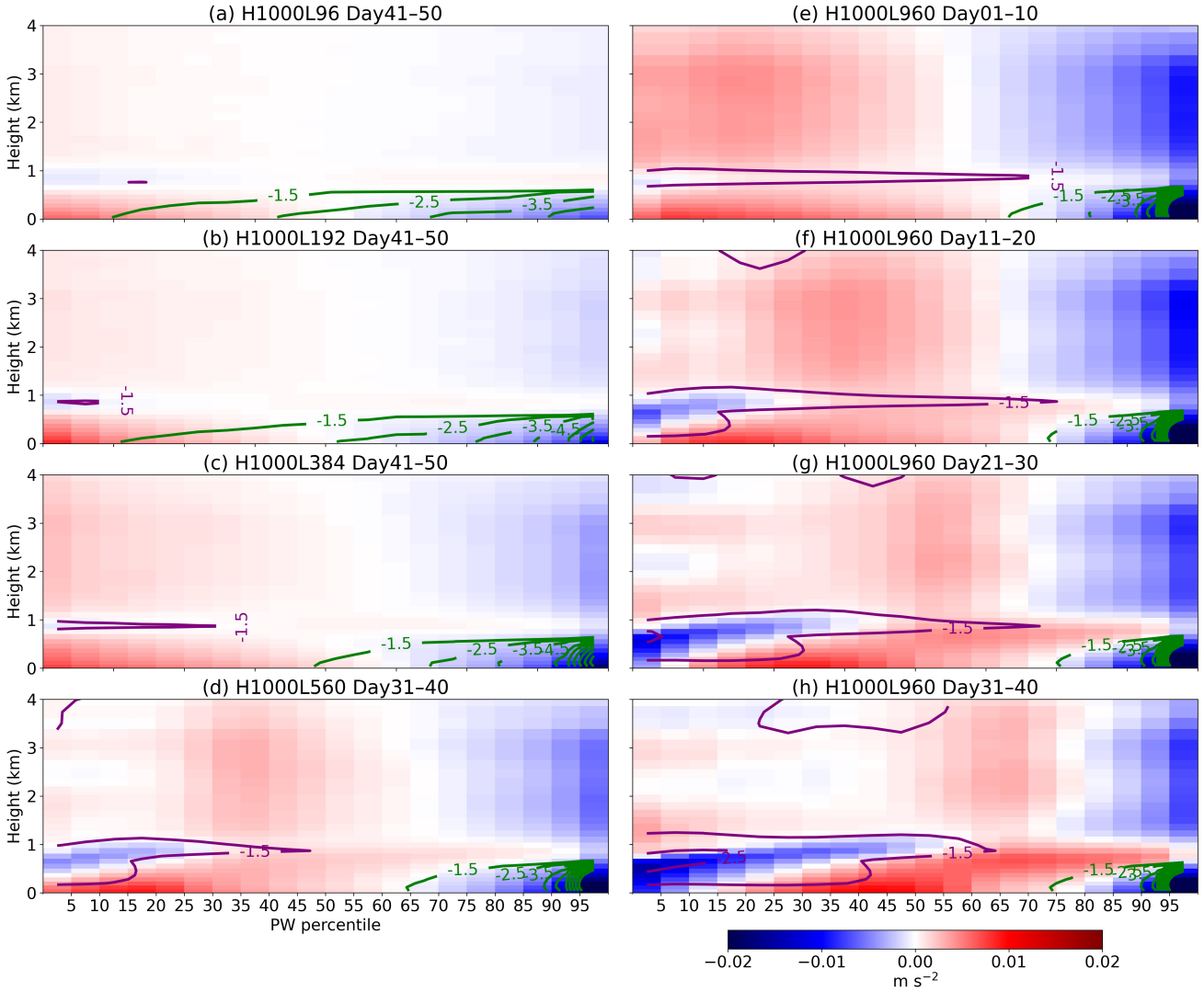

Buoyancy, evaporative cooling, and radiative cooling in moisture–height space. The green (purple) contours show a microphysical (radiative) heating rate (only values not greater than -1.5 kJ kg−1 day−1 with the interval 1.0 kJ kg−1 day−1). Shown cases and times are same as Fig. 4.4.

図4.7: 境界層内のトルク

初期10日は正浮力勾配は支配的ではない

- 渦度方程式

$$\frac{\partial \eta}{\partial t} = \frac{\partial \bar{\rho} B}{\partial \tilde{y}} + \frac{\partial F_z}{\partial \tilde{y}} - \frac{\partial F_{\tilde{y}}}{\partial z}$$

- 正確には運動量の回転の時間変化
- ∇PWを局所座標の $\tilde{y}$ 方向とみなす
- $\tilde{y}$ –z面内の2次元運動と仮定
- Q3D-SFの時間変化と逆符号

ここで

$$\eta \equiv \frac{\partial \bar{\rho} w}{\partial \tilde{y}} - \frac{\partial \bar{\rho} \tilde{v}}{\partial z}$$

$$B \equiv -g \frac{\rho'}{\bar{\rho}}$$

$$F_z \equiv -\frac{\partial \bar{\rho} w \tilde{v}}{\partial \tilde{y}} - \frac{\partial \bar{\rho} w w}{\partial z} + F_{\mathrm{SGS},z}$$

$$F_{\tilde{y}} \equiv -\frac{\partial \bar{\rho} \tilde{v} \tilde{v}}{\partial \tilde{y}} - \frac{\partial \bar{\rho} w \tilde{v}}{\partial z} + F_{\mathrm{SGS},\tilde{y}}.$$

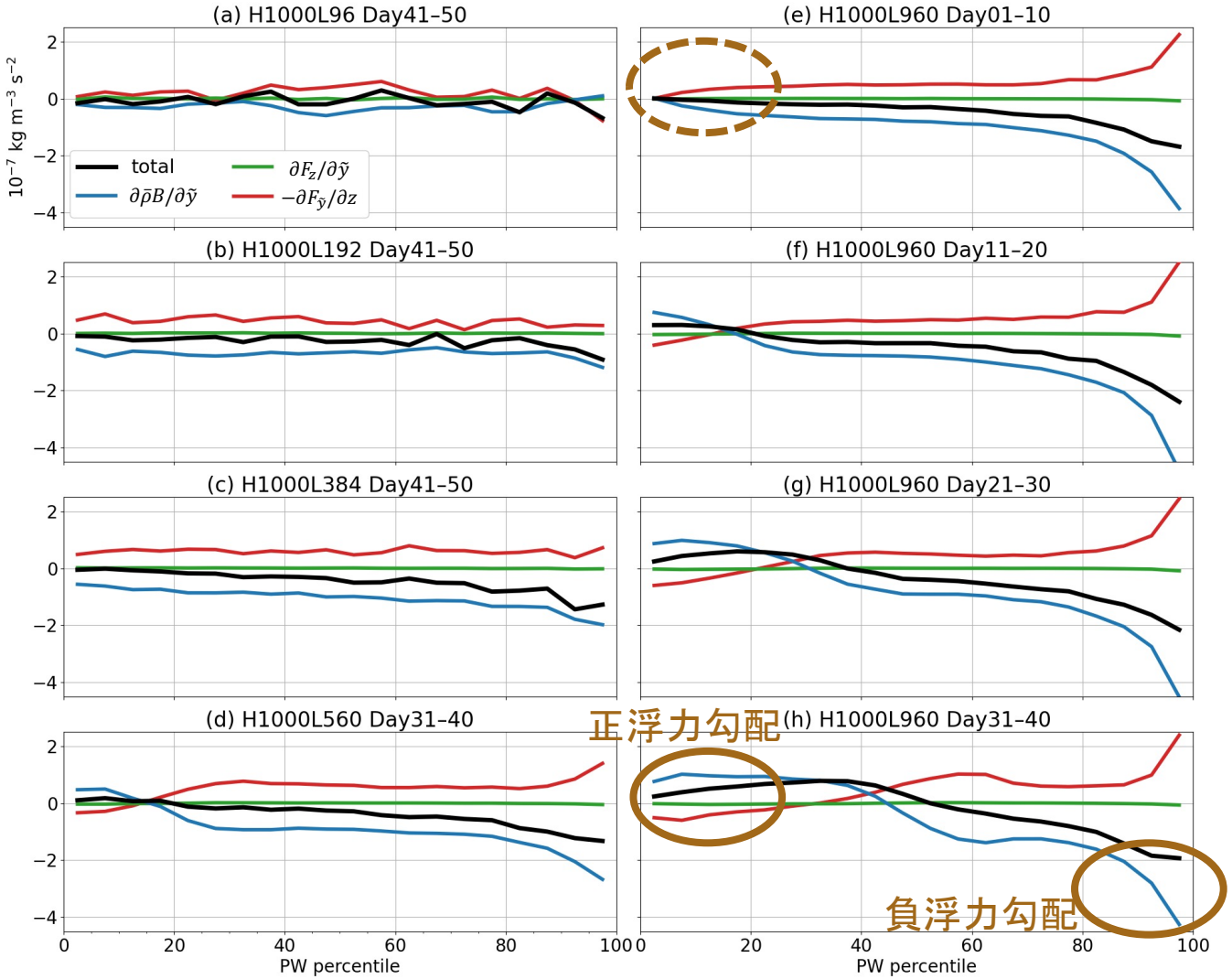

Torque terms for the vorticity in moisture–height space. The tendency terms in Eq. (4.8) of the main text: the total (black), buoyancy gradient (blue), w-acceleration gradient (green), and $\tilde{v}$ -acceleration gradient (red). Each term is the average over planetary boundary layer depth. Shown cases and times are same as Fig. 4.4.

図4.8: 乾燥域における鉛直速度のWTG診断

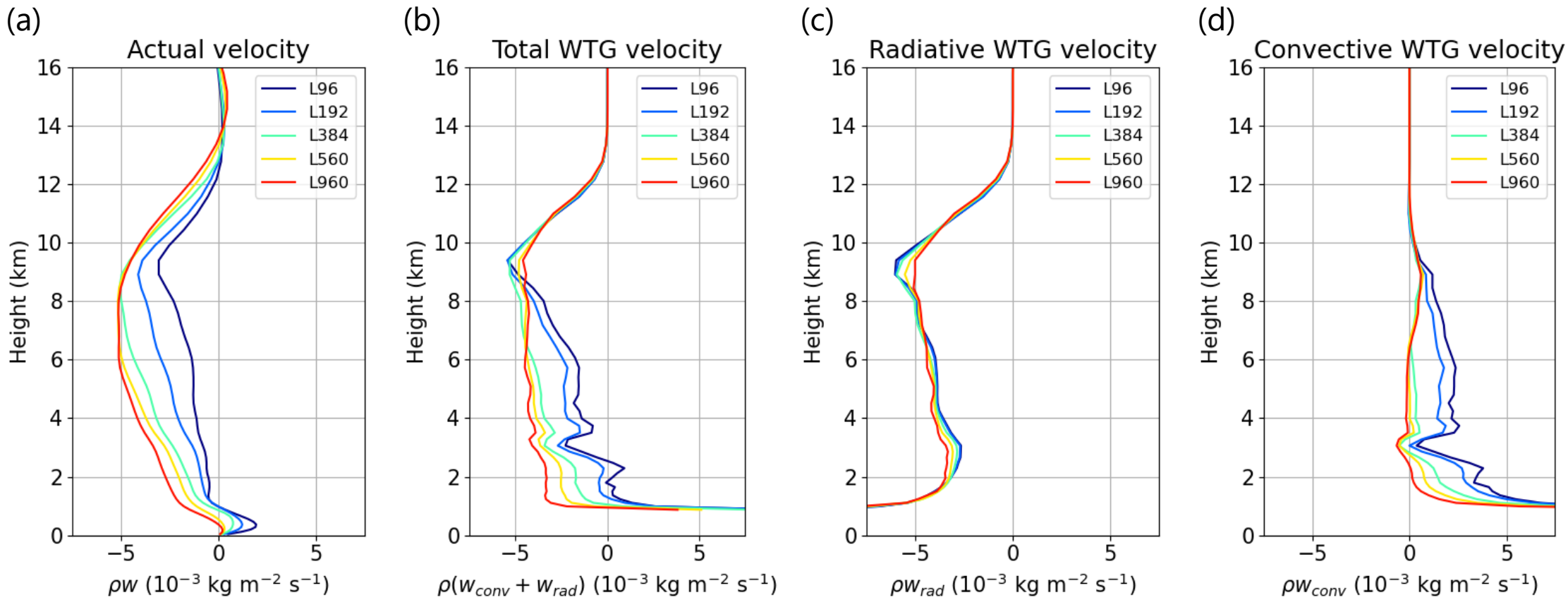

WTG assessment of vertical velocity in the dry region. (a) Actual vertical velocity. (b) WTG vertical velocity diagnosed by the total of radiative heating and convective heating (see Eq. 4.16 of the main text). (c) WTG vertical velocity diagnosed by the radiative heating. (d) WTG vertical velocity diagnosed by the convective heating. Convective heating refers to the total of microphysical heating and vertical eddy-flux convergence of dry static energy. Each profile is the average over the drier half region on the initial 10-day.

図4.9: 鉛直速度の半経験的鉛直モード分解

- 半経験的モード展開 $\rho w = o_1\Omega_1 + o_2\Omega_2 + o_3\Omega_3$

$\Omega_1 \equiv \sin(\pi z/D_{\mathrm{TRP}})$, $\Omega_2 \equiv \sin(2\pi z/D_{\mathrm{TRP}})$, and $\Omega_3 \equiv \sin(\pi z/d)$

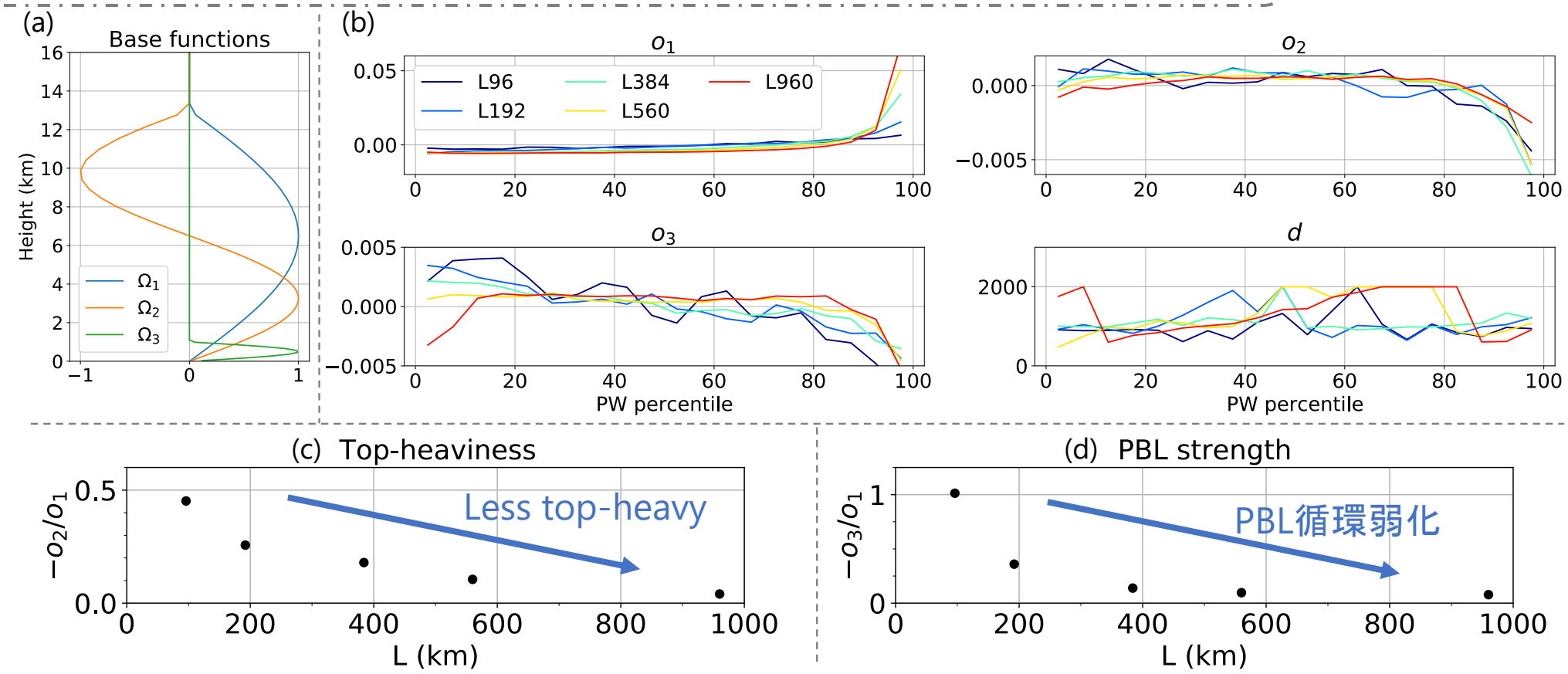

Semi-empirical vertical mode decomposition of vertical velocity profile. (a) The vertical profiles of three base functions (see Eq. 4.15 of the main text). (b) The coefficients derived by least-square fitting for each 5 percentile interval (initial 10-day). (c) Top-heaviness: the ratio of −o2 to o1. (c) PBL circulation strength: the ratio of −o3 to o1.

図4.10: 水蒸気と非断熱加熱の関係

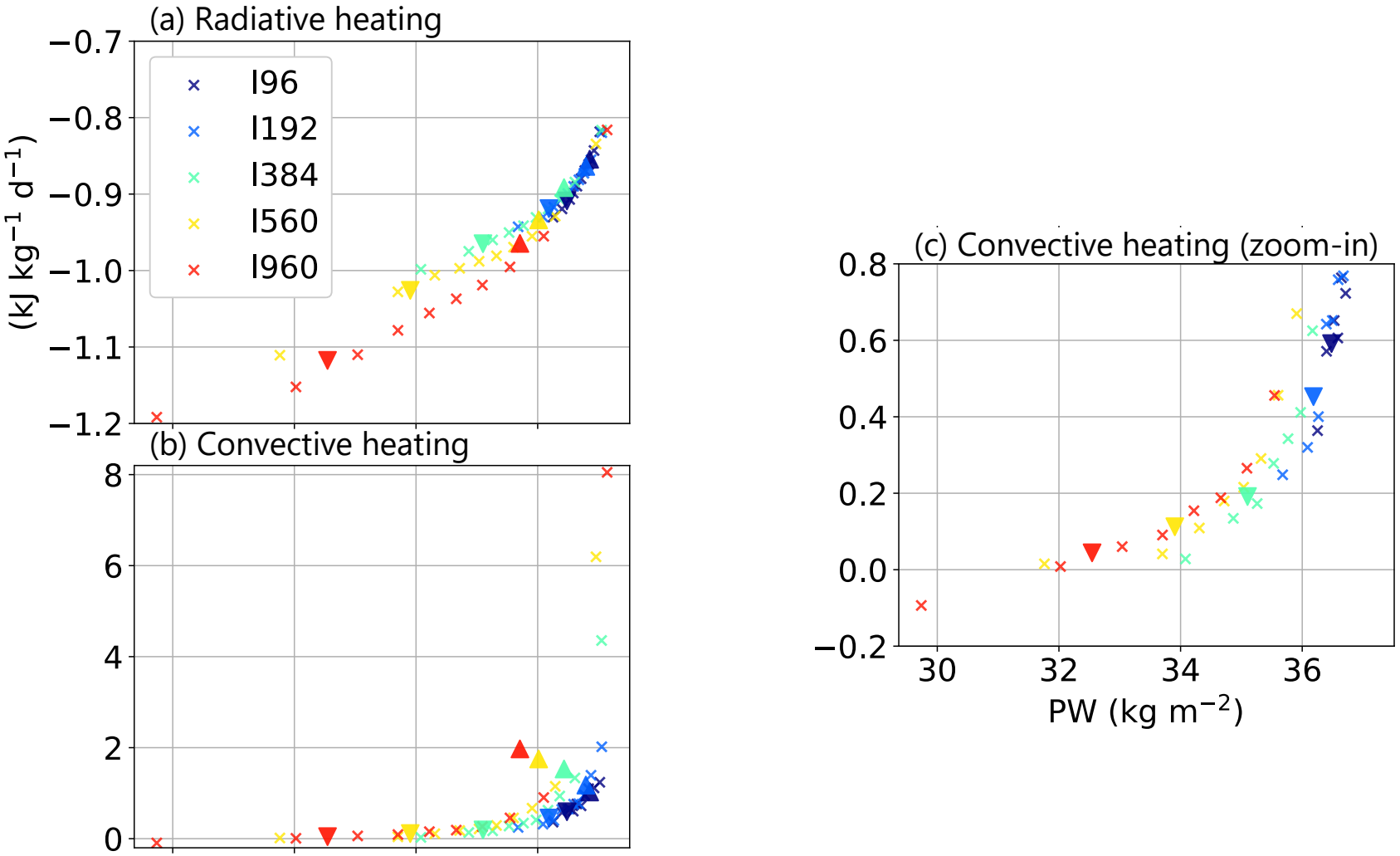

Relationship between diabatic heating and moisture. (a) Radiative heating versus PW. (b) Convective heating versus PW. (c) As (b) but focused on the lower heating range. Each value is the mass-weighted average from ground surface to about 6 km height on initial 10-day. The cross markers are the average over the 10 percentile intervals, and the triangle markers are the average over 50 percentile intervals.

図4.11: 比湿水平パワースペクトルの波長–高度分布

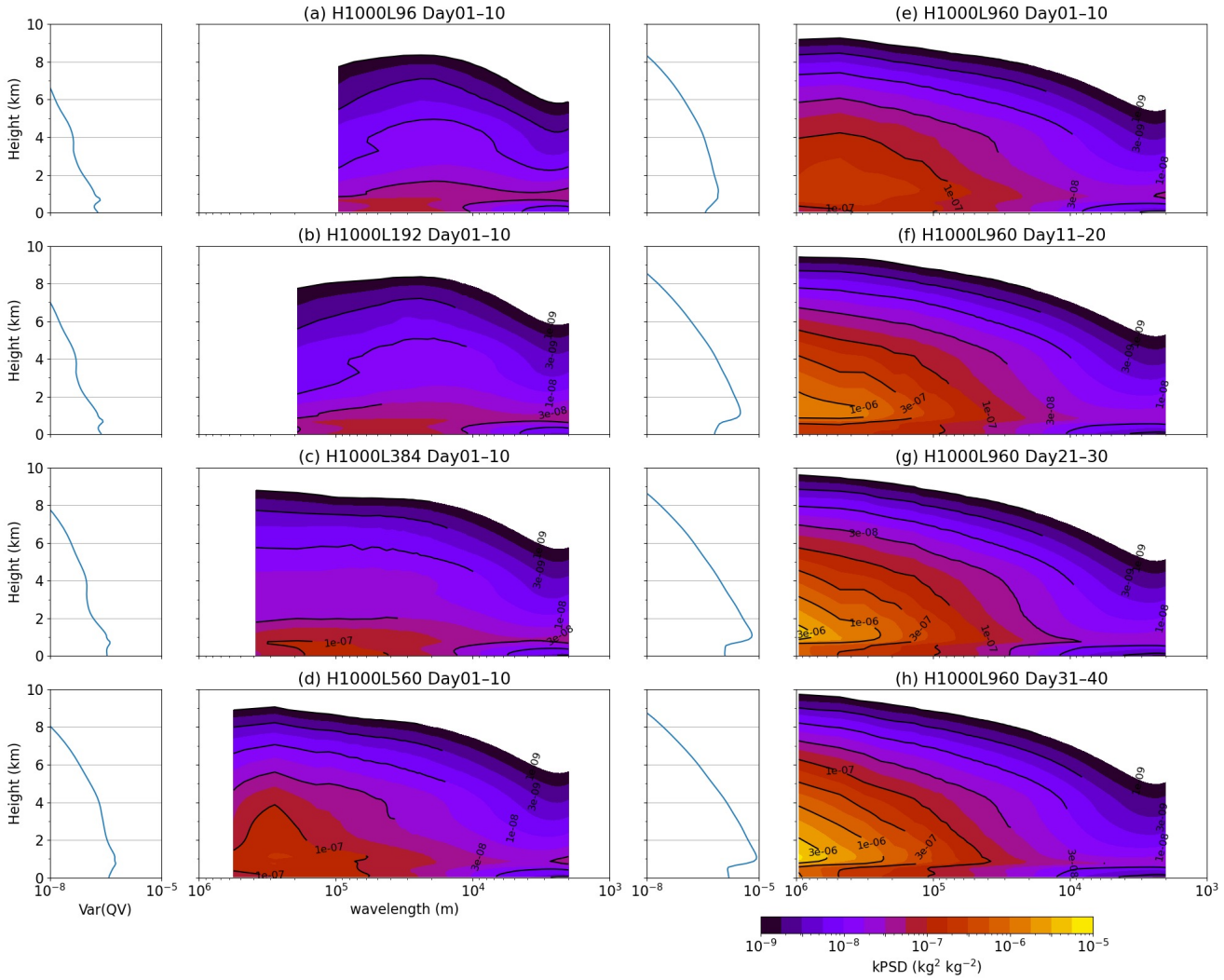

Horizontal power spectral density of specific humidity in the wavelength–height space. The vertical profile in the left of each panel is the horizontal variance of specific humidity. (a) H1000L96, (b) H1000L192, (c) H1000L384, and (d) H1000L560, and consecutive 10-days for (e)–(h) H1000L960. The power spectral density is multiplied by horizontal wavenumber, k. The value is averaged on the initial 10-day.

図4.12: 高度2.5km比湿 水平パワースペクトル

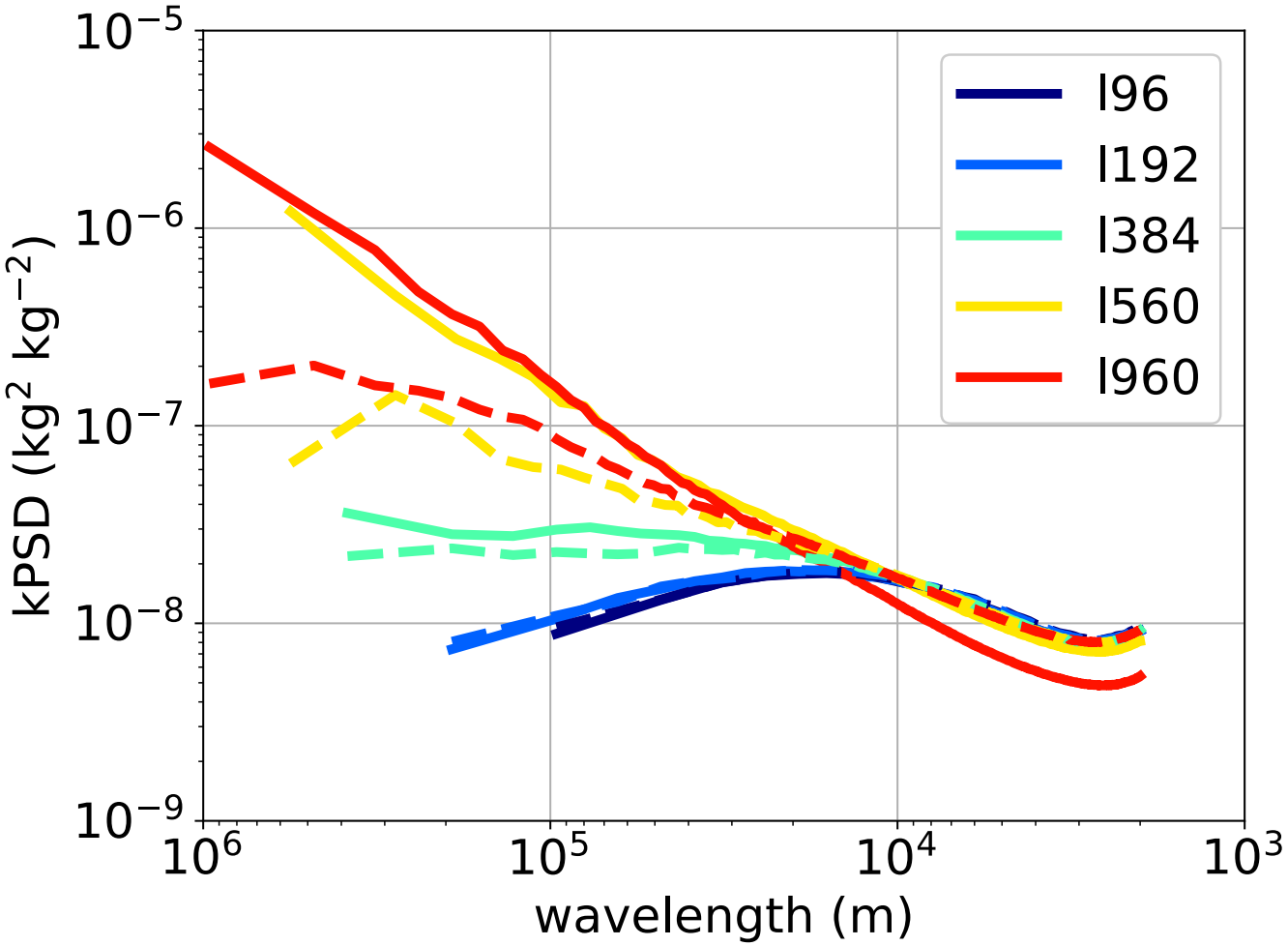

Horizontal power spectral density of specific humidity at 2.5 km height. The solid (dashed) lines are for the final (initial) 10-day.

図4.13: 水蒸気距離

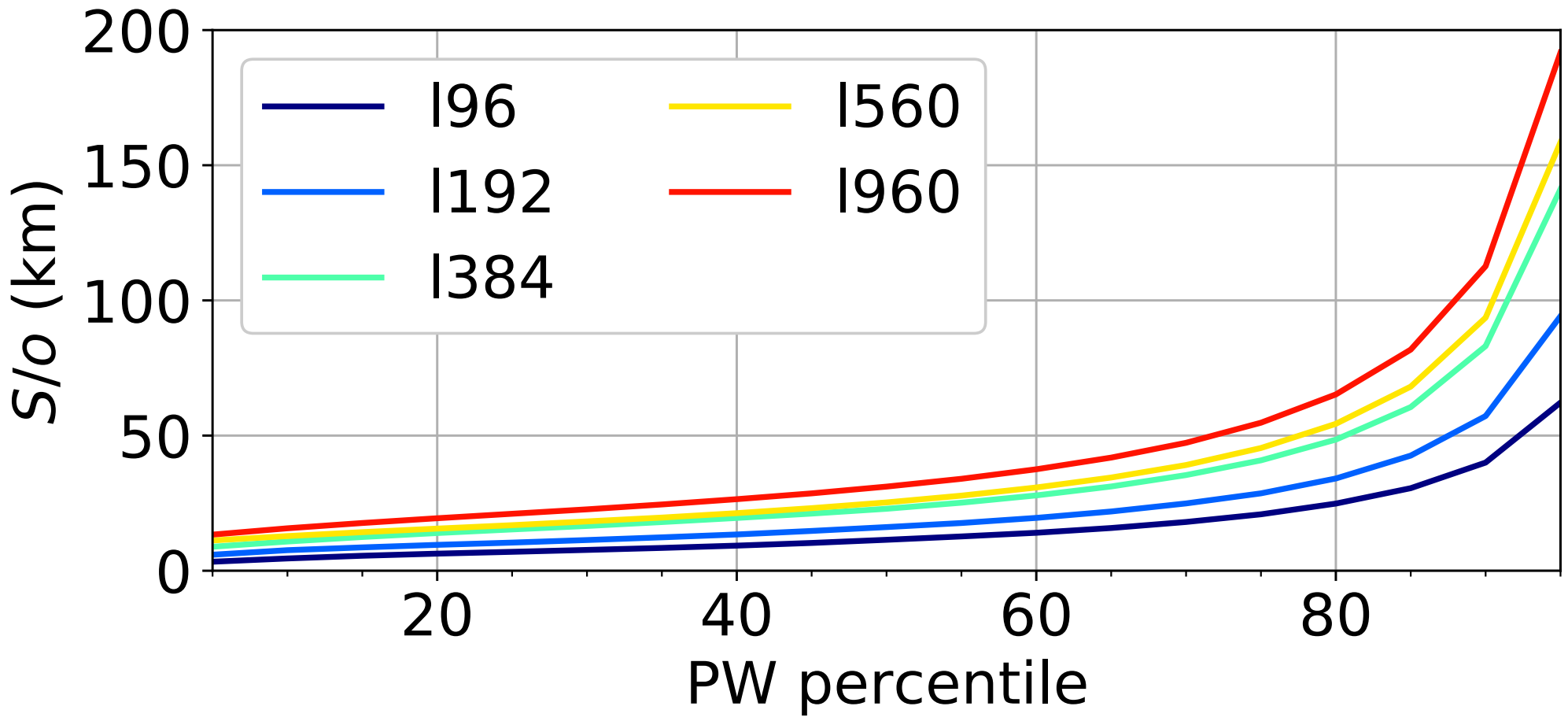

Moisture distance. The ratio of area S to the perimeter o, as a function of PW percentiles (initial 10-day). See Eq. 4.3 in the main text.

図4.14: 周囲長と面積-周囲長比の面積率依存性

- Samples for the horizontal geometries of the boundary between dry and moist regions

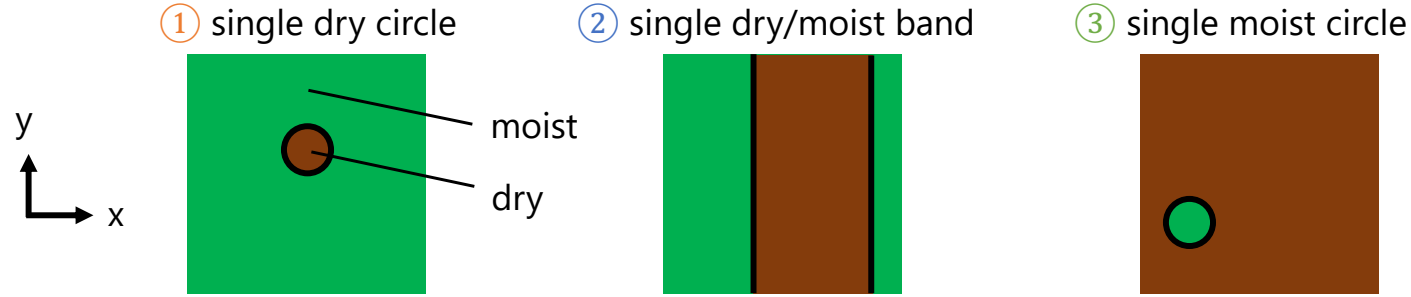

- The perimeter *o* and the area-to-perimeter ratio *S/o* (normalized by domain size *L*) as functions of the area *S*

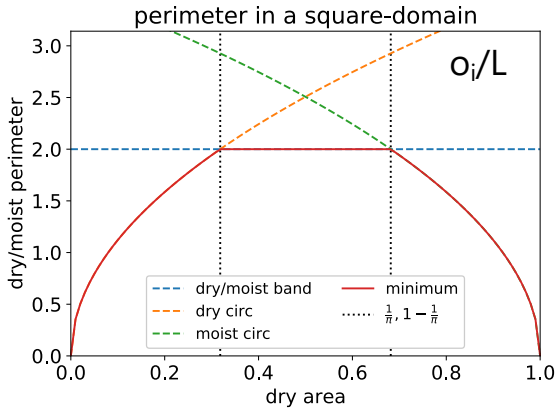

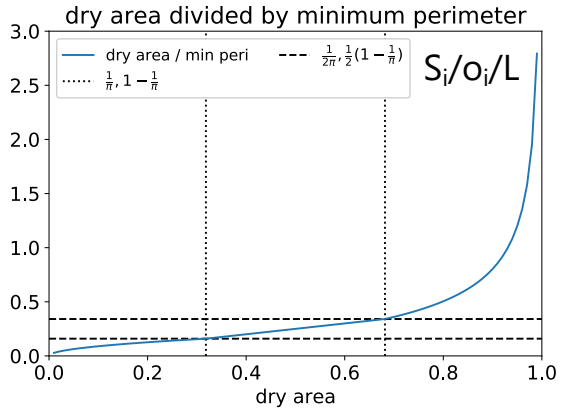

oが最小化される場合のS/o

Schematic of the perimeter and the area-to-perimeter ratio as functions of the area If the dry region has the circular geometry (① single dry circle), S = πr2 and o = 2πr, where S is the area of dry region, r the radius of the dry circle region, and o the length of the boundary of dry and moist region (equivalently the perimeter of dry circle region in this situation). Hence o/L = 2 (πS/L2)^1/2, where L is the domain size. If the dry region has the band geometry (② single dry band), o = 2L. If the moist region has the circular geometry (③single moist circle), o/L = 2 (π(1 − S/L2))^1/2. Assuming that the o is minimized, the dry region has to be circular for S/L2 < 1/π, the dry region has to be band for 1/π < S/L2 < 1 − 1/π, and the moist region has to be circular for 1 − 1/π < S/L2.

図4.15: 面積-周囲長比と面積変化の関係

- **Situation 1**: S_i/o_i scales with the domain size L

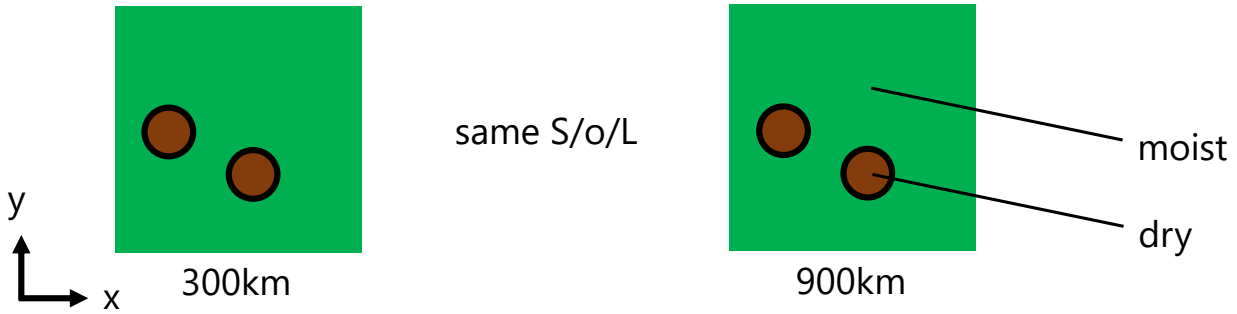

- **Situation 2**: S_i/o_i doesn't scale with the domain size L

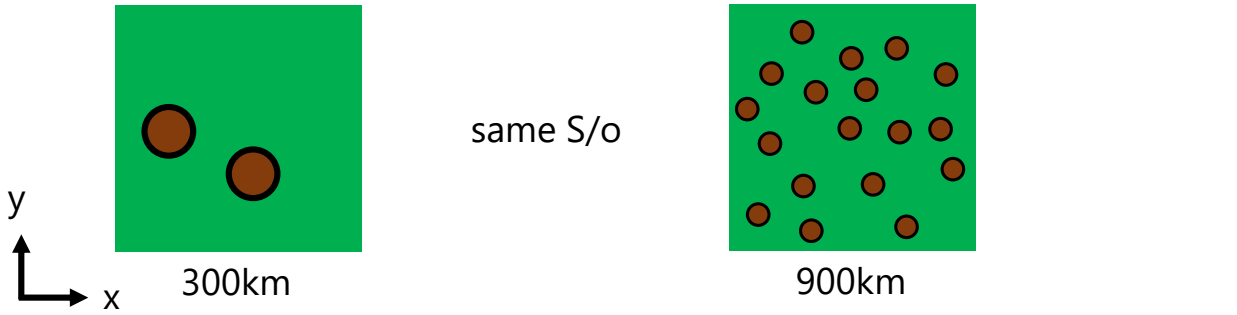

- 実際は, これらの中間で, S/oはLとともに増加する(水蒸気距離の結果を参照).

Schematic of the area-to-perimeter ratio and the change in domain size. The situation 1 indicates the S/o scales with the domain size L, which means the moisture distance proportionally increases with the domain size. On the other hand, the situation 2 indicates the S/o does not scale with the domain size L, which means the moisture distance is invariant.

図4.16: 最近傍対流コア距離

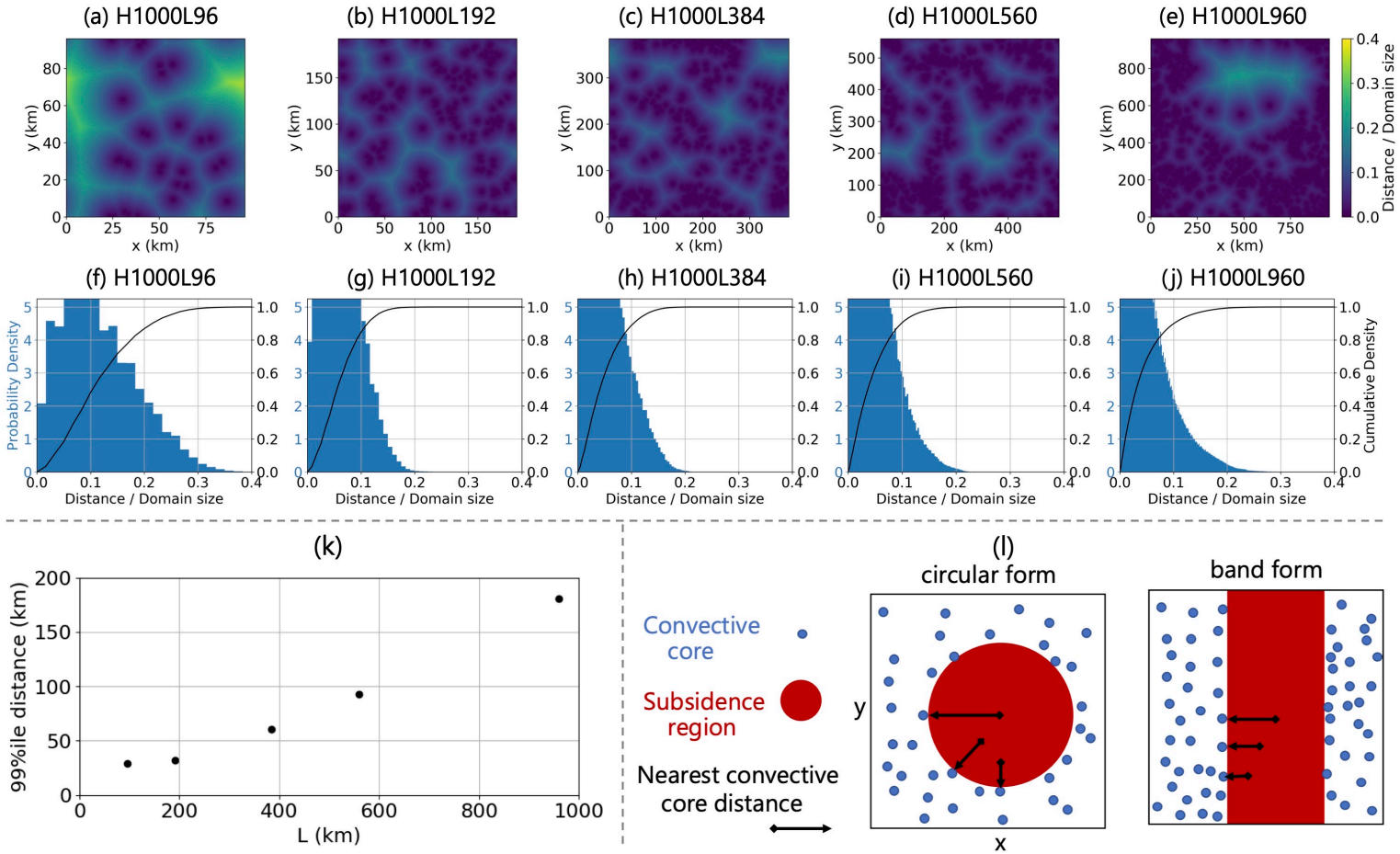

Nearest convective core distance. A convective core is defined as a horizontally connected area where vertical velocity is larger than 1 m s−1 at about 2.5 km height; the position of a convective core refers to its centroid. (a)–(e) Snapshots of the distance divided by the domain size, at an instantaneous time in Day 5. (f)–(j) Histogram of the distance; probability density and cumulative density are shown in blue-left axes and black-right axes, respectively, on Day 5. (k) Largest subsidence area size, defined as the 99th percentile value of nearest convective core distance, based on (f)–(j). (l) Schematic of convective cores distribution, subsidence region, and nearest convective core distances.

図4.17: 風速の水平パワースペクトル

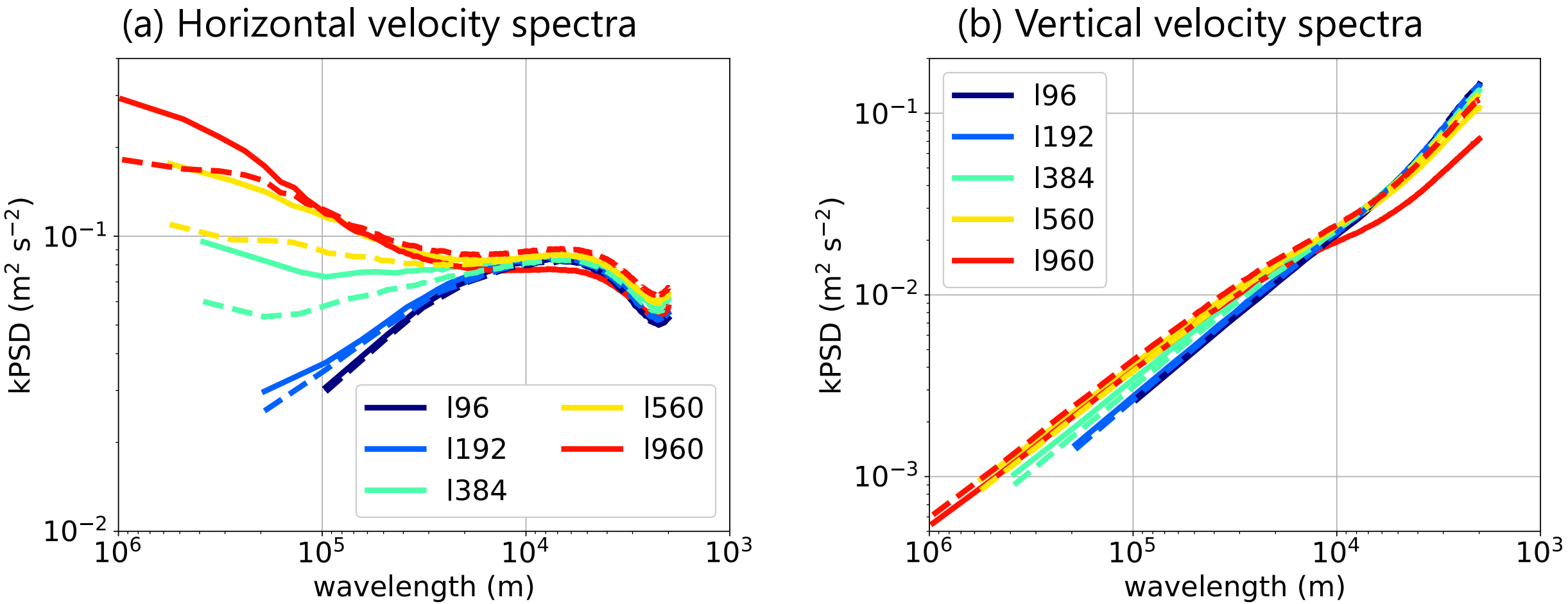

Horizontal power spectral density of wind at 2.5 km height. (a) Horizontal component and (b) vertical component.

図4.18: CSA発生メカニズムの概念図

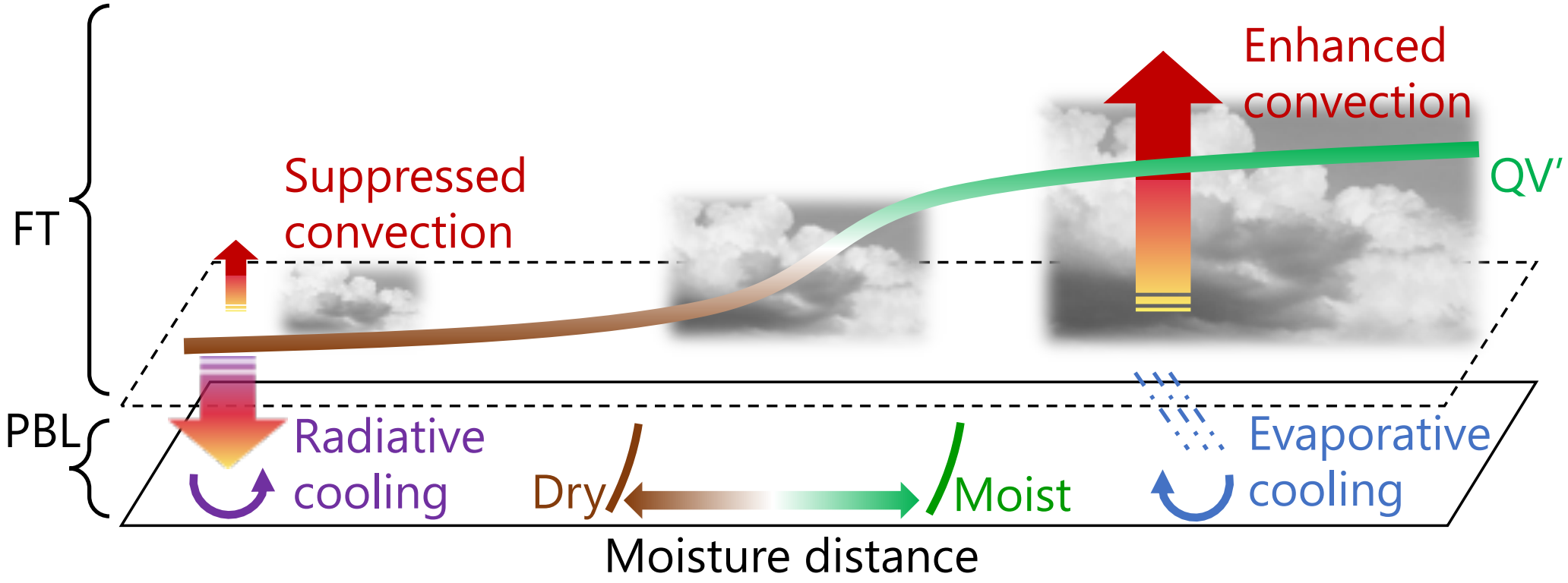

Schematic of the onset mechanism of convective self-aggregation. The development of the anticlockwise circulation near the surface is driven by the buoyancy gradient due to the enhanced radiative cooling in the drier region. The intrusion of the free-tropospheric subsidence into the planetary boundary layer in the dry region precedes the development of the near-surface circulation and happens at the critical domain size where the downward motion in the free-troposphere overwhelms the upward motion in the planetary boundary layer. The strengthening of the free-tropospheric subsidence is due to the weakening of the convective heating, the weakening is due to the dry region getting drier, and the dryness of the dry region is due to the larger scale horizontal variability in the moisture field, which is constrained by the domain size.

最終スライド